Research on the Mechanical Properties of the Sand Cast Magnesium Alloy AZ91

Von der Fakultät für Werkstoffwissenschaft und Werkstofftechnologie
der Technischen Universität Bergakademie Freiberg
genehmigte

DISSERTATION

Zur Erlangung des akademischen Grades

Doktor-Ingenieur

Dr.-Ing.
(Kurzform)

vorgelegt
von Dipl.-Ing. Serguei Erchov
geboren am 10. 09. 1975 in Novorossiysk

Gutachter: Prof. Dr.-Ing. Eigenfeld, Freiberg
Prof. Dr.-Ing. habil. Klimanek, Freiberg
Prof. Dr.-Ing. habil. Riehemann, Clausthal

Tag der Verleihung: 20.12. 2001

Danksagung

Ich möchte mich bei allen bedanken, die mich bei der Anfertigung der Arbeit auf unterschiedliche Art und Weise unterstützt haben.

Herrn Prof. Dr.-Ing. Eigenfeld danke ich für die Bereitstellung des Promotionsthemas, für die gewährte Unterstützung, für Anregungen und Hilfestellungen.

Herrn Prof. Dr.-Ing. habil. Klimanek und Herrn Prof. Dr.-Ing. habil. Riehemann danke ich für die freundliche Übernahme des Korreferates sowie für die sorgfältige Durchsicht und das Korrekturlesen des Manuskriptes.

Besonderer Dank gilt allen Mitarbeitern des Gießerei-Instituts und der Firma ACTech GmbH, die mir bei der Herstellung der Probekörper geholfen haben.

Weiterhin bin ich allen Mitarbeitern des Instituts für Metallkunde und des Instituts für Werkstofftechnik, insbesondere Herrn Prof. Dr.-Ing. Pusch, Herrn Dr.-Ing. Baum, Herrn Dr.-Ing. Klemm, Herrn Dr.-Ing. Trubitz, Frau Dipl.-Ing. Heinzel und Frau Bleiber für ihre Hilfe und die angenehme Zusammenarbeit, zu großem Dank verpflichtet.

Herrn Gabor vom Institut für Werkstofftechnik an der TU Clausthal danke ich für die Übernahme der Spannungsrelaxations- und Dämpfungsmessungen.

Hervorheben möchte ich die hilfreiche Unterstützung von Dr. Lukas und Dipl.-Phys. Neov bei den neutronographischen Texturmessungen am Zentrum für Grundlagen und angewandte Neutronenforschung in Rez, Tschechische Republik.

Contents

1. Introduction
2. Physical Metallurgy of Magnesium Alloys
2. 1. Physical and Chemical Properties of Magnesium
2.2. Magnesium-Aluminium-Zinc Alloys
3. Strengthening Mechanisms of AZ91
3.1. Basic Concepts
3.2. Grain Refinement
3.2.1. Influence of Grain Size on Mechanical Properties
3.2.2. Practical Aspects of Grain Refining in Magnesium Alloys
3.3. Heat Treatment of AZ91
3.3.1. Solid Solution Heat Treatment
3.3.2. Precipitation Heat Treatment
4. Texture Development in Magnesium Alloys
4.1. Definition of Texture
4.2. Orientation Distribution Function
4.3. Measurement of Texture by Means of Neutron Diffraction
5. Stress Relaxation and Damping Capacity of Sand Cast Magnesium Alloy AZ91
5. 1. Introduction to Stress Relaxation and Damping
5. 2. Internal Friction in Magnesium Alloys
5. 2. 1. General Remarks on Internal Friction in Metallic Materials
5. 2. 2. The Concept of Anelastic Relaxation
5. 3. Damping of Mechanical Vibrations
6. Casting of Magnesium Alloys – Practical Aspects
6.1. Reactivity of Magnesium Melts
6.2. Filtration of Magnesium Melts
7. Experimental Procedure
7.1. Casting and Melting Practices
7.2. Studies of Mechanical Properties
7.3. Metallographic Studies
7.4. Neutron Diffraction Tests
7.5. Stress Relaxation and Damping Tests

8. Results and Discussion
8.1. Results of the Filtration Tests
8.2. Results of the Grain Refinement Tests
8.3. Results of the Heat Treatment Tests
8.4. Results of the Instrumented Impact Tests
8.5. Results of the Neutron Diffraction Measurements
8.6. Results of the Stress Relaxation and Damping Tests
9. Conclusions
10. References

1. Introduction

Magnesium alloys are the lightest structural materials being extensively used in automotive and aeronautic applications. The tonnage of magnesium parts used in the automotive industry worldwide increased at an average annual rate of 15% between 1996 and 2000. The increase since 1991 and the projected increase in the use of magnesium die-castings until 2008 (according to International Magnesium Association) is shown in Fig. 1.1. Over 80% of this projected growth is expected in the automotive industry [1].

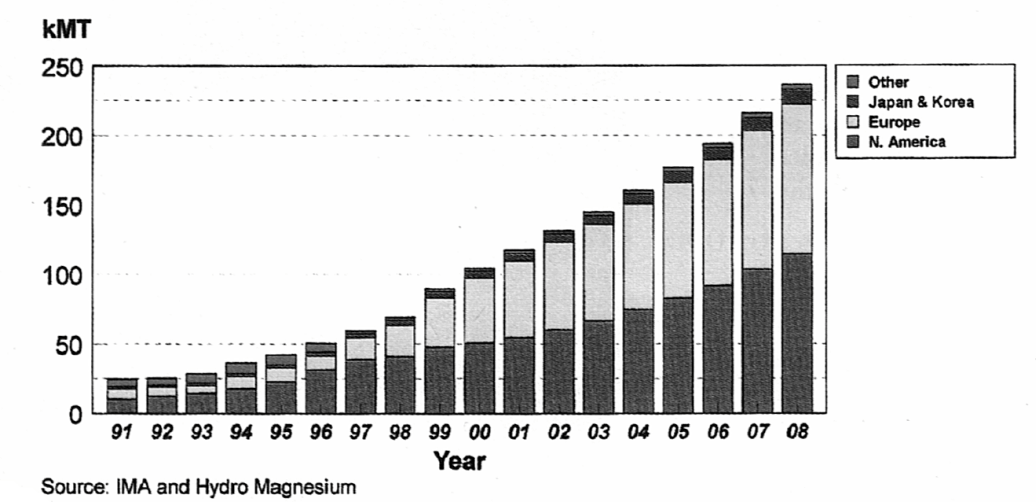

Fig. 1.1. Growth forecast for magnesium die casting in automobiles, in kMT [1].

There are over 60 separate and individual types of components where magnesium alloys are being used or being developed for use in automobiles. The most popular of these components are [1]:

1. Instrument panel substrates
2. Seat frames
3. Steering column components
4. Engine valve covers
5. Transmission housings
6. Intake manifolds

The situation in the aeronautic industry is similar to that in the automotive industry. The size of aircraft, emission regulations and economical considerations in the construction and operation of the aircraft are forcing aircraft designers to manufacture the components in magnesium alloys. Nowadays, magnesium alloys are generally used for aircraft transmission systems and their auxiliary components. In certain cases, large magnesium castings have been used in the cold areas of the engine such as intermediate housing [2].

While automotive castings dominate in terms of the total weight of magnesium consumed, certain non-automotive applications are being made in increasing numbers with considerable added value. These parts are generally very thin walled and relatively small in size, and are most commonly found in laptop computers as well as in hand held devices such as cell phones and various types of cameras. Here, magnesium brings a unique combination of advantages over plastic, namely 100% recyclability, good heat dissipation, electromagnetic and radio frequency shielding and compactness due to the thin walls [3].

The prototyping/testing process is integral to the engineering design process. Since prototypes are fabricated and tested to determine how the part will perform, the process must expose the part to realistic environmental and operating conditions. Prototypes that provide a reliable basis for assessment, i.e., that are close to the final die-casting quality, currently require manufacturing of time-consuming and cost-intensive die casting tools. The gravity sand casting process can solve this problem, as the rapid molding (rapid pattern making) techniques are relatively inexpensive and not very time-consuming. However, while gravity sand cast prototypes exhibit the most important properties of die cast magnesium (including density and modulus of elasticity), others - such as mechanical properties (coarser grain due to lower solidification rate) and porosity - are not as easily duplicated [4-6].

The most widely used magnesium alloy is the aluminium and zinc-containing AZ91 [7] and modern research papers are full of information on the die cast AZ91. However, a thorough literature review has revealed very little data covering the mechanical and certain physical properties of the sand cast AZ91, and these data are also highly controversial. To a certain extent, this is caused by various production methods in

different cast shops, as, for instance, the properties of the parts, manufactured with salt-free melting process may differ from those of the parts, produced with salts. Moreover, if magnesium parts were previously manufactured in green sand molds, today the castings are almost always produced in chemically hardened sand molds.

Nowadays, designers not only need the data on static mechanical properties, but also on the dynamic impact strength, since a large part of magnesium castings are used in structural parts which may underlay crash conditions.

Furthermore, lawmakers require car manufacturers to lower noise pollution caused by cars. Thus, the knowledge on interdependence between manufacturing parameters and damping capacity of the sand cast AZ91 in various conditions may allow a designer to draw conclusions on production methods.

Rapidly growing markets for high-tech and space equipment force manufacturers to find materials with special physical properties, such as high or low stress relaxation. The sand casting method is an ideal manufacturing method for these parts, since it allows economical production of very small series with desirable combination of properties.

Therefore, it is necessary to determine the influence of various manufacturing parameters - filtration, grain refinement, solidification rate (i.e. wall thickness of the part) and heat treatment on mechanical properties, such as strength, elongation, impact strength, damping capacity and stress relaxation.

2. Physical Metallurgy of Magnesium Alloys

2. 1. Physical and Chemical Properties of Magnesium

Magnesium, the lightest structural metal, was discovered in England in 1808 by Sir Humphrey Davy by making an amalgam and distilling off the mercury. The first process for the production of magnesium was developed in 1852 by Robert Bunsen.

Magnesium (at. Nr. 12, at. wt. 24,32) occupies a place in Group II of the Periodic table, and is one of the so-called typical elements. The atom, in its free state, has an ionic core composed of two 1*s* electrons, and two 2*s* and six 2*p* electrons, surrounding the nucleus. The two remaining electrons, in the 3*s* level, are the valency electrons and are easily lost. Magnesium, therefore, is highly reactive [8].

Pure magnesium has a hexagonal lattice structure with lattice ratio *c/a*=1,624. Only the basal plane (0001) is close-packed (Fig. 2.1). At temperatures below 225°C, glide occurs on the basal plane in the most closely packed direction $\langle 11\bar{2}0 \rangle$. In addition to slip, plastic deformation in magnesium occurs by twinning. By twinning, shear forces can produce atomic displacements such that on one side of the plane (the twin boundary), atoms are located in mirror image positions of atoms on the other side. In magnesium, twinning takes place generally on $\{10\bar{1}2\}$ planes (Fig. 2.2). Since there are few operable slip systems in magnesium, twinning is an important mode of deformation in magnesium and its alloys. The amount of bulk plastic deformation from twinning is normally small compared to that resulting from slip. However, the real importance of twinning lies in the accompanying crystallographic reorientations; twinning may place new slip systems in orientations that are favourable relative to the stress axis so that the slip process can now take place. In addition to the twinning on $\{10\bar{1}2\}$ planes, magnesium is observed in rare cases to twin on $\{10\bar{1}1\}$ planes. This effect is relatively unimportant and will not be further considered. At temperatures above 225°C, further glide planes $\{10\bar{1}1\}$ become activated, which result in the markedly increased plasticity, now comparable to those of cubic metals. This effect is caused by the increased thermal movement of atoms in the matrix [8-10].

Grain boundary sliding can also contribute to the plasticity of magnesium during deformation at higher temperatures [11].

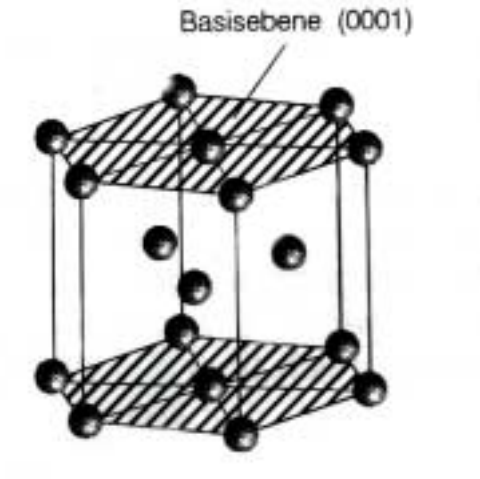

Fig. 2.1. Glide plane (0001) in magnesium lattice (at temperatures below 225°C) [9].

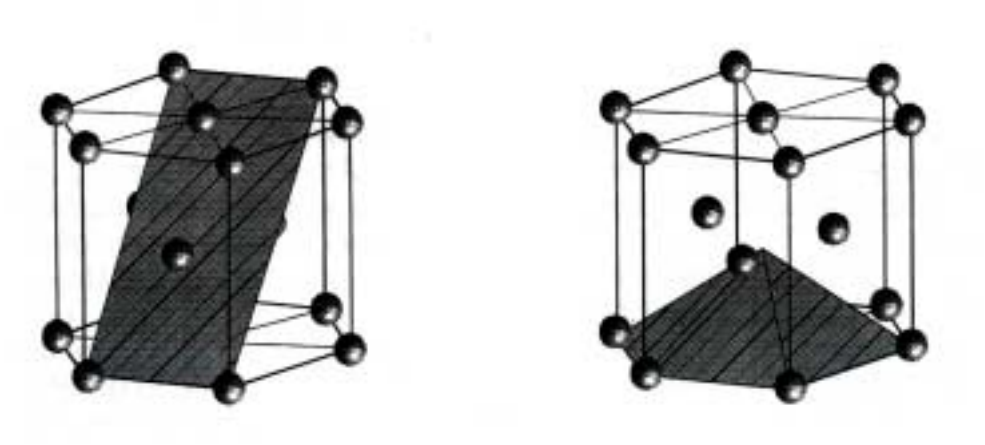

Fig. 2.2. Twinning planes $\{10\,\bar{1}\,2\}$ [9].

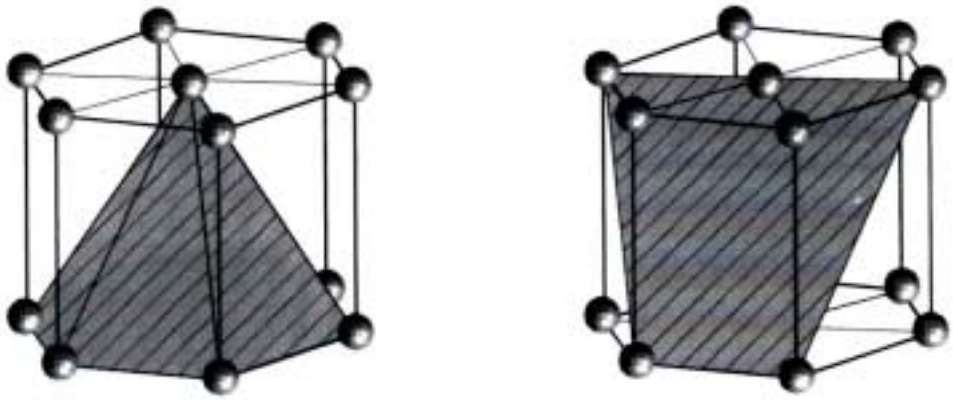

Fig. 2.3. Pyramidal planes $\{10\bar{1}\,1\}$ (temperatures above 225°C) [9].

2.2. Magnesium-Aluminium-Zinc Alloys

The principal concerns in the physical metallurgy of cast magnesium alloys include the effects of chemical composition and heat treatment on mechanical and physical properties. In terms of properties, strength improvement is the major objective in the design of magnesium alloys because magnesium in its pure form is soft, mechanically weak, and hence not generally used for structural applications [12, 13].

The most common alloy systems were developed on the basis of Mg-Al, Mg-Zn, and Mg-Al-Zn systems. Due to the addition of 9wt.-% aluminum and 1wt.-% Zn the best combination of strength and ductility is reached. Al and Zn additions modify not only the mechanical properties but also influence the castability. The effect of Al and Zn on the strength, ductility and susceptibility to hot cracking of binary magnesium alloys is shown in Fig. 2.4. Actual levels of zinc are inversely related to the aluminum contents, and the most widely used magnesium alloy today is AZ91 with a share of ~95% of all commercial magnesium castings. These alloys also contain certain amounts of Mn in order to reduce the corrosion rate [13, 14].

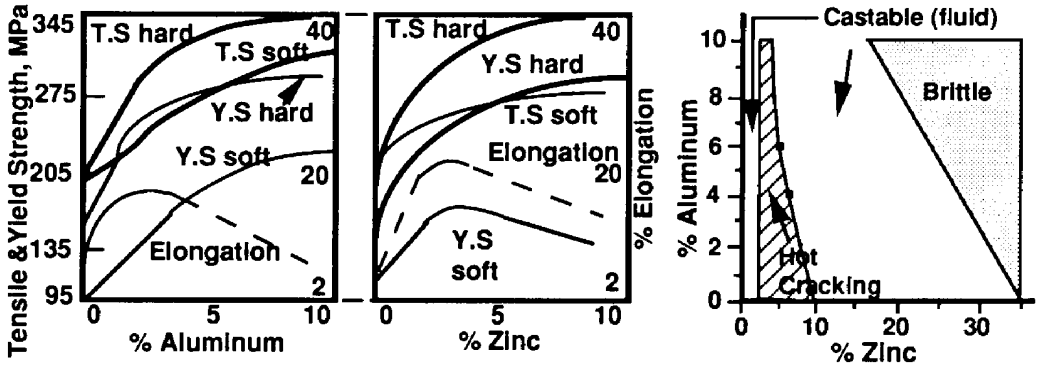

Fig. 2.4. Effects of Al and Zn on the mechanical properties and castability of Mg [13].

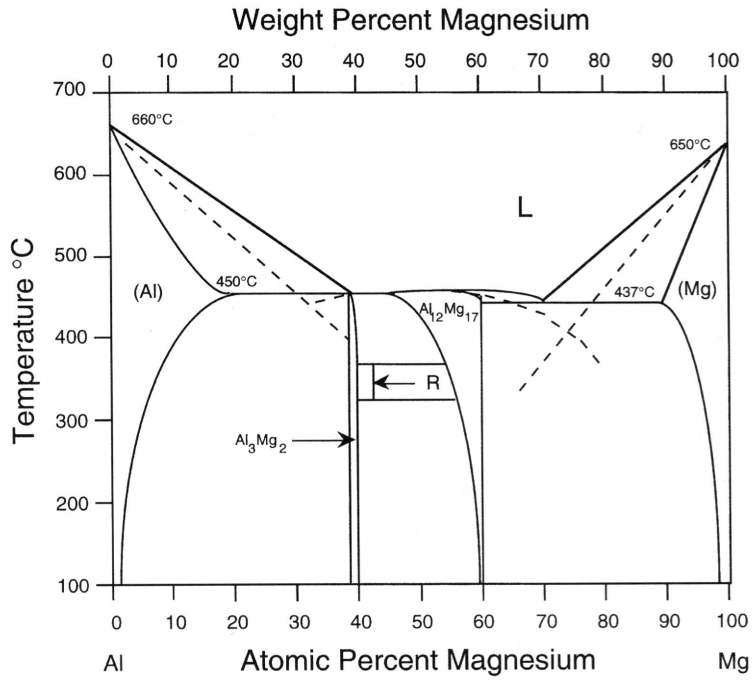

Fig. 2.5. Mg-Al-Phase Diagram [15]

The maximum solid solubility of aluminium in Mg-Al system is 12,7% at the eutectic temperature of 437°C (left side of Al-Mg diagram in Fig. 2.5). The intermetallic contains 32% aluminium, and its composition is $Mg_{17}Al_{12}$. The solid solubility of aluminium in magnesium falls smoothly to a value of 2,1 wt.-% of aluminium at ambient temperature. AZ91 contains 9% aluminium, and, according to the equilibrium diagram, should solidify into a homogeneous matrix of magnesium with aluminium in solid solution [12, 16]. This, however, is not the case. The solidification structure of AZ91 largely depends on the cooling rate. Solidification kinetics of AZ91 was studied by Luo [17]. At the slow cooling rate (0,03-0,4°Cs^{-1}, typical for sand casting) the microstructure consists of a partially divorced eutectic [Mg(α)+$Mg_{17}Al_{12}$(β)] structure plus lamellar $Mg_{17}Al_{12}$(β) precipitates. The formation of the eutectic under non-equilibrium conditions is a secondary process, following primary solidification. And as the amount of the remaining liquid is small, the typical lamellar eutectic structure degenerates [18]. It is believed that the lamellar eutectoid $Mg_{17}Al_{12}$ structure is formed after solidification via discontinuous precipitation from the Mg(α) supersaturated solid solution. Such lamellar precipitates do not appear in specimens with higher solidification rates. At higher solidification rates (gravity die casting and high pressure die casting processes), a divorced eutectic is formed. This is supported by the fact that

the tendency to form divorced eutectic structures is enhanced at higher solidification rates: while the eutectic structure at lower cooling rates assumes a partially divorced morphology, it turns to completely divorced morphology as in the die cast structure, in which Mg(α) grains are surrounded by the $Mg_{17}Al_{12}$(β) phase. The equilibrium liquidus and solidus temperatures, obtained by Luo for sand casting processes are at 600°C and 435°C. These data correspond excellently with our own results [19].

Very interesting results on the microstructure of AZ91 at low solidification rates were published by Aghion [20]. According to the EDX analysis of intermetallics, the chemical stoichiometry of the β-precipitates is not traditional $Mg_{17}Al_{12}$, but $Mg_{17}Al_{11,5}Zn_{0,5}$ due to the significant weight percentage of Zn that is present in the precipitate. A lamellar eutectoid was shown to have a chemical composition of Mg – 85 ± 3%, Al – 13 ± 2%, Zn – 1,3 ± 0,2%. The discontinuous precipitation usually occurs at relatively low temperatures when the total force of transformation is reduced and it is sufficient only for formations of α/β interfaces due to high probability of heterogeneous nucleation as the high boundary-diffusion coefficient provides more effective solute transport via grain boundaries than through the lattice. EDX analysis also indicated that the aluminium content of the Mg-Al- solid solution can vary from 3-4% in bulk to more than 10% in the vicinity of the β-phase.

The microstructure of AZ91 consists not only of Mg (α) and $Mg_{17}Al_{11,5}Zn_{0,5}$ (β) (further for brevity designated as $Mg_{17}Al_{12}$), but also of various iron and manganese containing particles, as shown by Holta and Aghion [21, 22]. Small additions of manganese are given to AZ91 in order to increase corrosion resistance and to bind iron by forming hexagonal $Al_8(Mn, Fe)_5$ particles.

Cast magnesium alloys of the Mg-Al and Mg-Al-Zn systems are suitable for use up to temperatures of 110-120°C. Above these temperatures, the creep rates become unacceptable. It was believed that the poor high temperature behavior originated from the β-Phase. Most researchers agreed with Raynor's statement that the low creep strength of these alloys at temperatures around 150°C was primarily due to the elevated temperature softening of the intergranular β-$Mg_{17}Al_{12}$ phase [8]. However, the elevated

temperature softening of the β-$Mg_{17}Al_{12}$ is highly questionable, since this phase has a very strong covalent bonding and does not soften until 260°C [23, 24].

The most recent studies by Dargush and Dunlop [25, 26] have revealed that the creep mechanism is more complex and that the creep resistance is dominated by the instability of the as-cast microstructure and inhibition of grain boundary sliding when exposed to elevated temperature. Measurements of creep rates and activation energies for creep indicate that the creep strength was linked to discontinuous precipitation of $Mg_{17}Al_{12}$ in highly supersaturated regions of microstructure. Creep studies, comparing the ingot and high-pressure die castings, were conducted by Regev [27]. The results of these tests support Dargush's findings. Sub-micron precipitates of β-$Mg_{17}Al_{12}$ were found near the matrix grain boundaries. As the ingot microstructure is more stable due to a lower solidification rate, ingots show a much lower creep rate than die cast samples. The explanation of creep behavior based on the stability of microstructure is given by Agnew [28]. The volume fraction of β-$Mg_{17}Al_{12}$ grows during the anneal and the primary magnesium phase's lattice constants dilate as aluminium exits the matrix to the new precipitate. First, this results in lattice dilation and will be enhanced under tension due to the positive hydrostatic stress and suppressed under compression. Second, the strain induced by the precipitation reaction is measurable and would increase the creep strain measured in tension and decrease it in compression.

The creep properties are also largely dependent on the quality of casting. The presence of shrinkage and gas porosity dramatically increase the creep rate [28]. The interdependence between the creep rate and different casting techniques was shown by Mordike [30]. As the creep rate inversely depends on the grain size, the highest creep rate was obtained in rapidly solidified alloy samples.

3. Strengthening Mechanisms of AZ91

3.1. Basic Concepts

Plastic deformation in metallic materials is produced by dislocation motion. The theory of dislocations was developed by Polanyi [31], Orowan [32] and Taylor [33] and is excellently presented in [34 - 36]. Because macroscopic plastic deformation corresponds to the motion of a large number of dislocations, the ability of a metal to plastically deform depends on the ability of dislocations to move. Since hardness and strength (both yield and tensile) are related to the ease with which plastic deformation can be made to occur, by reducing the modility of dislocations, the mechanical strength may be enhanced; that is, greater mechanical stresses will be required to initiate plastic deformation. The movement of dislocations is hindered by imperfections in microstructure. Imperfections in microstructure are presented schematically in Fig. 3.1. In contrast, the more unconstrained the dislocation motion, the greater the facility with which a metal may deform, and the softer and weaker it becomes. Virtually all strengthening techniques rely on this principle: restricting or hindering dislocation motion through the introduction of imperfections renders a material harder and stronger [10].

The major hardening mechanisms in metallic materials are [37 - 39]:

- strain or work hardening
- dispersion hardening
- solid-solution strengthening
- grain refinement

As this work investigates magnesium cast alloy, we can mainly influence the mechanical properties through solid solution strengthening, dispersion hardening and grain refinement.

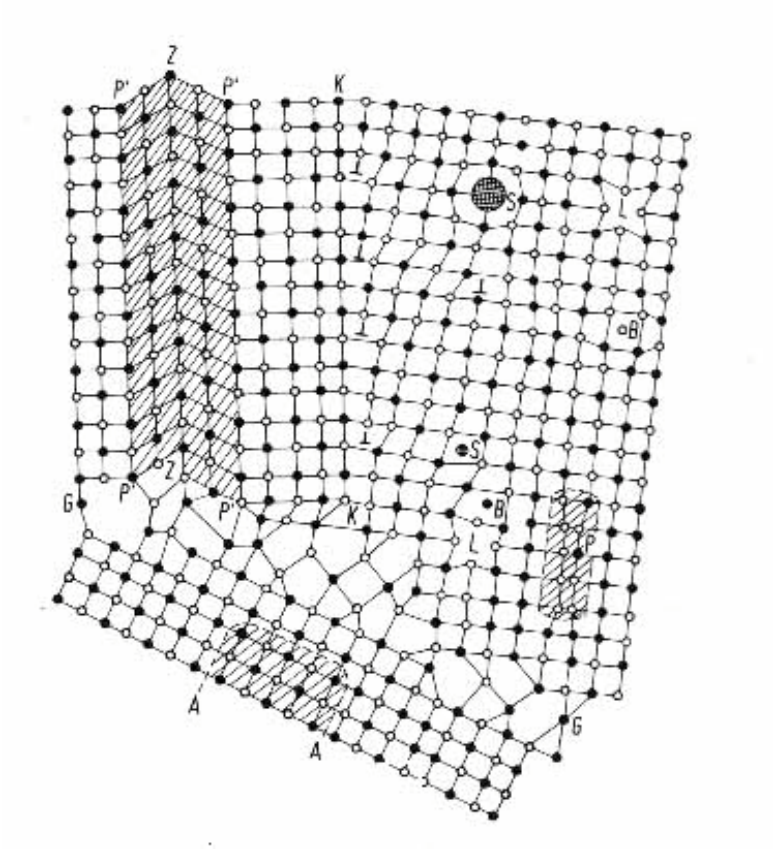

Fig. 3.1. Schematic presentation of a microstructure [40]
L - lattice vacancy, B - interstitial atom, ⊥ - edge dislocation, A-A- Antiphase boundary, Z-Z- twin boundary, K-K-small angle grain boundary, G-G- large angle grain boundary, P- coherent phase boundary, S- solid solute.

3.2. Grain Refinement

3.2.1. Influence of Grain Size on Mechanical Properties

The polycrystal volume is built up of regions displaying an orientation dependent elastic and plastic behavior (the grains) surrounded by two-dimensional crystallographic defects (grain boundaries). The heterogeneity generates an elastoplastic mismatch from the microplastic regime, with its associated pattern of fluctuating internal stresses. The admissible plastic mismatch is resolved by some kind of dislocation accumulation – containing geometrically necessary dislocations – which simultaneously is responsible for the build up of the necessary internal stress state. The presence of those dislocations in the polycrystal grain, in contrast to their absence in a single crystal of similar

orientation submitted to the same plastic strain tensor, implies a true polycrystaline strengthening effect. This effect is grain size dependent, constituting the well-known Hall-Petch relationship [41] (Eq. 3.1):

$$\sigma_c = (\sigma_c)_0 + K_{HP} D^{-1/2} \tag{3.1}$$

where $(\sigma_c)_0$ collects any grain size independent contribution to the flow stress and K_{HP} is an empirical strain dependent factor.

Petch has explained the grain-size dependence as follows: he assumes that all dislocations are pinned and immobile until an applied stress reaches the upper yield point. At the upper yield point plastic deformation commences in a single grain. Yielding takes place in this grain when one dislocation source becomes active and sends out dislocation loops. The dislocation loops move to the grain boundary, where they are stopped. The dislocations which are piled up at the grain boundary produce a stress concentration in the adjacent grains. If the stress concentration is sufficiently large, a source in the neighbouring grain will become activated and throw off dislocation loops. These new loops in turn will produce a stress concentration in another grain and cause the start of plastic deformation in it. Plastic yield thus spreads from one grain to the next and in this manner a Lüders band propagates across the sample [34].

Petch's explanation has, however, a limited applicability, since it is restricted to alloys where dislocations are strongly locked by solutes, or to low stacking-fault energy or long range ordered alloys. This consideration motivated the development of non-pile up theories. Non-pile up theories of Hall-Petch grain boundary strengthening rely on the enhanced dislocation accumulation in the deforming polycrystal relative to the single crystal because of the presence of grain boundaries. The enhancement is attributed to the ability of boundaries for either emission of dislocations (source theory of Li) or trapping of gliding dislocations ("work hardening" theories) [41]

3.2.2. Practical Aspects of Grain Refining in Magnesium Alloys

AZ91 alloy tends to have a large and variable grain size and this effect is important in sand cast part production. Thus, it has been a common practice of grain refining to overheat the melt to a temperature of about 850°C for about 30 min and then to quickly cool the melt down to the cast temperature [42, 14, 43]. This method has the disadvantage of high energy consumption. The strong oxidation of crucible walls should be taken into account, too. There have also been some other grain refining methods in the past, but they were not as wide spread as overheating. The method currently used involves the application of hexachlorethane or other carbon-containing materials to the melt. Grain refinement is attributed to the inoculation of the melt with Al_4C_3 or $AlN{\cdot}Al_4C_3$ [43, 16, 14]. It is, however, difficult to determine how strong the increase in strength is and the data provided are highly controversial [14, 43]. A serious disadvantage of hexachlorethane is the development of deleterious fumes during the melt treatment. Fumes are highly toxic and include chlorine-containing constituents. Other methods of grain refining used in the past included the modification of the magnesium alloy melt with $FeCl_3$-compound [43]. Although the obtained results were considered to be satisfactory, dramatically increased corrosion rate prohibited the application of this method. Extensive research conducted in USSR were concerned with the physical methods of grain refining, such as electromagnetic agitation or ultrasonic refining. The main disadvantage of these methods are the high investment costs necessary for the installation of the grain refining devices [44, 48, 49]. Grain refinement with strontium or titanium carbide is also currently under consideration [46]. However, though grains become finer, no increase in strength was observed.

3.3. Heat Treatment of AZ91

3.3.1. Solid Solution Heat Treatment

Magnesium alloys are usually heat treated either to improve mechanical properties or as a means of conditioning for specific fabrication operations. The type of heat treatment selected depends on alloy composition and on anticipated service conditions. Solution heat treatment improves strength and results in maximum toughness and shock

resistance. Artificial aging (precipitation heat treatment) after solution treatment gives maximim hardness and yield strength, but with some sacrifice to toughness [47].

During the solid solution heat treatment in a range 390-420°C (T4) the as-cast microstructure, consisting of α-Mg, partially divorced eutectic [Mg(α)+$Mg_{17}Al_{12}$(β)] structure plus lamellar $Mg_{17}Al_{12}$(β) precipitates, becomes more homogeneous as the eutectic and lamellar constituents are taken into the solution. After the high-temperature solution treatment, a quench is conducted to maintain the solid solution structure. The strength is increased due to the interaction of dislocations with solute atoms.

Direct interactions between solute atoms and dislocations to be considered as mechanisms of solid solution hardening can be subdivided into two groups [34]:

a) Dislocation locking: Solute atoms collect on dislocations at rest; the solute atoms have time to diffuse to positions of maximum interactions with a dislocation.
b) Dislocation friction: Solute atoms act on moving dislocations; a stationary distribution of solute atoms, assumed to be a statistical distribution on both sides of the glide plane, interacts with a moving dislocation.

In the first case a pronounced yield point should be observed. Slip tends to concentrate by continuing from where it has started. The effect of friction is simply to shift the whole stress-strain curve to higher stresses, although the friction may slowly decrease with increasing strain (if solute clusters are destroyed); a gradual yield point is then observed.

As reported in [14, 51], a solid solution treatment followed by quenching results in a sufficient increase in properties, whereas ductility increases 7 times, tensile strength raises by approximately 60%, but the yield strength decreases slightly.

The effect of various elements (Ba, Be, Bi, Ca, Cu, Ca, Ce, Fe, Li, Mn, P, Pb, Sn, Si, Sr, Ta, Na and Zr) on the solution heat treatment time was studied by Mann [59]. Na and Cu have been shown to significantly decrease the solutioning time.

Solid solution treatment should be conducted under a protective gas atmosphere, otherwise the oxidation of the magnesium surface may lead to fire [57, 51, 52].

Other phenomena which may appear during heat treatment are eutectic or grain boundary melting and grain growth or germination. These phenomena are controlled or eliminated by employing specific heat treatment practices. Eutectic melting is caused by heat treating at too high of a temperature or by heating too quickly to the heat treating temperature. Eutectic melting, in itself, unless unusually severe, does not adversely affect mechanical properties. However, this phenomenon is sometimes accompanied by intergranular oxidation causing voids which lower mechanical properties. The common practice to avoid eutectic melting is to slowly raise the temperature of the casting being heat treated through the lower part of the temperature range to permit diffusion of the low melting point eutectic into the solid solution matrix [53].

Germination is the tendency of aluminium-containing magnesium alloys to develop large grains when held at temperatures at or near the homogenization temperature and has been observed by various workers [14, 54]. This is generally detected on machined surfaces of castings. The enlarged grains usually occur in irregularly shaped areas surrounded by normally fine grained areas.

Germination may occur in sections of casting in which the following conditions exist during the heat treatment:

a) Grain size is fine
b) Internal stresses and stress gradients are present although the magnitude of these stresses appears to be quite small. Chilled areas are particularly prone to germination.
c) Time at solution heat treatment temperature is sufficient to effect complete solution of grain boundary constituent. Germination apparently does not proceed until the grain boundaries are essentially free of interfering material.

One positive method of preventing germination is the interrupted solution heat treatment. The concept of this treatment is that germination cannot proceed without a gradient in energy levels within the casting. The volume change resulting from

alternative solution and precipitatioon relaxes the lattice and eliminates gradients in the stress and energy level. For AZ91, the following solution heat treatment is recommended: 6h at 415°C, cooled to 350°C and held for 2h, reheated to 415°C and held for at least 10 hours. The charge is then regularly quenched.

The temperature and the type of quenchant may seriously change mechanical properties, with a lower quenchant bath temperatures leading to higher tensile and yield strength. However, thermal cracking may be observed in complex parts at very low temperatures of quenchant [59]

Aging of the supersaturated solid solution for a sufficient length of time causes precipitation of the second phase. The basic requirement of a precipitation-hardening alloy system that the solid solubility should decrease with decreasing temperature is filled in the case of AZ91. This precipitation occurs by a nucleation and growth process, fluctuations in solid concentrations providing small clusters of atoms in the lattice which act as nuclei for the precipitates [50].

3.3.2. Precipitation Heat Treatment

Aging of the resulting structure in a range 180-230°C leads to a partial decomposition of the solid solution and to the precipitation of minute $Mg_{17}Al_{12}$ particles. The formation of the precipitates greatly strengthens an alloy. The increase in yield strength depends principally on the strength, structure, spacing, size, shape and distribution of the precipitate particles as well as on the degree of misfit or coherency with the matrix and on their relative orientation. A dislocation moving on its slip plane containing a distribution of precipitate particles may cut through the particles or avoid them by moving out of its slip plane or by bending between the particles, leaving a dislocation ring around each precipitate. For all of these processes, energy must be expended [33].

It is well known that the largest increase in strength can be obtained with coherent precipitates, which may be penetrated by moving dislocations. Incoherent particles are impenetrable for the matrix dislocations, as no common crystal planes are present. Moving dislocations must bend around incoherent particles and bypass them by Orowan

mechanism. Maximum strength may be achieved with coherent precipitates, which have reached critical size [34, 50].

Aging of Mg-9%Al alloy was studied by Clark [55]. It was found out that both discontinuous and continuous precipitatation occurred. The discontinuous precipitation, most pronounced in the early stages of aging, was made up of lamellae of $Mg_{17}Al_{12}$ and an equilibrium composition matrix growing behind the migrating grain boundary. No evidence for the formation of either G.P. zones or a transition lattice of the $Mg_{17}Al_{12}$ precipitate was obtained. The $Mg_{17}Al_{12}$ lamellae were parallel to the basal plane of the matrix. In the solution treated condition, basal slip and $\{10\bar{1}2\}$ - twins were the principal deformation modes. Precipitation induced cross slip on the prism planes and tends to suppress $\{10\bar{1}2\}$ - twin formation. It has been shown that the alloy is hardened by complex dislocations on the prism and basal planes. It was also discovered that the poor aging characteristics of Mg-9%Al alloy are due to the incoherency, large size and large interparticle spacing of the $Mg_{17}Al_{12}$ plates.

Studies of the aging behaviour of AZ91, conducted by Crawley [56] have revealed that the precipitating phase is $Mg_{17}Al_{12}$ and confirmed the orientation relationship of the continuous precipitation, obtained by Clark.

The effect of trace elements on the aging behaviour of AZ91 alloy was studied by Bettles [57]. Ten elements (B, Mo, Ca, Ba, Sr, Pb, Ti, Ag, Si, Li) were added in trace amounts to AZ91 and it has been found out that in most cases, the addition of trace elements has a large effect on the times for the various stages of aging. Similarly, many additions have a marked effect on the rate of development and type of microstructure of the alloys. However, the maximum hardness values were all within 10% of that for AZ91.

Aging of Mg-9Al-Zn alloys was investigated by Lagowski [58] by means of changes in hardness, dimensions and electrical resistivity. Three periods were determined: 1) the incubation period, where some contraction and an increase in electrical resistivity takes place; 2) the main precipitation, where electrical resistance rapidly decreases and dimensions, hardness and tensile properties rapidly increase; 3) the overaging, where

electrical resistivity is levelled off, hardness slightly decreases and expansion reaches a maximum.

Though various research has been done on aluminium-containing magnesium alloys, no clear interdependence between wall thickness of the part, melt treatment and heat treatment was provided. Therefore, in this work, mechanical properties of samples of two different diameters (16 mm and 50 mm) will be investigated. Samples are to be cast with both grain-refined and non-grain-refined melts, and heat treated with various heat treatment methods.

4. Texture Development in Magnesium Alloys

4.1. Definition of Texture

Virtually all magnesium castings are polycrystalline. The properties of magnesium parts largely depend on the properties of single crystals which form the resulting casting. The properties of single crystals may be strongly anisotropic. In order to describe this anisotropy, the knowledge of the orientation of single crystals in the polycrystalline casting is of great importance. Designers and foundrymen usually underestimate the importance of these factors (thorough literature review has revealed that no information on the texture development in magnesium castings is available) and one of the goals of this thesis was to determine the texture development in magnesium parts during solidification and deformation processes.

During the solidification and / or deformation, the constituent grains of the casting may acquire a preferred orientation or texture. The grains approximate, generally with a good deal of scatter, to an ideal orientation. Sometimes several such orientations (texture components) coexist, so that the total scatter is greater. A texture can thus, be described in terms of the ideal orientation or group of ideal orientations to which it approximates [34].

Methods for the description of crystallite orientation and texture are excellently presented in [34, 60]. Crystallite orientation is the orientation of the crystal lattice with respect to external axes of the sample. External axes of the samples are defined by the "sample reference system", $x_1x_2x_3$. A "crystal reference system" $x_1^c x_2^c x_3^c$ is placed on 3 characteristic directions of the crystal lattice that are normal to each other. Using both systems, the crystallite orientation may be described as the orientation of $x_1^c x_2^c x_3^c$ with respect to $x_1x_2x_3$. The description is often done by means of the three Euler angles φ_1, Φ, φ_3. Figure 4.1 illustrates their meaning. The sample system $x_1x_2x_3$ is first rotated by an angle φ_1 around x_3. Let the rotated axes be $x_1'x_2'x_3'$. They are in turn rotated by an angle Φ around x_1'. By now, x_3' has already become x_3^c, around which a third rotation by an angle φ_2 is carried out. So the three successive rotations bring the sample system into

the angular position of the crystal system. Theoretically the range of the Euler angles to be considered is 0 - 360° for φ_1 and φ_2 and 0 - 180° for Φ.

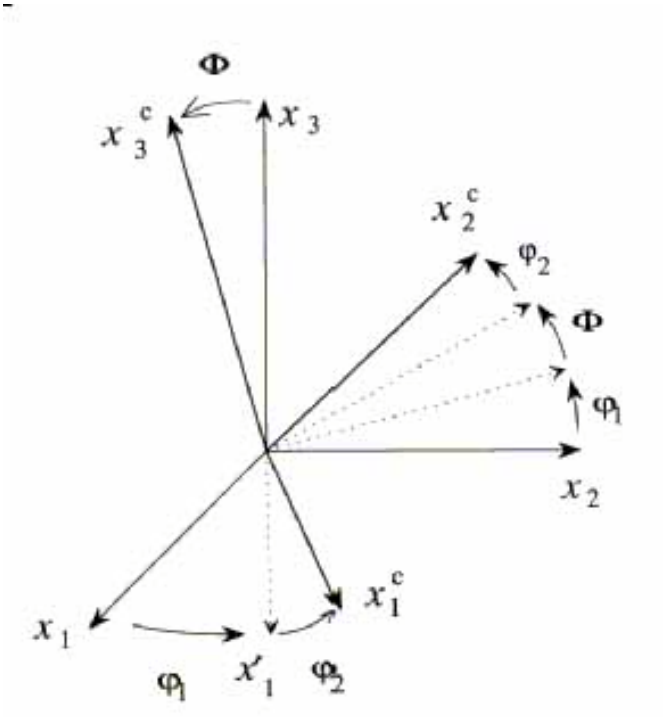

Fig. 4.1. Euler angles that describe the orientation of the crystal system $x_1^c x_2^c x_3^c$ with respect to the sample system $x_1 x_2 x_3$ [34].

4.2. Orientation Distribution Function

The "orientation distribution function" (ODF) describes the crystallographic texture of the specimen. The symbol *g* is often used as a short-hand notation for φ_1, Φ, φ_2. The usual symbol for the ODF is *f(g)*. It is usually assumed that the number of crystallites is infinite, and that *f(g)* is a continuous function. Let *g* be the crystal orientation, and d*g* an infinitesmal range around it. Then *f(g)dg* is by definition the volume fraction of all crystallites for which the crystal orientation is within the range *dg* (Eq. 4.1).

$$\frac{dV}{V} = f(g)dg = f(\varphi_1, \Phi, \varphi_2)\frac{\sin\Phi}{8\pi^2} d\varphi_1 d\Phi d\varphi_2 \qquad (4.1)$$

Where dV is the volume fraction of all crystallites, which orientation in the sample is given by three Euler angles φ_1, Φ and φ_2.

An ideal orientation and statistical spread about it, as well as the relative proportions of several constituent textures are presented in the pole figure, which is plotted from X-ray diffraction or neutron diffraction data obtained from the sample. To produce a pole figure, imagine all grains concentrated at the center of a sphere and then construct normals to all of the lattice planes of a particular family (say {110}) in all grains, so that each forms a spot where it cuts the sphere. If there is a texture, the spot density varies in different parts of the spherical surface, and contours of equal spot density are drawn to define areas of high and low concentration (Fig. 4.2).

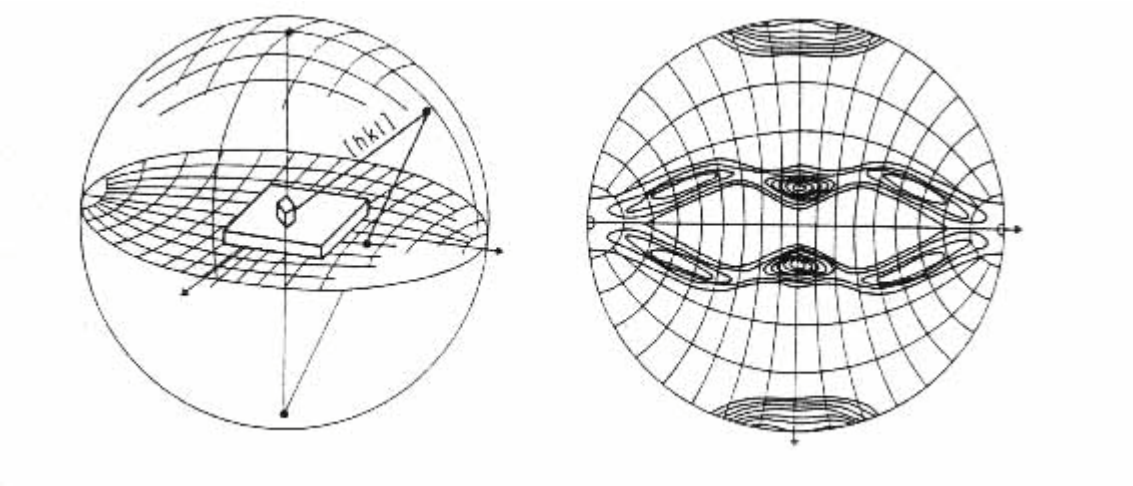

Fig. 4.2. Spherical projection surface and resulting pole figure

4.3. Measurement of Texture by Means of Neutron Diffraction

The basic principles of the X-ray and neutron diffractions are very similar. Figure 4.3 shows a beam of X-rays of wavelength λ, impinging at an angle θ on a set of crystal planes of spacing d. The beam reflected at the angle θ can be real only if the rays from each successive plane reinforce each other. For this to be the case, the extra distance a ray, scattered from each successive plane, has to travel, i.e. the path difference, must be equal to an integral number of wavelengths, $n\,\lambda$. For example, the second ray shown in Fig. 4.3 has to travel further than the first ray by the distance $PO + OQ$. The condition for reflection and reinforcement is then given by Eq. 4.2.

$$n\,\lambda = PO + OQ = 2ON\,\sin\theta = 2d\,\sin\theta \qquad \text{Eq. 4.2}$$

This is the Bragg law and the critical angular values of θ for which the law is satisfied are known as Bragg angles. The directions of the reflected beams are determined

entirely by the geometry of the lattice, which in turn is governed by the orientation and spacing of the crystal planes [50].

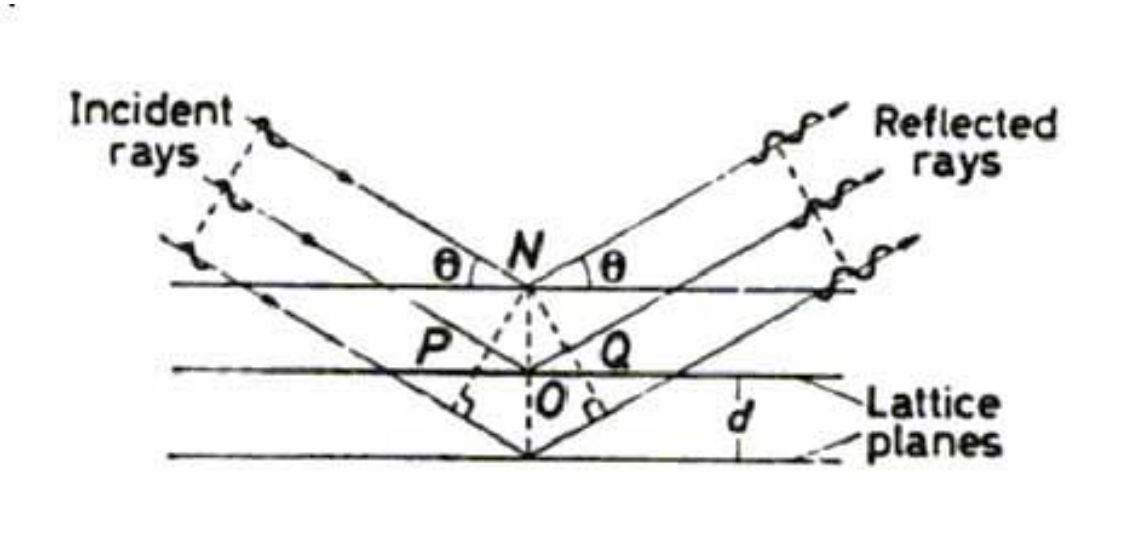

Fig. 4.3. Diffraction from crystal planes [50].

For the investigations of the polycrystalline structures, samples are mounted on the goniometer, which allows for a complete recording of the scatter phenomena [61 - 63].

In this work, neutron diffraction was used to obtain the pole figures. The most important advantage of the neutron diffraction for the purpose of this study is the low impact of grain size on the exactness of measurement (i.e., measurements of samples with relatively large grains 100-200 μm are possible) [62].

The goal of the neutron diffraction investigations conducted in this study was to determine textures and orientation distribution functions in samples of AZ91. The results of these investigations may allow qualitative statements on the factors, which play a major role in mechanical behaviour of variously treated sand cast parts of AZ91.

5. Stress Relaxation and Damping Capacity of Sand Cast Magnesium Alloy AZ91

5. 1. Introduction to Stress Relaxation and Damping of Mechanical Vibrations

The internal friction properties, i.e. reversible stress relaxation and damping of metallic materials are largely neglected by mechanical engineers, as the scale of these effects in most metals is relatively small. It is, however, well known, that pure magnesium has an internal friction similar to or even higher than that of certain polymer materials. Stress relaxation and damping of magnesium alloys may be largely varied due to alloying and heat treatment in order to suit various engineering needs. Thus, the designer can choose between magnesium alloys with high damping capacity (HIDAMETS – **Hi**gh **Da**mping **Met**a**ls**) and alloys with low relaxation (LODAMETS – **Lo**w **Da**mping **Met**a**ls**). Alloys with high damping capacity may effectively suppress mechanic vibrations, noise emissions, equipment malfunctioning, etc. Whereas a careful component design is useful in avoiding resonance effects and concentration of vibration amplitudes, intrinsic material damping properties may contribute considerably to the desired objective with the smaller investment in material. For other applications, magnesium alloys with a low relaxation may be required in order to obtain high dimensional stability in precision mechanical instruments [64 - 66]. Moreover, if magnesium alloy parts are to be joined by means of bolting, low relaxation is desirable. Over the years, progress was achieved in investigations of internal friction in magnesium alloys and composites [66 - 77]. The literature revue has shown, however, that there exist very few data covering the stress relaxation and damping of the sand cast AZ91.

One of the goals of this study was to obtain information on damping capacity and stress relaxation properties of sand cast AZ91 in various conditions. Moreover, it is necessary to obtain data on the interdependence of the structure of AZ91 and its internal friction properties. This knowledge will help designers to select a proper manufacturing process for AZ91 parts, so that an optimal combination of mechanical and acoustical properties can be obtained. Furthermore, if a clear relationship between the microstructure and the internal friction properties is found, this may be used for quality assessment of AZ91 parts.

5. 2. Internal Friction in Magnesium Alloys

5. 2. 1. General Remarks on Internal Friction in Metallic Materials

To begin with, the literature review has revealed that there is no consensus on the definition of the "internal friction". It may be stated, however, that the term "internal friction" denotes the transformation of the mechanical energy into heat in a solid. Internal friction may be caused either by anelastic effects, or by hysteretic effects [64, 65]. Anelastic effects have a marked maximum in frequency response at a certain temperature and are mostly thermally activated. This temperature depends on the activation energy, which, in turn, is caused by the movement of crystal defects, such as interstitials, dislocations, grain boundaries, etc.

Internal friction in metallic materials may be caused not only by elasticity, but also by hysteretic internal friction. Two important features characterize this damping mechanism:

a) The absence of the definite relationship between stress and strain. The stress-strain curve of such materials is not clearly determined and is (also) dependent on the previous way in the stress-strain diagram.
b) The absence of the marked relaxation times or relaxation frequencies. For the anelastic effects, maxima of relaxation times build up at certain frequencies. On the contrary, the hysteretic effects are, to a large extent, time- and frequency independent. In practice, only marked stress dependence of the hysteretic damping is present.

The concept of pure hysteretic internal friction is not applied to magnesium alloys at room temperature, and damping is caused primarily by anelastic effects [78].

5. 2. 2. The Concept of Anelastic Relaxation

The description given below of the concept of stress relaxation is based on [9, 64 - 66]. A time-dependent elastic strain component exists in all metallic materials. For an elastic solid it is generally assumed that stress and strain are directly proportional, but in

practice at least a small part of the elastic strain is usually dependent on time as well as on stress so that the strain lags behind the stress.

The relaxation behaviour may be presented as the time dependence of the modulus of the elasticity (Eq. 5.1):

$$\sigma_r + \Delta\sigma(t) = (E_r + \Delta E(t))(\varepsilon_r + \Delta\varepsilon(t)) \tag{5.1}$$

Where $\Delta E(t=0) = E_u - E_r$

In equation (5.1), $\Delta\sigma(t)$ and $\Delta\varepsilon(t)$ denote correspondingly stress and strain, caused by the time-dependent reaction of material ($\Delta E(t)$) on the change of the load conditions. Index *r* means the relaxed state, and index *u* – the unrelaxed state. Thus, the following equation holds for stress relaxation under constant strain ε_0 (Eq. 5.2):

$$\sigma_r + \Delta\sigma(t) = (E_r + \Delta E(t))\varepsilon_0 \tag{5.2}$$

As Hooke's law is valid for the relaxed and constant values, the modulus defect being the relative change of Young's modulus with time, may be presented as (Eq. 5.3):

$$\frac{\Delta E(t)}{E_r} = \frac{\Delta\sigma(t)}{\sigma_r} = -\frac{\Delta\varepsilon(t)}{\varepsilon_r} \tag{5.3}$$

The stress relaxation phenomenon is schematically shown in Fig. 5.1a and 5.1b. In Fig. 5.1a, a plot of load versus time is presented, in which the strain ε_1 and, correspondingly, ε_2 are applied and stay constant for the half-period duration T/2. This time T/2 should be long enough to allow for nearly complete stress relaxation to minimize interaction with preceding strain periods. In this quasistatic relaxation test the repeating changes in strain do not influence the stress behaviour. At the end of the half-period time the strain is immediately changed (A → B, C → D), which causes the

proportional change in stress. The proportionality factor in this test is the unrelaxed modulus of elasticity.

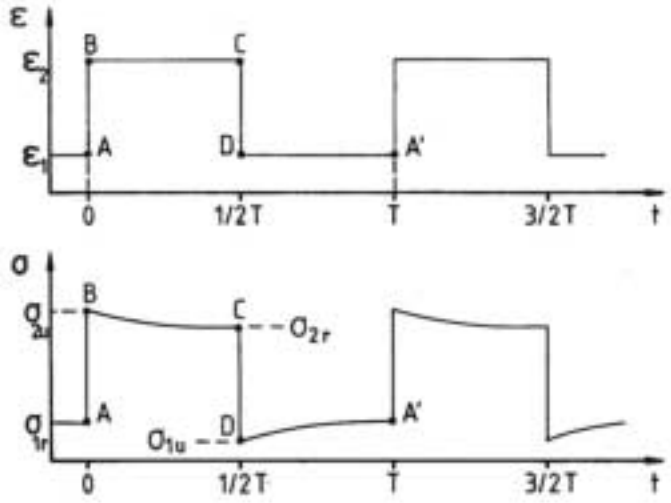

Fig 5.1a. Load versus time [65].

During the following time period of the constant strain (T/2), the stress decreases (B → C) or increases (D → A′) until it reaches its equilibrium (σ_{1r} or, correspondingly, σ_{2r}), which is defined by the relaxation modulus.

The relaxed modulus is the ratio of the relaxed stress to the constant strain change (Eq. 5.4):

$$E_r = \frac{\sigma_{2r} - \sigma_{1r}}{\varepsilon_2 - \varepsilon_1} = \frac{\sigma_r}{\varepsilon_0} \tag{5.4}$$

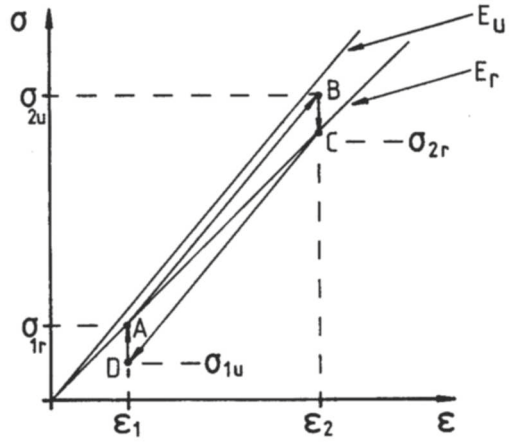

Fig. 5.1b. Hysteretic loop in stress-strain diagram [65].

The resulting hysteretic loop in the stress-strain diagram surrounds the dissipated mechanical energy density (ΔW), which is usually transformed into heat (Eq. 5.5).

$$\Delta W = \oint \sigma d\varepsilon \tag{5.5}$$

The density of the elastic energy, accumulated in the body, is (Eq. 5.6),

$$W = \int_{\varepsilon_1}^{\varepsilon_2} \sigma_r d\varepsilon \tag{5.6}$$

It follows from the figures 5.1a, 5.1b and equations 5.4, 5.5, and 5.6 (Eq. 5.7):

$$\frac{\Delta W}{W_r} = \frac{2\Delta\sigma}{\sigma_r} = -\frac{2\Delta\varepsilon}{\varepsilon_r} \quad \text{with} \quad \Delta\varepsilon = \varepsilon_r - \varepsilon_u ;$$

$$\Delta\sigma = \sigma_r - \sigma_u \quad \text{and} \quad \Delta W = W_r - W_u \tag{5.7}$$

Equation (5.7) is generally valid when the relaxed state is compared to the unrelaxed state. For time-dependent values, equation (5.7) is not valid. However, from equations (5.7) and (5.3) equation (5.8) may be derived:

$$\frac{\Delta W}{W_r} = \frac{2\Delta E}{E_r} = 2\Delta \qquad \text{with } \Delta E = E_u - E_r \tag{5.8}$$

The value Δ is known as the relaxation strength and is time-independent if the body has enough time to completely relax. In practice, neither the start value, nor the final value of the relaxation can be measured. Therefore, Δ is time dependent, and is also called relaxation strength. The value of Δ is dependent on the start and on the end time of measurement. Therefore, in order to obtain comparable results, equal time interval should be chosen.

Equation (5.3) may be rewritten in the following form (Eq. 5.9) and the relaxation function *f(t)* may thus be derived:

$$\frac{\Delta E(t)}{E_r} = \Delta \cdot f(t) \tag{5.9}$$

In this equation, Δ is the relaxation strength, and *f(t)*- the time component of the anelastic relaxation. According to the equation (5.1), $f(0) = 1$ and $f(t) = 0$ for $t \rightarrow \infty$, and *f(t)* permanently decreases with the increase of *t*.

In materials under cyclic loading, the anelastic effects lead to a phase difference (Φ) between stress and strain as well as to a resonance peak which depends on the exciting frequency. Both the phase difference and the half-width of the resonance peak (Q^{-1}) may be used as the measure of internal friction. Perhaps the most common use is the logarithmic decrement δ (Eq. 5.10), the natural logarithm of successive amplitudes of vibrations. In a forced vibration experiment near a resonance frequency, the factor Q^{-1} is often used (Eq. 5.11).

$$\sigma = \ln \frac{A_n}{A_{n+1}} \tag{5.10}$$

Where A_n, A_{n+1} are successive amplitudes of vibration.

$$Q^{-1} = \frac{\omega_2 - \omega_1}{\omega_0} \tag{5.11}$$

Where ω_1 and ω_2 are the frequencies on the two sides of the resonant frequency ω_0 at which the amplitude of oscillation is $1/\sqrt{2}$ of the resonant amplitude. The specific damping capacity may also be used (Eq. 5.12), where ΔW is the energy density dissipated per cycle of vibration energy density W, i.e. the area contained in the stress-strain loop.

$$Q^{-1} = \frac{1}{2\pi}\frac{\Delta W}{W} \tag{5.12}$$

It may be shown from equations 5.10-5.12 that for small damping, equation 5.13 holds:

$$\pi \cdot \tan\Phi = \pi Q^{-1} = \delta \tag{5.13}$$

5.3. Dislocation Damping

In metallic materials, all known defects of crystal structure such as solute atoms, dislocations, grain-, phase- and twin boundaries can yield a contribution to internal friction effects.

It was shown by K. Sugitomo [78] that the damping effects in magnesium alloys are caused by the reversible or irreversible movement of dislocations. The theory of Granato and Lücke, which is based on the vibrating string model for the dislocations, provides an explanation for this phenomenon [79]. The dislocation motion is restricted by two types of pinning points. As shown in Fig. 5.2a the dislocation is assumed to remain solidly anchored at the strong pinning points, A and B. The distance between the strong pinners determines the maximum loop length $\overline{AB}$. When a small oscillating stress is applied, the dislocations bow out between the weak pinners, leading to amplitude independent, frequency dependent damping effects. If the force of the dislocation segments on the weak pinners becomes larger than the binding force of the weak pinners, the dislocation will break out from all of the weak pinning points contained within $\overline{AB}$. This breakaway results in the dramatic increase in dislocation damping. It is, however, assumed, that the network pinning at pinners A and B is strong

enough that no breakaway of network length occurs. When the stress decreases, the dislocation becomes repinned again and on the reversal of the stress, the same sequence will occur and as a result the stress-strain relation will exhibit a hysteretic loop, independent on the frequency of the applied stress. Taking into account the mean distance between weak pinners, l, and that between strong pinners, L, Granato and Lücke revealed that the amplitude-dependent dislocation damping can be written as (Eq. 5.14):

$$Q^{-1} = \frac{C_1}{\varepsilon}\exp\left(-\frac{C_2}{\varepsilon}\right) \tag{5.14}$$

Where

$C_1 = \frac{\Lambda L^3 F_b}{6\pi b l^2 E_u}$ and $C_2 = \frac{F_b}{blE_u}$, Λ being the dislocation density, L and l the average dislocation loop lengths, F_b - the binding force between the dislocation segments and weak pinners, b the magnitude of the Burgers vector, E_u the unrelaxed modulus and ε the strain amplitude.

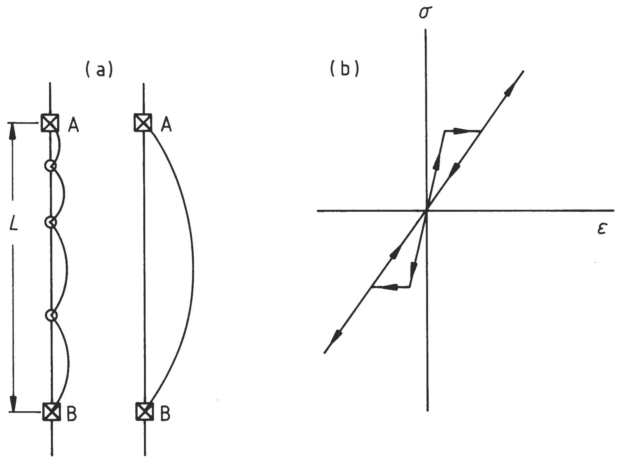

Fig. 5.2(a). Dislocation break-away model according to Granato and Lücke with strong ⊠ and weak ○ pinning points. (b) Schematic stress-strain hysteretic loop for dislocation break away [64].

The Granato-Lücke model is based on the isothermal approach and therefore, disregards any thermal contribution to unpinning and neglects any effects of stress-assisted thermally activated redistribution of weak pinners.

6. Casting of Magnesium Alloys – Practical Aspects

6.1. Reactivity of Magnesium Melts

Molten magnesium alloys are prone to ignition when oxygen is readily available. The reason for this is the high affinity to oxygen and high vapour pressure of magnesium alloys. Magnesium reacts with oxygen according to the following equation:

$$Mg+½\ O_2 = MgO + 145{,}8\ cal/mol \qquad (6.1)$$

MgO film is a very stable compound with a melting temperature of 2825°C. However, this film is porous and cannot prevent the contact of magnesium with oxygen. The high vapour pressure puts high demands on the quality of the protective film. If the magnesium part is heated up to more than 450°C, the MgO-film loses its protective ability and at 623°C the magnesium ignites. Magnesium vapour easily penetrates the oxide film and forms a white MgO fume above the melt. Since this reaction is strongly exothermic, local over-heating of the melt takes place and results in accelerated oxidation and formation of oxide „blooms“ spreading out on the melt surface. In order to avoid ignition, protective gases should be applied [14, 81, 82].

Gas protection of the molten metal surface is currently used by most casters. The application of salt mixtures as a protective means is expensive and decreases the corrosion resistance of magnesium parts. CO_2, Ar, He, SO_2 and SF_6 or their mixtures are in current use as protective gases today. The application of BF_3 as the protective gas is also possible. SO_2 is toxic and if in contact with humidity, it will enhance the corrosion of the steel equipment. Deposits and reaction products may form, which, under unfavourable conditions, may lead to metal eruption from the furnace. The advantage of SO_2 is that this gas is relatively inexpensive and does not have the same environmental impact as SF_6. A film formed with SF_6 is very dense and the evaporation of Mg is almost avoided. The protective effect of SF_6 is superior compared to those of SO_2. The greatest disadvantage of SF_6 is that this gas has been identified as a greenhouse gas by the UN’s Intergovernmental Panel on Climate Change (IPCC). The Global Warming Potential for SF_6 in a 100 years time horizon is currently calculated to be 23,900 relative to CO_2, meaning that 1 kg of SF_6 in the atmosphere gives

approximately the same contribution to the greenhouse effect as 24 tons of CO_2 [82, 83].

Magnesium alloy melts attack most refractory materials, with exception to magnesium oxide, aluminum oxide, graphite and dolomite. Especially violent reactions occur with heavy metal oxides, for example scaling, and with silicon containing materials, such as quartz, silica, waterglas. Consequently, magnesium is molten only in crucibles made of steel. If an ordinary graphite crucible is used, magnesium attacks the clay bonding material. As a refractory material on the inner side of the furnace, shamotte stone should be used, which reacts with magnesium only briefly and not violently [85, 86].

A very important aspect of magnesium sand casting is the reactivity between magnesium alloys melts and the mold material, which leads to various casting defects if no special means is applied to eliminate this effect. Basic chemical reactions occurring when casting magnesium in sand molds may be summarised as follows [87]:

$Mg + H_2O = MgO + H_2 + 77500$ cal (green sand mixtures); (6.1)

$2\ Mg + O_2 = 2\ MgO + 146000$ cal; (6.2)

$2\ Mg + SiO_2 = 2\ MgO + Si$; (6.3)

$4\ Mg + SiO_2 = 2\ MgO + Mg_2Si$; (6.4)

$3\ Mg + N_2 = Mg_3N_2 + 116000$ cal. (6.5)

Inhibitors, such as sulphur, boric acid, potassium tetrafluoborate (KBF_4), ammonium fluosilicate are mixed with the sand to prevent these reactions. In the presence of boric acid, diethylene glycol acts as an inhibitor, although its primary purposes are to keep the sand from drying out and to reduce the amount of water added to the sand [85, 87]. In the Soviet Union, additions to the green-sand mixtures composed of urea ($CO(NH_2)_2$), aluminum sulphate ($Al_2(SO_4)_3$), and boric acid were standard practice [14].

6.2. Filtration of Magnesium Melts

Chemical reactions of molten magnesium melts with oxygen or nitrogen in the air and with mold refractories cause the entrapment of non-metallic inclusions into the casting. The non-metallic inclusions are known to not only deteriorate mechanical properties,

but also to decrease corrosion resistance. The most important inclusions in magnesium are [14, 90, 91]:

- oxides, appearing as lumps, films and apparently loosely connected agglomerates or clusters,
- intermetallic particles,
- chlorides,
- sand grains.

Inclusions may be subdivided into two categories:

- The so-called “primary oxides” which come into the casting from the crucible. These primary oxides have a largest negative effect on the mechanical properties and may be relatively easy detected in the casting by means of X-ray tests.
- The so-called “secondary oxides” are formed during the pouring of the mold. Low viscosity of magnesium melts together with strong affinity to oxygen further aggravates the problem.

The primary oxides may be removed from the melt by various methods, such as fluxing, inert gar sparging, application of an alternating magnetic field or ultrasound and filtration [14, 92 - 96]. Formation of secondary oxides may be avoided through the special gating system design, through the positioning of filters into the gating system and through the scavenging of the mold with inert gases [14, 43, 97].

Extensive studies on gating and feeding techniques for magnesium alloys were conducted by Spitaler [88, 89], Honsel [43] and other researchers [14, 96]. Because molten magnesium alloys oxidize readily, the method of mold filling is more critical than for some other metals. The larger the surface of the melt stream and the higher the fall height, the stronger the oxidation. Turbulence of the metal flow results in the formation of oxide skins and films (dross), which are folded into the flowing metal and appear in the casting as inclusions or surface pitting. To prevent dross from being carried into the casting cavity, proper gating techniques must be used. This problem may be approached in either of two ways: (a) by completely suppressing gating turbulence and thereby preventing dross formation; or (b) by tolerating a certain amount

of turbulence in the early parts of the gating system, accepting the formation of some dross, but separating such dross from the metal stream before it enters into casting. It is rarely possible to prevent dross formation completely; therefore provisions are usually made for the separation of dross from the metal stream before it enters the casting.

Filtration of magnesium melts may be an effective means in improving the mechanical properties of magnesium parts. Currently, steel wool filters are in common use. However, ceramic foam filters could be an interesting alternative to steel wool [95 - 97].

Ceramic foam filters were introduced to filter molten aluminum in the 70`s. Ceramic foam technology expanded rapidly and became the preferred method to filter not only aluminum melts, but also iron melts. The high efficiency of ceramic foam filters is caused by the complex structure of interconnected pores. During the flow through the ceramic foam structure, melt frequently changes its direction, and thus, even tiny particles with sizes much smaller than the filter pore size become captured.

The general theory of filtration is presented in [98, 99]. Basically, the filter works as a porous screen, removing and retaining particles too large to pass through the openings of the filter, but allowing the carrier fluid to pass. Particles are retained in the filter medium by numerous mechanisms. The most important are direct interception, inertial impaction and diffusion.

Direct interception occurs when a particle collides with the filter medium. Inertial impaction occurs if a particle fails to negotiate the tortuous path within the filter, collides with and adheres to a filter material. Diffusion is only of interest for the filtration of aerosols and will not be discussed here.

The simplest type of mechanical filter provides only surface retention and works largely by direct interception. Particles larger than the pore size of the filter are stopped at the upstream surface of the filter; their size prevents them from entering and/or passing through the pores or openings.

The other basic type of mechanical filter employs a medium with a significant thickness, providing “depth filtration”. The mechanism of filtering becomes more

complex. The path through the filter is much longer and random, providing greater possibility for both direct interception and inertial impaction.

The overall performance of a depth-type filter can be better than that given by its purely mechanical action or direct interception. The inertia of particles impining directly on the filter medium may generate absorptive forces, and Brownian movement effects may be present with fine particles, again developing absorptive retention.

Therefore, we may conclude that the ceramic foam filters represent a special type of the depth-type filter.

The efficiency of the ceramic foam filter is affected by the following factors [100]:

- Amount of superheat
- Filter preheat temperature
- Filter pore size
- Molten metal/filter heat transfer coefficient
- Latent heat of solidification
- Contact wetting angle
- Metal density
- Metal velocity.

Literature review has revealed that no data are available on how the application of various filter types and gating systems improves the mechanical properties of AZ91. Therefore, different filters were studied. But the primary target of the filter efficiency tests was to obtain reliable data on the mechanical properties of the sand cast AZ91 if the influence of the impurities was largely excluded.

7. Experimental Procedure

7.1. Casting and Melting Practices

Chemical composition of the AZ91HP alloy, delivered by Norsk Hydro, was determined by the spark diffractometry in the experimental foundry of the Technical University of Freiberg and is presented in Table 7.1.

Table 7.1. Chemical composition of the AZ91 alloy used in the present investigation (in weight percents).

Al	Zn	Mn	Zr	Cu	Si	Fe	Ni	Ca	Sn	Be	Pb	Mg
9,51	0,901	0,224	0,001	0,0174	0,0547	0,0135	0,0017	0,0036	0,005	0,0003	0,0089	Bal.

In the present study, the furan/acid nobake system was taken for the production of molds. Silica sand (SiO_2) was used as a refractory material. The resin binder used was of Bakelite 9915GN01 type, manufactured by Bakelite AG, and the catalyst used was of GS-2 type, produced by Ashland-Südchemie-Kernfest GmbH, all of Germany. This system is known for its satisfactory reactivity with all types of acid catalysts, excellent erosion resistance, good hot strength and satisfactory shakeout properties. In order to avoid reactions between the mold and the magnesium melt, the mold surface was sprayed with the alcohol-based Molco 41A coating, manufactured by Foseco GmbH, Germany.

The melting procedure was conducted in a crucible made of a plain low-carbon steel (20kg capacity). As a protective gas, Argon (99,99%) was used. A thermocouple was inserted into the plain steel tube and introduced into the crucible. The pouring temperature was 750°C in all cases.

The grain refiner used in this study was manufactured by Schäfer Chemie und Umwelt GmbH, Germany and has the trademark MAXOFLUSS – MG T 431 GR (principal constituent C_2Cl_6). TiC and activated carbon additions were also investigated. The measured amount of grain refining agent was introduced into the crucible at 750°C. Killing time was 10 minutes in all cases. This relatively short killing time was chosen

because of the small volume of the crucible. If necessary, the melt was then brought up to the pouring temperature of 750°C.

7.2. Studies of Mechanical Properties

Two types of casting were used for manufacturing the tensile tests samples. The first casting is presented in Fig. 7.1. This is the casting according to the German aeronautic standard. The bar's diameter is 16 mm. It may be noticed that a gating system is designed to avoid the entrapment of impurities into the bars and to smooth the melt's flow. The riser's height is 400 mm. The feeders have a diameter of 50 mm and allow for the proper feeding of the bars. The second casting has basically the same design, but the gating system is modified to allow for the installation of filters (Fig. 7.2). The 50 mm diameter samples were machined from the feeder bars of this casting. However, in order to guarantee directed solidification, chillers were installed at the bottom of the feeder bars, and large feeders were put on the top of the feeder bars. For the purposes of comparison, gravity die cast bars (20 mm diameter) were also manufactured. The design of the die cast tools allowed for a good feeding of the samples. The temperature of the die prior to pouring was held at 300°C.

Three types of filters were investigated. These filters are presented in Fig. 7.3. The first type was the Foseco ceramic foam filter with a thickness of 20 mm and pore sizes of 10, 20 and 30 ppi (pores per square inch). In Fig. 7.3. these are filters 1, 2 and 3. The second type was a Schäfer ceramic foam filter with a thickness of 14 mm and pore sizes of 10 and 20 ppi (filters 4 and 5) The third type was a typical steel wool filter, manufactured by Britnit Ltd, UK (filter 6).

Samples for the impact tests were machined from the Y-shaped castings with a thickness of 20mm and 40mm. Filters were inserted into the gating system to avoid turbulences and the entrapment of oxides. Y-shaped castings were chosen because they allow for a good feeding of the samples and thus, reduce the negative influence of porosity on the impact properties.

Fig. 7.1. Casting according to the German aeronautic standard (Later on - Casting 1)

Fig. 7.2. Modified German aeronautic standard casting (Later on - Casting 2)

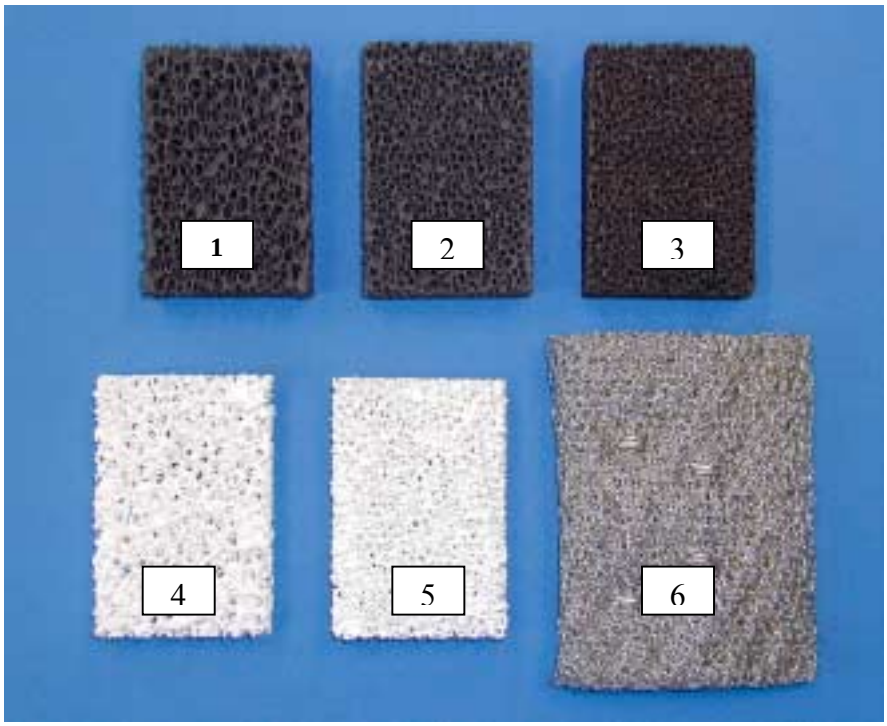

Fig. 7.3. Filters used in this study

The solid solution heat treatment (T4) was conducted in a protective argon atmosphere at 420°C for various lengths of time (16h, 24h, 48h). Modified solutionizing was also done, which included 4h at 420°C, 1h at 350°C and 12h at 420°C. After the solution heat treatment, all samples were quenched in water at 20°C. Annealing was conducted at 210°C for various lengths of time.

Samples for the tensile tests were machined to a diameter of 12 mm and tested on the Zwick 1476 tensile test machine at ambient as well as at elevated temperatures (100° and 120°C).

Tensile test parameters are as follows:

- Pre-stress: 2 N/mm^2
- Velocity for E-modulus: 5 N/mm^2s
- Velocity for the tensile and yield strength: 5 N/mm^2s
- Strain rate: 0,008 1/s

As magnesium alloys experience the gradual elastic-plastic transition, the point of yielding was determined as the initial departure from linearity of the stress-strain curve at the strain offset of 0,002.

In order to determine the hardness values of various samples, Brinell hardness and Vickers microhardness (0,005 kp/10s) tests were conducted.

Instrumented Charpy V-notch impact fracture testing was undertaken to predict fracture behavior. The impact fracture specimen has the shape of a bar of a cross section (10x10x55mm), into which a V-notch is machined. Impact fracture tests were made at ambient temperature.

7.3. Metallographic Studies

Metallography of magnesium alloys is a somewhat complicated issue, since the preparation procedure of samples for metallographic investigation differs greatly from that for aluminum alloys. The sample preparation procedure is presented in Table 7.2.

Discs of approximately 100µm in thickness and 3 mm in diameter were produced by a spark erosion cutter or an ultrasonic disc cutter. Pre-thinning was conducted by electrochemical methods of material removal, and final thinning was done by means of the ion thinning technique.

7.4. Neutron Diffraction Tests

Samples for the texture mesurements were machined from both deformed and non-deformed regions of tensile test samples. Samples had a cylindrical form with a diameter of 10 mm and a height of 10 mm. Texture measurements were conducted in the Center for Fundamental and Applied Neutron Research in Rez near Prague. The neutron flow was approximately 10^5 neutrons per second and per square centimeter. As a monochromator a zinc monocrystal was used, so that a wave length of 0.144 nm with a maximum divergence of $\delta \approx 1°$ was obtained. The diffractometer is equipped with a He-detector (Ø 93mm) and allows for a resolution of $\Delta d/d \leq 2.8 \times 10^{-2}$. The measurements of pole figures were made using the reflex method with a mesh of 5x5 degrees. The calculations of ODF were made using POPLA-Software.

Table 7.2. Sample preparation procedure

Grinding on the SiC-paper with water cooling			
SiC - Grain Size	Pressure	Time	U/min
180 (70µm)	~ 6 bar	1 min	300
320 (35µm)			
500 (10µm)			
1200 (3µm)			
Polishing with Alcohol			
3 µm	~ 6 bar	3 min	150
1µm			
Etching			
Microstructure	5 ml HNO_3, 100 ml Alcohol, ~ 30 seconds		
Microstructure	5 ml HF, 95 ml Alcohol, ~ 30 seconds		
Grain Boundaries	5 ml HNO_3, 100 ml Alcohol, ~ 30 seconds		

7.5. Stress Relaxation and Damping Tests

Samples for the stress relaxation and damping tests were machined from the bars of sand cast magnesium alloy AZ91. For the comparison, properties of the gravity die cast sample (diameter 20mm) were also measured. Sand cast bars were the same bars as those used for mechanical testing. All tests were conducted at the Institute für Werkstofftechnik und Werkstoffkunde at the Technical University of Clausthal. Both the damping and the stress relaxation measurements were carried out on bending specimens 10 mm wide, 129 mm long and 4 mm thick. The designation of stress relaxation and damping samples is given in Table 7.3 below. The test sample is schematically presented in Fig. 7.4. The procedure of stress relaxation and damping measurements is extensively described by P. Buchhagen and W. Riehemann [65, 66, 70, 71].

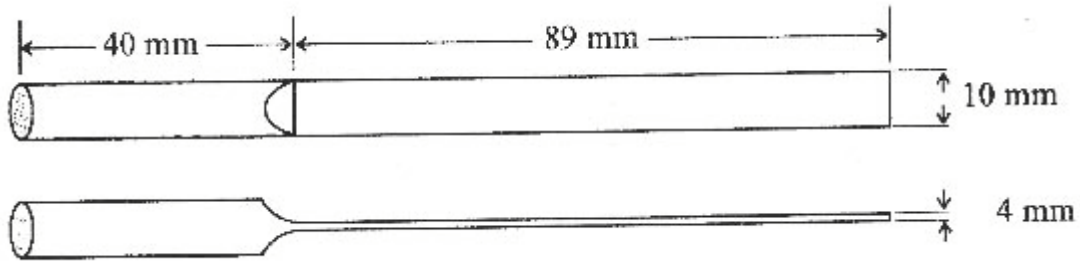

Fig. 7. 4. Stress relaxation and damping samples

Stress relaxation measurements were conducted on a modified commercial electrodynamic balance with a resolution of 1mg (E1200S) manufactured by Sartorius, Göttingen, FRG (Fig. 7.5). The temperature of the experimental set-up was kept constant at 31 ± 0,02°C. Stress relaxation was determined over the time period t_1 = 3s to t_2 = 3030s.

Damping measurements were carried out in a vacuum of about 30 Pa at ambient temperature. Damping was measured as the logarithmic decrement of the decay of the amplitude of the vibrating specimen. The experimental set-up is presented in Fig. 7.6. A permanent magnet is screwed onto the free end and enters an exciting and receiving coil. The beam is excited into resonance (200 to 250 Hz) by the permanent magnet and

the sinusoidal alternating current flowing in the exciting coil. After reaching a definite amplitude the coil is switched off by a PC and the declining mechanical vibration is stored in the PC via an ADC measuring the voltage induced by the moving permanent magnet. The logarithmic decrement δ is then calculated by the PC.

Table 7.3. Parameters of the Samples

Nr.	Parameters of the Samples
0.1	Non-refined, As-Cast Condition, Sample Diameter 16mm
0.2	Non-refined, As-Cast Condition, Sample Diameter 50mm
0.3	Grain-refined, As-Cast Condition, Sample Diameter 16mm
0.4	Die Cast Sample, Diameter 20mm
1	Non-refined, T4 for 16h @ 420°C, quenched in water @20°C
2	Non-refined, T4 for 48h @ 420°C, quenched in water @20°C
3	Non-refined, T6 for 16h @ 420°C, quenched in water @20°C , 4h @ 210°C
4	Non-refined, T6 for 48h @ 420°C, quenched in water @20°C , 4h @ 210°C
5	Non-refined, T6 for 48h @ 420°C, quenched in water @20°C, 16h @ 210°C
6	Grain-refined, T4 for 17h (420, 350°C), quenched in water @ 20°C
7	Grain-refined, T6 for 17h (420, 350°C), quenched in water @ 20°C, 4h @ 210°C

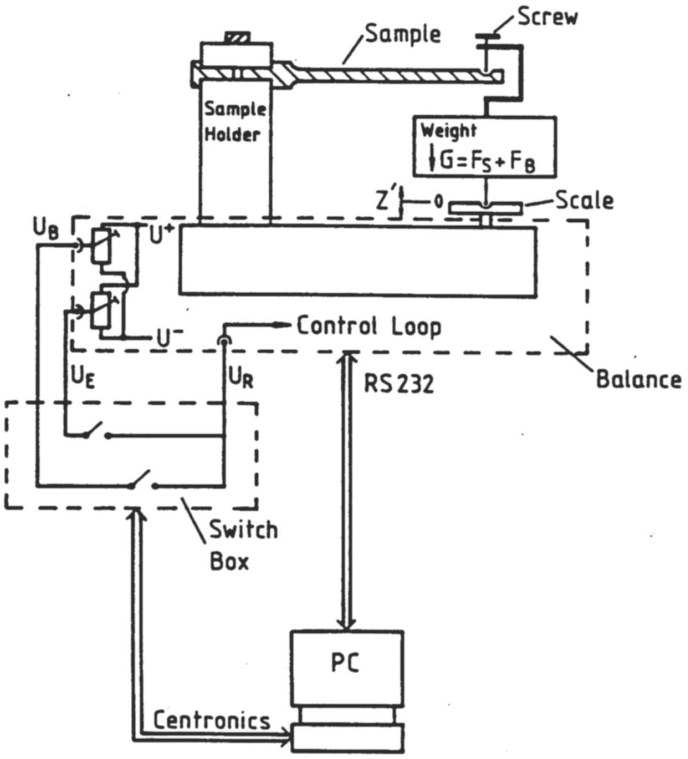

Fig. 7.5. Schematic drawing of experimental set-up [71].

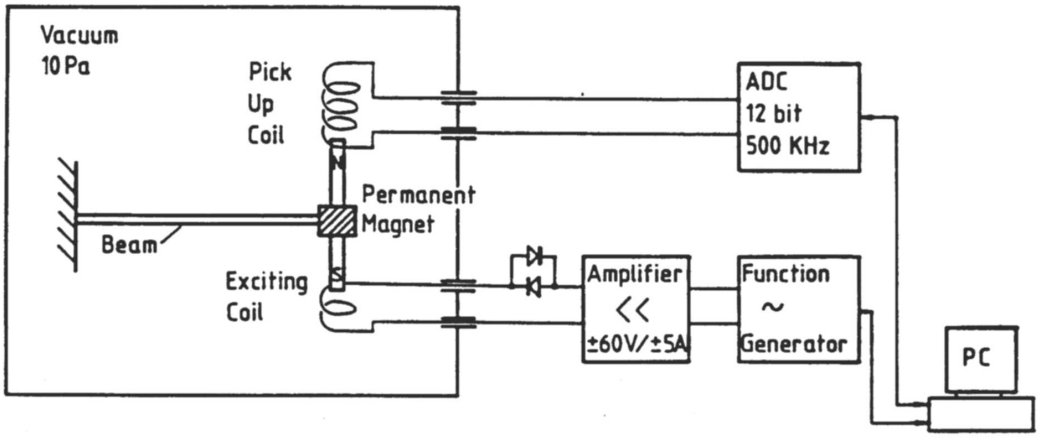

Fig. 7.6. Schematic drawing of the experimental set up for the determination of the logarithmic decrement δ of mechanical vibrations [71].

8. Results and Discussion

8.1. Results of the Filtration Tests

These tests were conducted with the samples, machined from the German aeronautic standard castings, both modified and non-modified. The purpose of these tests was to obtain the mechanical properties of the sand cast samples in the as-cast condition, without any grain refiner additions and to investigate the influence of the gating system, filter type and filter pore size. For a comparison, tensile test samples were also machined from the sprues of Casting 1. Results of these tests are presented in Table 8.1 and in Figure 8.1. After tensile tests, fracture surfaces of the samples were investigated by means of a scanning electron microscopy.

Table 8.1. Results of the Filtration Tests[1]

Nr.	Type of Casting, Filter type as shown in Fig. 7.3	Rm, MPa	$R_{p0,2\%}$, MPa	A_5, %
1	Casting 1, Sprue	84	69	1,4
2	Casting 2, no filter installed	142	86	1,6
3	Casting 2, Filter Nr. 6	146	83	2,2
4	Casting 2, Filter Nr. 4	149	101	1,7
5	Casting 2, Filter Nr. 5	151	89	2
6	Casting 1, no filter installed	159	97	2,7
7	Casting 2, Filter Nr. 1	160	96	2,6
8	Casting 2, Filter Nr. 2	167	96	2,9
9	Casting 2, Filter Nr. 3	171	99	3,4

It is clear from Table 8.1 that the best combination of mechanical properties was obtained with the 20 mm thick ceramic foam filter with a pore size 30 ppi. On the contrary, the worst combination of properties was obtained in samples machined from the sprue. Low mechanical properties in these samples are caused by strong turbulence during the mold filling and by the presence of large oxide films, as shown in Fig. 8.2.

[1] Average value from at least four samples.

Since such oxides were not observed on the fracturegraphs of the other samples, it was suggested that these were the primary oxides introduced from the crucible.

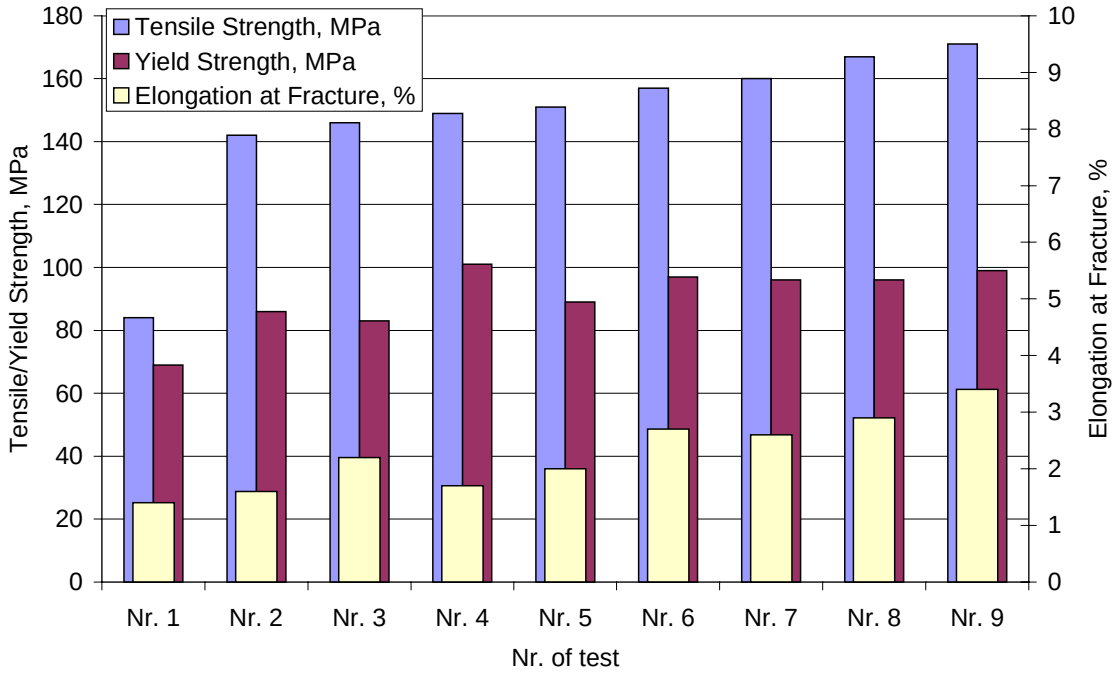

Fig. 8.1. Influence of the gating system, filter size and filter type on the mechanical properties of AZ91 sand cast samples (Sample diameter 16 mm)

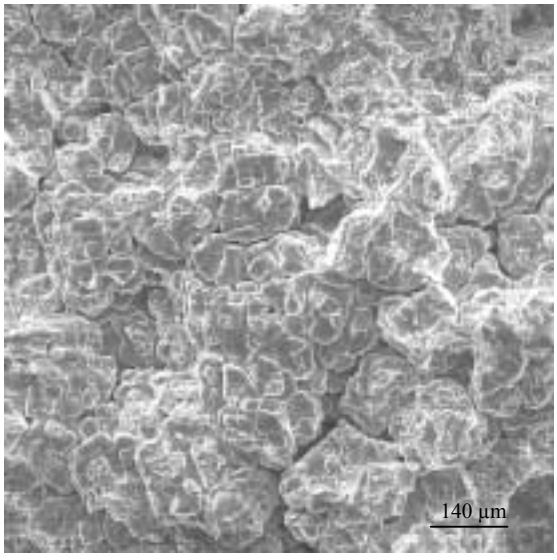

Fig. 8.2. Large oxide films found on the fracture surface of the sample machined from the sprue.

Properly chosen gating systems as those in Casting 1, may improve tensile strength by 10% and the elongation by 67%, even when no filter is installed. The runner of Casting 1 was cut and studied by light microscopy. It has been found out that the lower part of the runner was free of oxides, while in the upper part large oxide films were captured, as shown in Figure 8.3. The possible explanation is that the floating takes place in this gating system. Because dross is lighter than the liquid metal, it floats to the top of a still pool or a quietly moving stream of metal. By reducing the velocity of the metal in the runner (due to enlargement of the runner cross sections) and by allowing it to flow a sufficient distance before it reaches the gates, it is possible to skim the dross from the metal stream before it enters the mold cavity. The floatation mechanism is most effective when the runner is completely full of metal; unless the runner is full, dross continues to float down the metal stream. Runners can be kept full when the runner system is confined to the level below the mold cavity [85].

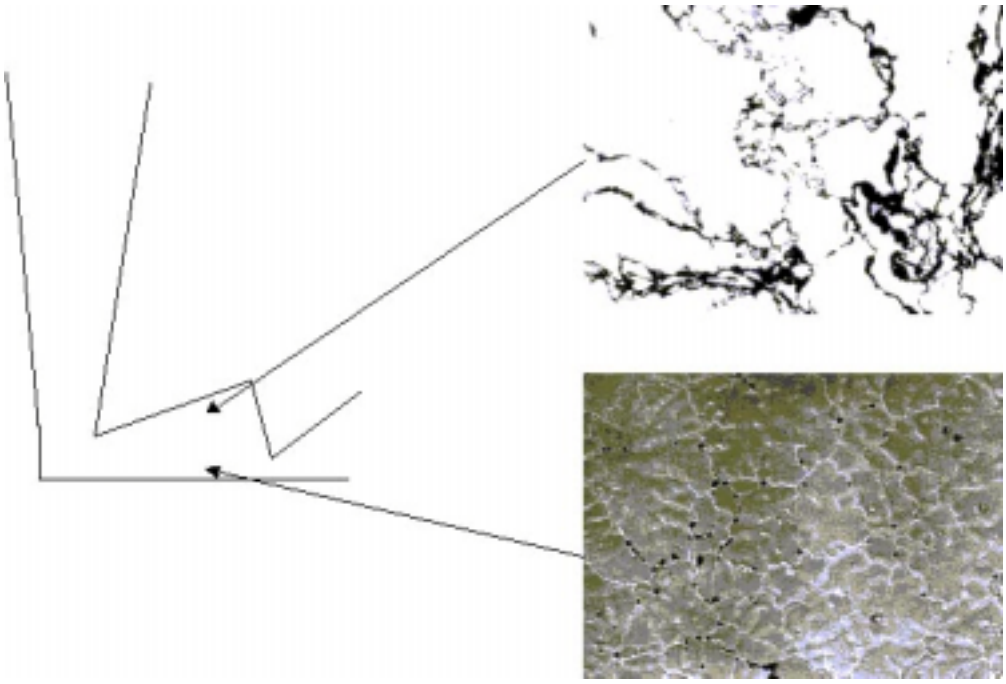

Fig. 8.3. Schematic presentation of the runner in the Casting 1.

Studies of the fracture surface of the samples from the Casting 1 have revealed that non-metallic inclusions are present in the core regions of tensile bars as well as in the surface regions (Fig. 8.4, Fig. 8.5). Dross in the bulk metal of the sample was possibly introduced during casting, while the inclusion in the surface regions of the bars probably stem from a reaction between the magnesium melt and the molding material.

The chemical composition of various inclusions is presented in Table 8.2. A closer look at this table reveals that some inclusions may originate from a reaction between the silicon sand of the mold and molten magnesium. This shows how important the choice of mold coatings is.

Table 8.2. Composition of non-metallic inclusions found on the fracture surfaces of AZ91 sand-cast samples

Mg	O	Si	Al	Cl	K	Ca	S	Fe	Ti	Zn
37,42	55,4	0,82	4,11	1,66	0,59	-	-	-	-	-
0,53	61,28	4,42	4,42	0,62	0,47	17,75	9,54	-	0,97	-
2,54	23,33	2,86	1,70	52,82	2,00	8,15	1,26	4,36	0,06	0,92
0,59	57,37	17,38	15,33	-	0,38	5,95	-	0,36	2,64	-

The gating system of the Casting 2 was specially designed for the installation of filters. Though the runner cross section also significantly enlarges and a lot of dross is captured in upper parts of the runner, the gating system is not effective enough. A large amount of contaminated metal flows through the runner before it is completely full of metal and before the floatation mechanism starts working. Therefore, the mechanical properties of the samples machined from Casting 2 (Nr. 2) are the worst in comparison to all other samples.

The installation of a steel wool filter consisting of several layers of woven steel wire leads to the 27% increase in the elongation at fracture values and to the very modest (3%) increase in the tensile strength. The obtained mechanical properties are still inferior to those achieved in Casting 1. This underscores the importance of the gating system design when casting magnesium. SEM studies of the steel wool filters have revealed, however, that large oxides and dross particles were captured by the filter (Fig. 8.6).

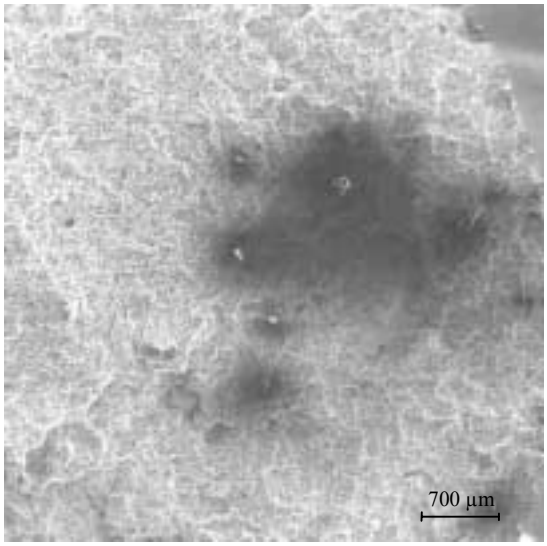

Fig. 8.4. Non-metallic inclusions on the fracture surface of the AZ91 samples.

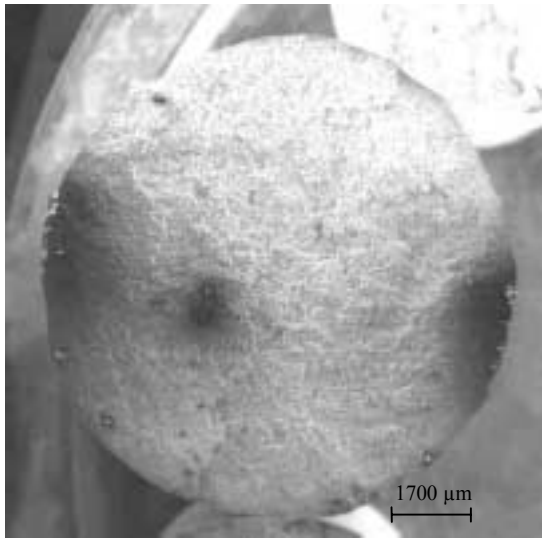

Fig. 8.5. Non-metallic inclusions stemming from reactions between magnesium melt and molding material, X6

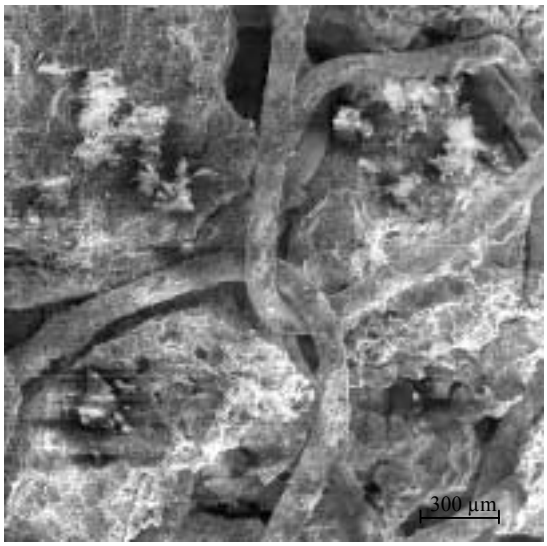

Fig. 8.6. Oxides and dross particles trapped by the steel wool filter.

Fig. 8.7. Reaction layer on the steel wire and trapped non-metallic inclusions.

Here, an interesting observation was made. Though it is generally accepted that steel wire filters mainly have a mechanical retention action on dross and that steel is not wetted by molten magnesium, a reaction layer build-up on the steel wire was observed (Fig. 8.7). The chemical composition of this layer, as revealed by EDX studies, was 0,76%S, 6,95%O, 3,91%Na, 13,60%Fe and 74,78%Zn. This layer may possess better wetting than steel and thus allow for the retention of dross in a liquid state.

Relatively low mechanical properties achieved with steel wool filters may be caused by the presence of small oxides, originating from large primary oxides, which were "milled" by the steel sieve and by the hydrostatic pressure of the molten metal. Another reason for the lower mechanical properties in comparison to the properties achieved when ceramic foam filters were used is the much lower retention of dross in the liquid state. The SEM studies on the interfaces between ceramic foam filter Nr. 3 and metal matrix have shown relatively thick layers of non-metallics adhering to the ceramic surface of the filter (Fig. 8.8). On the fracture surface of these samples, no non-metallic inclusions were found. The comparison between the fracture surfaces of the gating system after and before the filter is shown in Fig. 8.9. The dross may be clearly seen on the fracture surface before the filter. A blank metallic fracture was obtained in the gating system after the filter.

The higher efficiency of the ceramic foam filters may be explained by the structure of these filters. Almost 90% of the volume of the filters consists of open interconnected pores. As the melt passes through the filter, the direction and the velocity of the melt flow change many times, causing intensive contact with the ceramic surface of the filter. Due to this contact, even the particles of a much smaller diameter than the average pore sizes are captured in the filter.

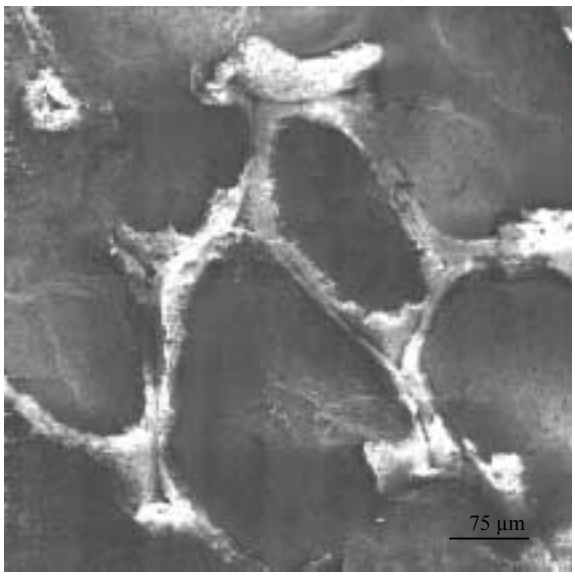

Fig. 8.8. Dross adhering to the ceramic foam filter.

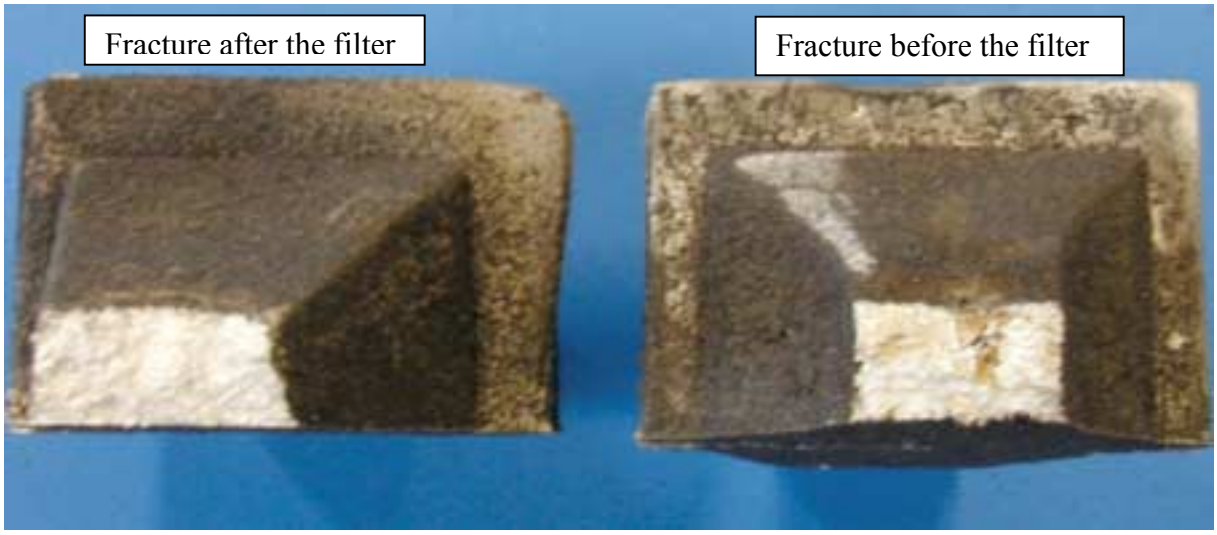

Fig. 8.9. Comparison of the fracture surfaces of the gating system before and after the filter.

The thickness of the filter plays an important role. As the results of test Nr. 7 show, filter 1 (with a thickness of 20 mm) renders the tensile strength of 160 MPa and an elongation at fracture of 2,2%, while filter 2 (with the thickness of 14 mm) renders the tensile strength of 149 MPa and an elongation at fracture of 1,7%: a decrease of 7 and 23%, correspondingly. Greater thickness of the filter allows for a longer flow-through distance and results in more contact between the ceramic foam surface and the melt.

Another important factor is the pore size of the filter. A decrease in the pore size of the filter from 10 ppi to 30 ppi results in the increase of the tensile strength from 160 to 171 MPa and an increase in the elongation at fracture from 2,6 to 3,4% (7% and 30%, correspondingly). Smaller pore size means an automatically higher internal surface and thus, a more intensive contact between the melt and the filter.

The results of the filtration tests have clearly revealed that the mechanical properties may be improved due to the application of a carefully designed gating system and due to the application of filters. Though the mechanical strength values only increase minimally (compare the results of tests Nr. 2 and Nr. 7), elongation at fracture more than doubles.

Steel wool filters were shown to be ineffective in comparison to the ceramic foam filters. A higher filter thickness and smaller pore size both increase the efficiency of the filtration, and thus, the mechanical properties.

8.2. Results of the Grain Refinement Tests

Grain refinement tests were conducted with the samples machined from Casting 2. Two sample diameters were investigated – 16 mm and 50 mm. A ceramic foam filter with a pore size of 30 ppi and a thickness of 20 mm was installed (Comp. Fig. 7.3). The choice of this filter is explained by the fact that in this case the negative influence of the non-metallic inclusions on the mechanical properties is eliminated and only the grain refiner addition to the melt may influence the properties. The grain refiner hexachlorethane, titanium carbide and activated carbon were chosen. When samples were refined with titan carbide, only 16 mm diameter samples were investigated, since the preliminary results have revealed low efficiency of this grain refinement method. Grain refinement with various additions of activated carbon – 0,3, 0,6 and 0,9 wt.-% has rendered no strengthening effect but caused the melt to ignite. Results of the grain refinement tests are presented in Table 8.3 and in Figures 8.10, 8.11 and 8.12.

The general trend when refining with titanium carbide is the deterioration of tensile strength and elongation at fracture and a slight improvement of yield strength with increasing TiC-additions. Tensile strength decreases by approximately 12%, elongation by 53%, while yield strength increases by 21%.

The efficiency of the grain refinement with hexachlorethane, which is state-of-the-art in the industrial practice today, depends largely on the wall thickness. In the case of the 16 mm diameter samples, the highest tensile and yield strength, as well as the highest elongation at fracture values were obtained with moderate 0,6 weight-% additions of hexachlorethane. In the case of the 50 mm diameter samples, a 2 weight-% addition of hexachlorethane rendered the best mechanical properties.

The 0,6 weight-% C_2Cl_6 addition to the 16 mm diameter samples renders a 12% increase in both tensile and yield strength, and a 12% increase in elongation at fracture values. Further hexachlorethane additions of up to 2 weight-% resulted in consequent deterioration of all mechanical properties, with the exception of the yield strength. In comparison to the non-treated melts, a 23% increase of yield strength was achieved with a 1,2 weight-% addition of C_2Cl_6.

Table 8.3. Results of the grain refinement tests with TiC- and C_2Cl_6-additions[2].

Grain refiner, Weight- %	Sample diameter, mm	Tensile Strength, MPa	Yield Strength, MPa	Elongation at Fracture, %
Non grain refined	50 mm	97	83	0,7
	16 mm	171	98	3,4
0,3% TiC	16 mm	160	115	2,3
0,6% TiC	16 mm	149	116	1,9
0,9% TiC	16 mm	150	119	1,6
0,3% C_2Cl_6	50 mm	122	96	0,8
	16 mm	188	106	3,6
0,6% C_2Cl_6	50 mm	127	98	0,9
	16 mm	192	110	3,8
0,9% C_2Cl_6	50 mm	139	98	1,1
	16 mm	178	108	2,8
1,2% C_2Cl_6	50 mm	118	90	1,3
	16 mm	169	121	2,5
2% C_2Cl_6	50 mm	139	107	1,7
	16 mm	165	118	2,6

In comparison to the 16 mm diameter sand cast samples, grain refining with 2 weight-% of C_2Cl_6 of the 50 mm diameter samples brought up a much higher increase in properties, since the tensile strength rose 43%, yield strength increased by 29%, and elongation at fracture more than doubled (143% up). Smaller hexachlorethane additions immediately improved tensile strength, while leaving yield strength and elongation almost unchanged. The 0,6 weight-% addition increased the elongation only marginally – by 14%.

[2] Average value from at least four samples.

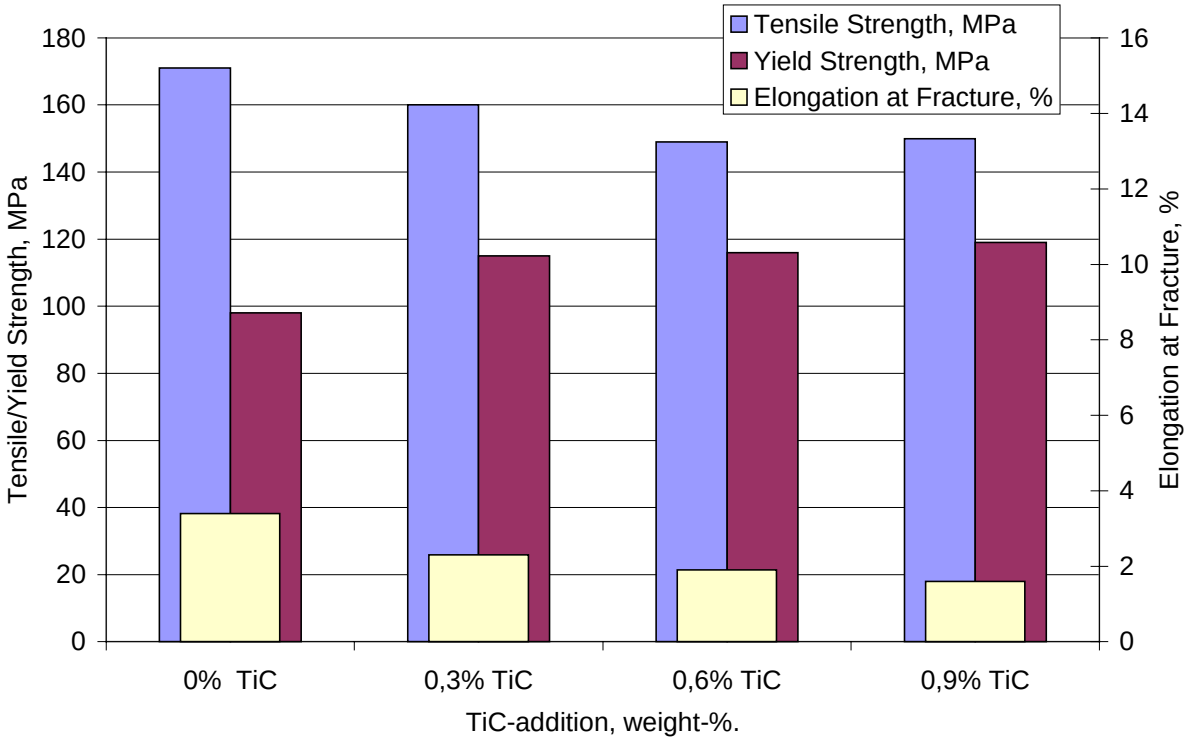

Fig. 8.10. Influence of the TiC-addition on the mechanical properties of AZ91 sand-cast samples (Sample diameter 16 mm).

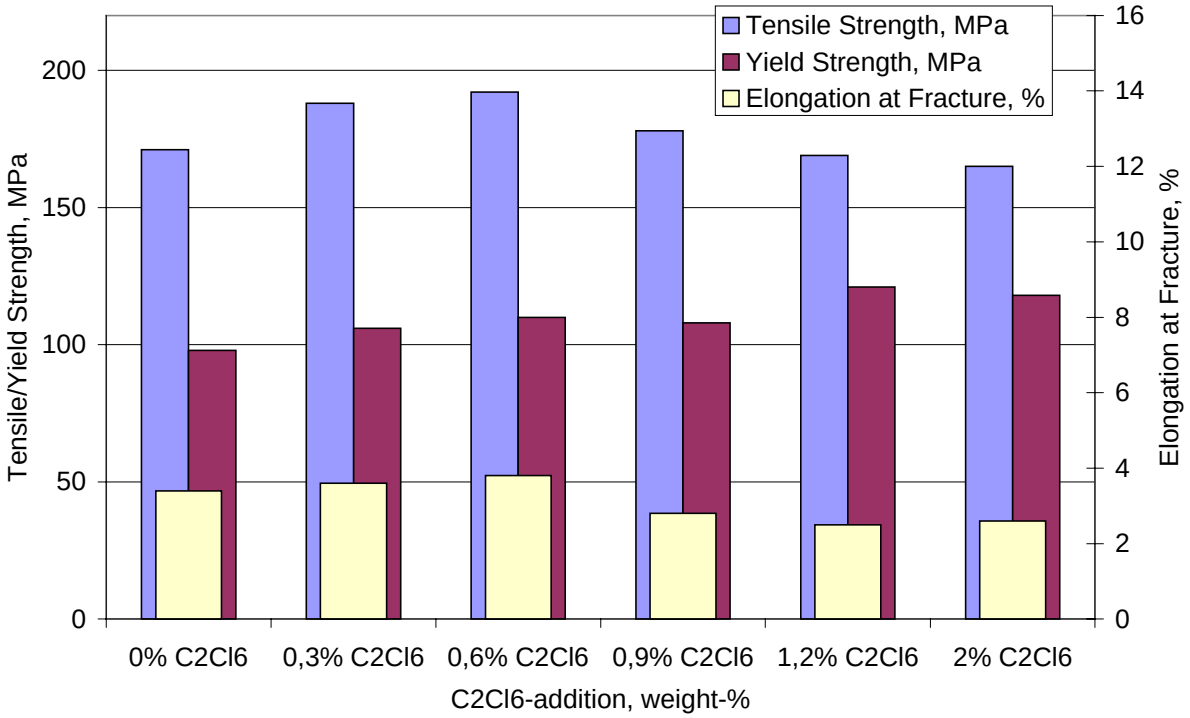

Fig. 8.11. Influence of the C_2Cl_6-addition on the mechanical properties of AZ91 sand-cast samples (Sample diameter 16 mm).

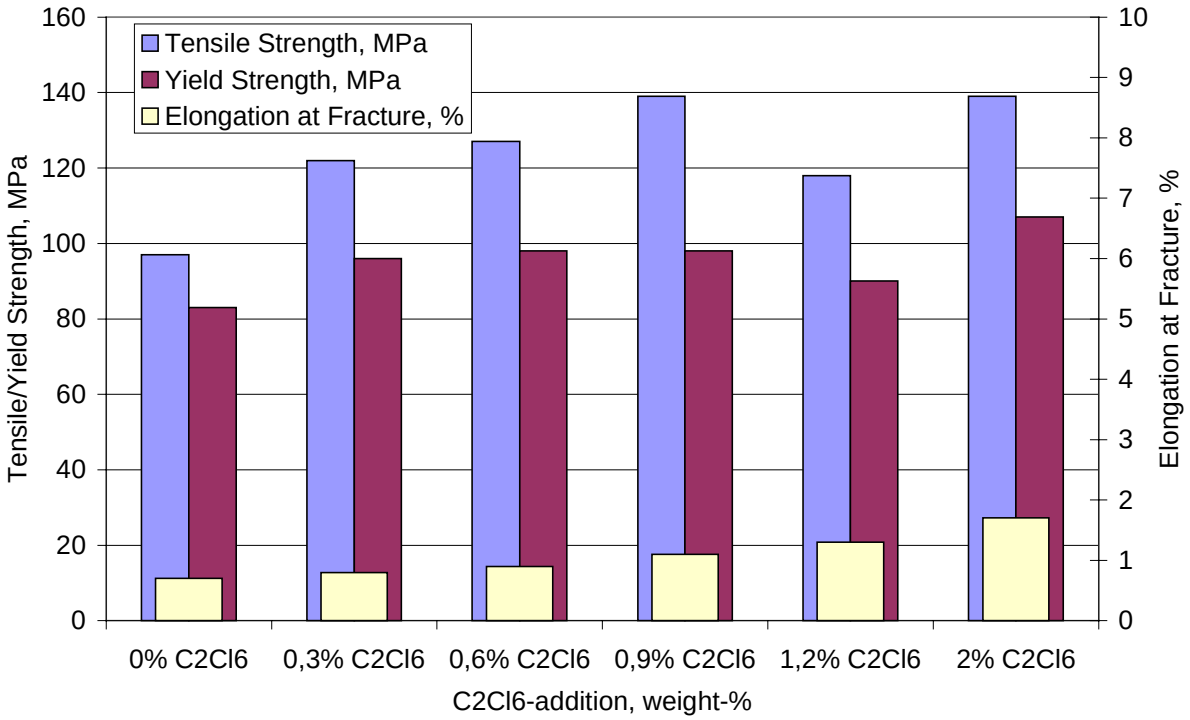

Fig. 8.12. Influence of the C_2Cl_6-addition on the mechanical properties of AZ91 sand-cast samples (Sample diameter 50 mm).

The generally lower mechanical properties of the 50 mm diameter samples can be explained by the inherent microporosity. AZ91 is the long freezing range alloy possessing a mushy state solidification pattern, and though it is possible to somewhat decrease the microporosity grade by means of risers and chills, i.e. by promoting directional solidification, our experience has revealed that it is almost impossible to achieve sound castings with wall thicknesses of more than 20 mm. The microstructure of the 50 mm diameter sample is shown in Fig. 8.13.

In order to establish a clear interdependence between the grain refiner addition and the mechanical properties, grain size measurements were conducted. Results of these measurements are presented in Table 8.4 and in the Figures 8.14 a- 8.14 f.

It may be seen that in the non-grain refined samples, a small fraction of grains (approximately 15% of all grains) has a very large percentual amount of the sample volume. Therefore, we may suggest that a bimoidal grain volume distribution is present here.

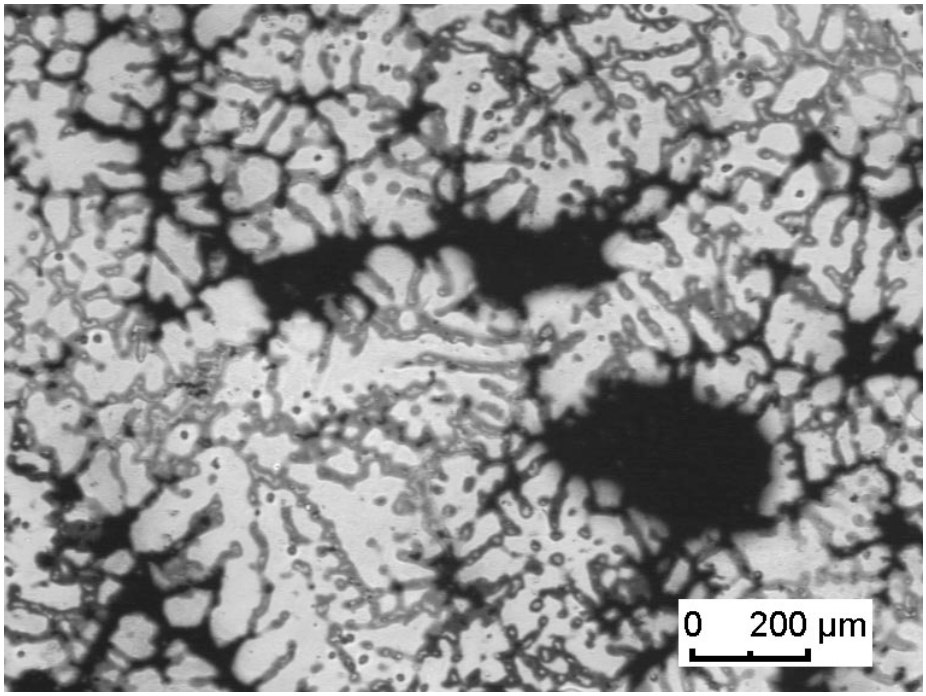

Fig. 8.13. Microporosity in the 50 mm diameter sample.

Table 8.4. Mean grain size of AZ91 sand cast samples[3]

C_2Cl_6-addition, weight-%.	50 mm sample diameter				16 mm sample diameter			
	Min, µm	Max, µm	Mean Grain Size, µm	Std. Deviation	Min, µm	Max, µm	Mean Grain Size, µm	Std. Deviation, µm
0% C_2Cl_6	8,34	891,95	283,36	158,58	3,26	626,69	152,84	103,86
0,3% C_2Cl_6	3,28	347,8	120,21	54,6	4,37	272,33	82,45	34,63
0,6% C_2Cl_6	3,28	340,14	128,75	63,68	10,94	197,96	71,26	28,56
0,9% C_2Cl_6	20,78	290,92	113,53	45,21	2,19	202,34	78,31	31,34

Thus, it may be seen that the average grain size in the 16 mm diameter samples decreased by almost 55% with the 0,6 weight-% C_2Cl_6 addition, and in the 50 mm diameter samples mean grain size also dropped by 54%. Another important effect of the grain refinement is the tightening of the average grain size distribution (compare Figures 8.14 a - 8.14 d for the 16 mm diameter samples, and Figures 8.14 e - 8.14 h for the 50 mm diameter samples).

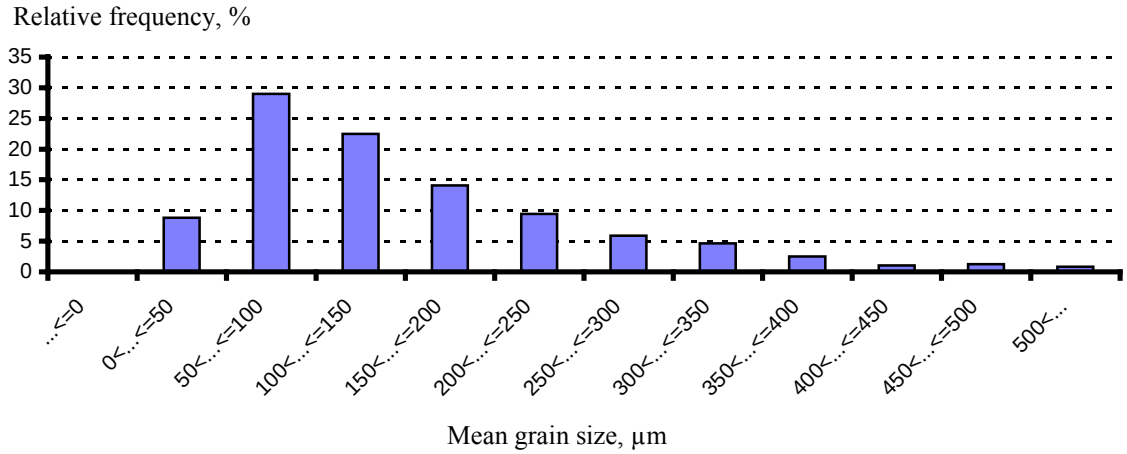

Fig. 8.14 a. Frequency distribution of grain size diameter of the non-grain refined 16 mm diameter AZ91 sand cast sample.

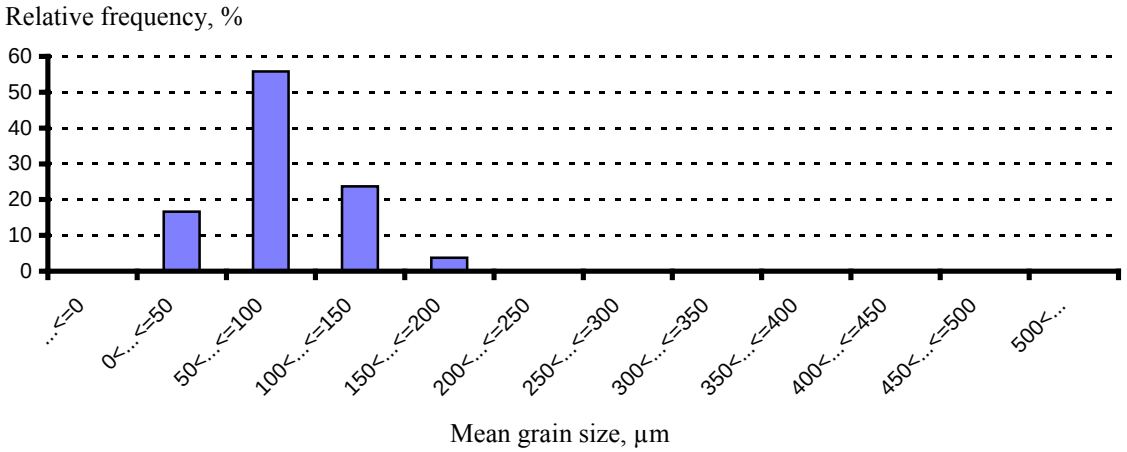

Fig. 8.14 b. Frequency distribution of grain size diameter of the grain refined 16 mm diameter AZ91 sand cast sample (0,3 weight-% C_2Cl_6-addition).

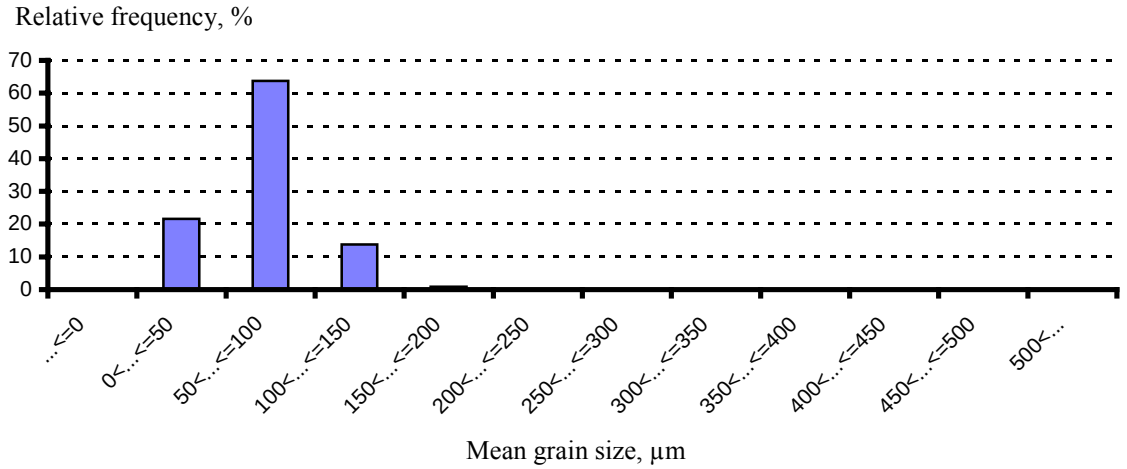

Fig. 8.14 c. Frequency distribution of grain size diameter of the grain refined 16 mm diameter AZ91 sand cast sample (0,6 weight-% C_2Cl_6-addition).

[3] Mean value of at least 8 measurement fields

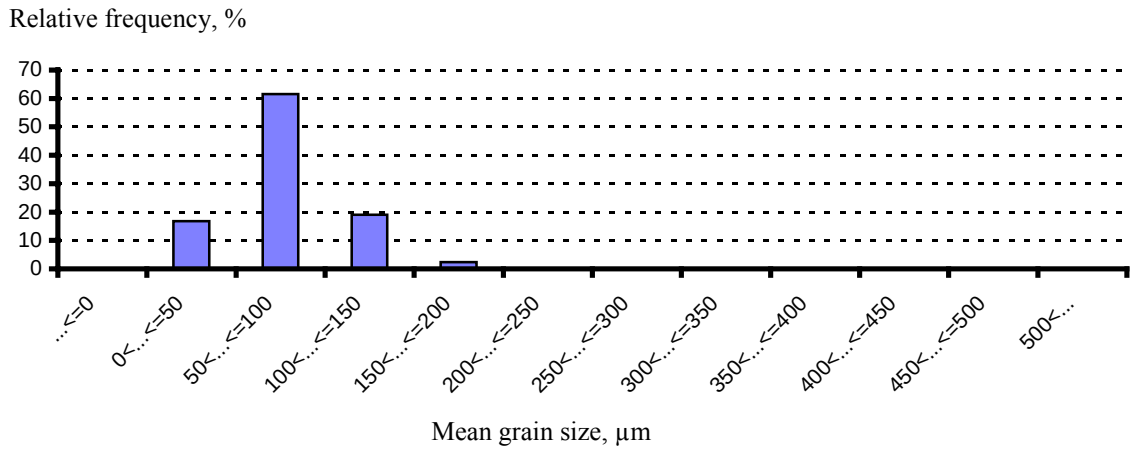

Fig. 8.14 d. Frequency distribution of grain size diameter of the grain refined 16 mm diameter AZ91 sand cast sample (0,9 weight-% C_2Cl_6-addition).

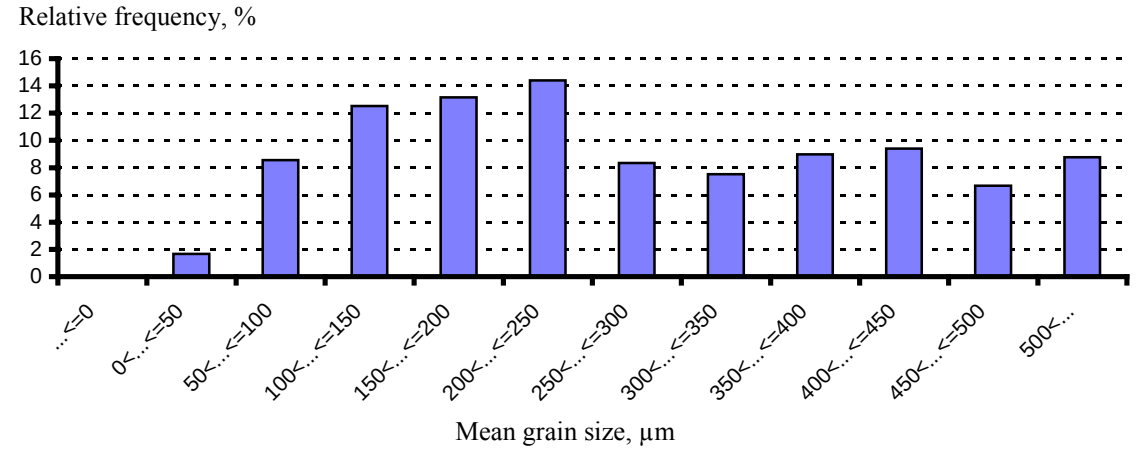

Fig. 8.14 e. Frequency distribution of grain size diameter of the non-grain refined 50 mm diameter AZ91 sand cast sample.

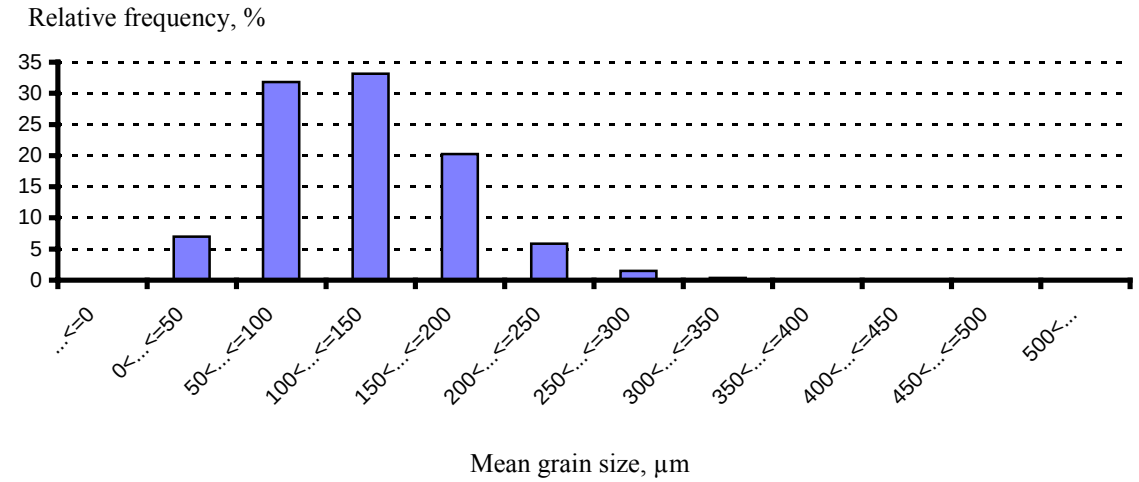

Fig. 8.14 f. Frequency distribution of grain size diameter of the grain refined 50 mm diameter AZ91 sand cast sample (0,3 weight-% C_2Cl_6-addition).

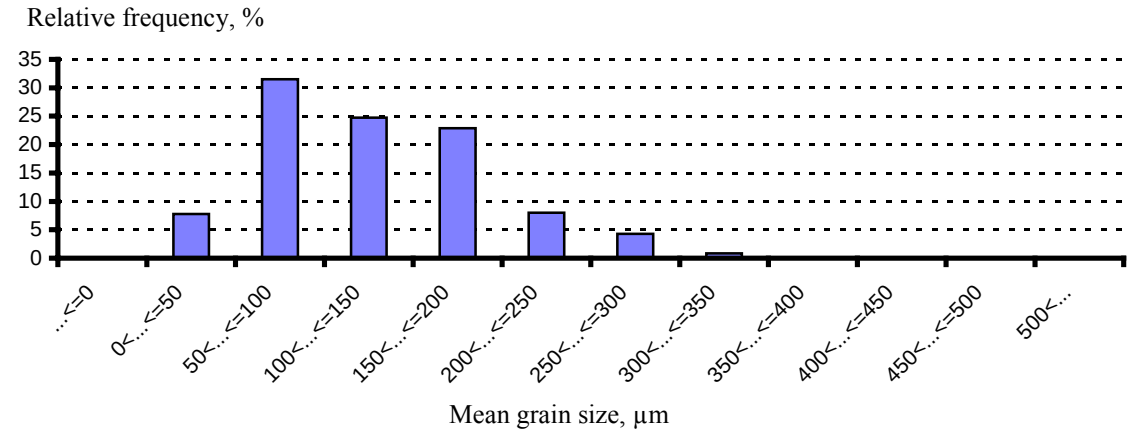

Fig. 8.14 g. Frequency distribution of grain size diameter of the grain refined 50 mm diameter AZ91 sand cast sample (0,6 weight-% C_2Cl_6-addition).

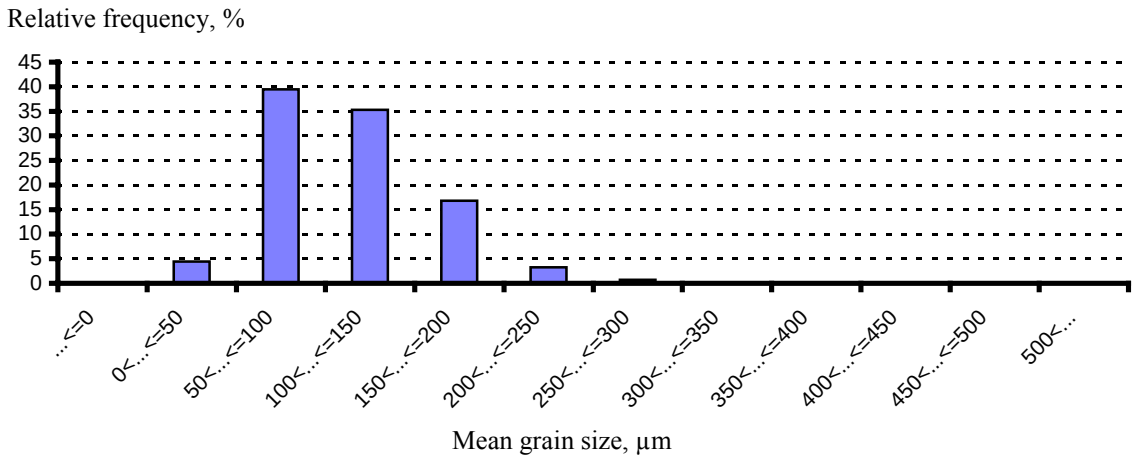

Fig. 8.14 h. Frequency distribution of grain size diameter of the grain refined 50 mm diameter AZ91 sand cast sample (0,9 weight-% C_2Cl_6-addition).

Interestingly, the dramatic drop of the average grain size did not cause a large increase in yield strength, as was expected. In certain steels, for example, a similar percentual decrease of the average grain size would result in a 30% to 50% increase in yield strength. However, it should be taken into consideration that not the percentual decrease, but rather the inverse square root of the average grain size is of greatest importance from the point of view of the Hall-Petch relationship.

The results of the melt treatment with hexachlorethane and activated carbon could not offer the explanation of the causes of the grain refining effect in aluminium-containing magnesium alloys. The theory that the grain refinement is caused by Al_4C_3-particles was not proven, since the properties did not change at all after the melt treatment with

activated carbon. However, it should be noted that the activated carbon granules did not dissolve in the melt, and were captured by the filter. But since the necessary amount of carbon for the grain refinement is supposed to be very small, it could be suggested that the minute carbon particles (such as carbon dust) could be dissolved and thus lead to the grain refining effect. Moreover, in comparison to earlier casting practices where the melting was conducted in grey iron crucibles and a certain diffusion of silicon and/or carbon into the melt could be responsible for the grain refinement, we conducted our melting in plain steel crucible. The studies, conducted by Siebel in 1948 [101] also tried to provide a direct link between various process parameters and the resulting grain refinement effect. In order to avoid the possible grain refinement effect caused by iron, Siebel produced melts in graphite crucibles, superheated the melts and also achieved grain refinement effect. The question is, how did he avoid reactions between magnesium melts and graphite? Siebel also undertook various grain refinement tests with chlorine and chlorine containing elements, such as C_6Cl_6, C_2Cl_6 and $C_6H_6Cl_6$ and has found that chlorine by itself was sufficient as a grain refining agent. It is unclear, however, in which crucibles (cast iron or graphite) these tests were conducted. The degassing of magnesium melts was given as the reason for the increasing strength .

Our tests were conducted in plain steel crucibles (carbon and silicon diffusion into the melt are avoided), under protective gas (no hydrogen could be introduced into the melt) and with the HP (high-purity) alloys, which have very low amounts of impurities, such as iron or silicon.

Activated carbon was introduced into the melt deliberately and caused no property improvement. Can we therefore, conclude, that the formation of Al_4C_3 (even if it took place) is the cause of the grain refinement? Or is it the degassing of magnesium melt by chlorine from C_2Cl_6? The hydrogen could be introduced into the pig metal during the manufacturing under protective salt melts.

It is, therefore, still unclear from our results if the carbon or chlorine are the main grain refining agent for the aluminium-containing magnesium alloys. The results, obtained by Siebel, show, however, that the tensile strength of 270 MPa, yield strength of 140 MPa, and the elongation at fracture of 14% was achieved in the as-cast condition in the 20 mm diameter samples (compare to 230 MPa, 120 MPa and 7%, correspondingly,

without any grain refiner additions). The last provocative question is whether the standard, non high-purity alloys (containing higher percentual amounts of iron) could be a better alternative from the point of view of properties to the new, much more expensive high-purity alloys?

In conclusion, grain refining improved the properties of sand cast AZ91, but not to the extent that we suggested. Since the magnesium alloy castings currently manufactured are relatively thin-walled (in most cases), the 0,6 weight-% hexachlorethane addition can be sufficient. However, melt treatments with hexachlorethane is not environmentally friendly and it may be expected that hexachlorethane will soon be banned from foundries. Therefore, it is necessary to investigate other possibilities of property improvement, such as heat treatment.

8.3. Results of the Heat Treatment Tests

Heat treatment practices, either annealing and quenching (T4) or annealing and quenching, followed by aging (T6), both cause serious changes in the microstructure of the alloy. To begin with, let's study the microstructure of the 16 mm and 50 mm sand cast samples in the as-cast condition (Fig. 8.15 and 8.16). Structure constituents are marked by arrows. Microhardness of various structure constituents is presented in Fig. 8.16.

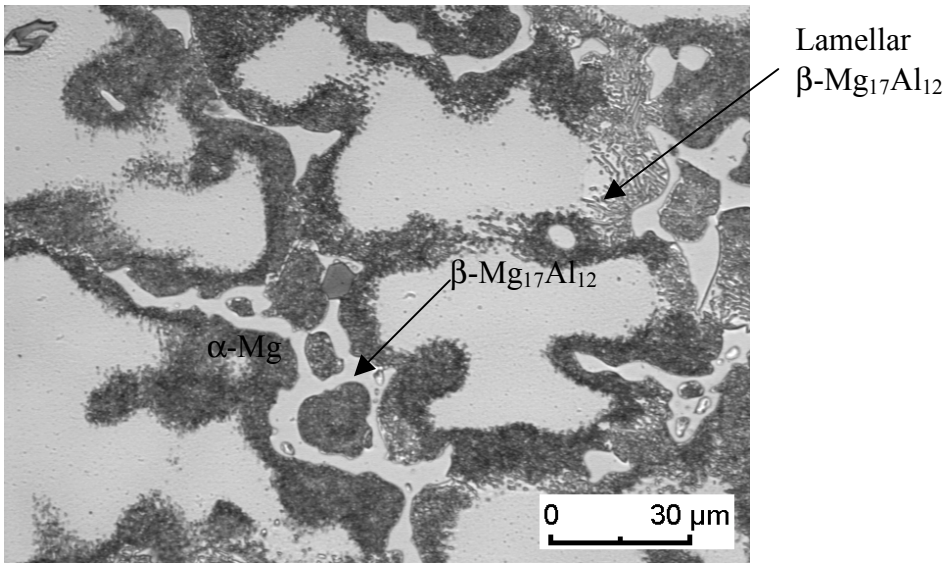

Fig. 8.15. Microstructure of the 16 mm diameter sample in the as-cast condition.

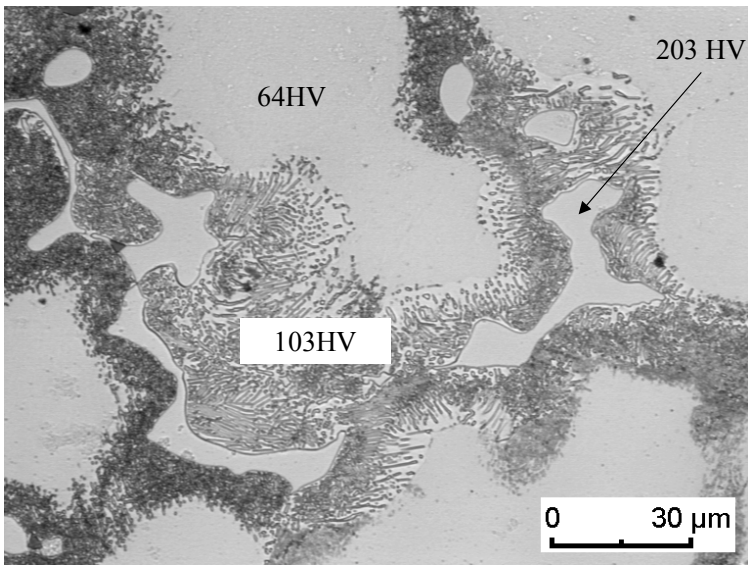

Fig. 8.16. Microstructure of the 50 mm diameter sample in the as-cast condition with microhardness values of various structure constituents.

It is clear that the microstructure of the 50 mm diameter sample is much coarser than that of the 16 mm diameter sample. The amount of the lamellar eutectoid $Mg_{17}Al_{12}$ is much more pronounced in the 50 mm diameter sample since the lower cooling rate allows for the precipitation of the eutectoid constituent. In the case of the 16 mm diameter sample, Mg-rich coring at the grain boundaries is present in higher quantities than single eutectoid $Mg_{17}Al_{12}$ precipitates. Higher solidification and cooling rate also caused higher saturation with aluminium atoms, thus strengthening the α-magnesium matrix. The microhardness measurements in the microstructure of the 50 mm diameter sample has shown that the β-$Mg_{17}Al_{12}$ has the highest hardness between all microstructural constituent, with 203 HV, while the softest constituent is the α-Mg with 64 HV.

Transmission electron microscopy studies were conducted on the samples machined from 16 mm bars and interesting results were obtained. Results of the TEM studies are presented in Fig. 8.17 –8.19.

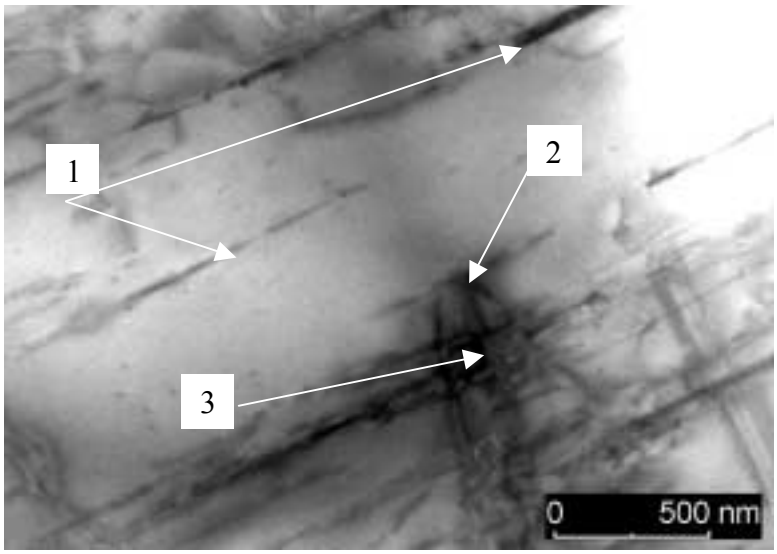

Fig. 8.17. Microstructure of the sand-cast AZ91 sample showing various microfeatures:
1 – minute precipitations, presumably $Mg_{17}Al_{12}$
2 – dislocation source
3 – dislocations.

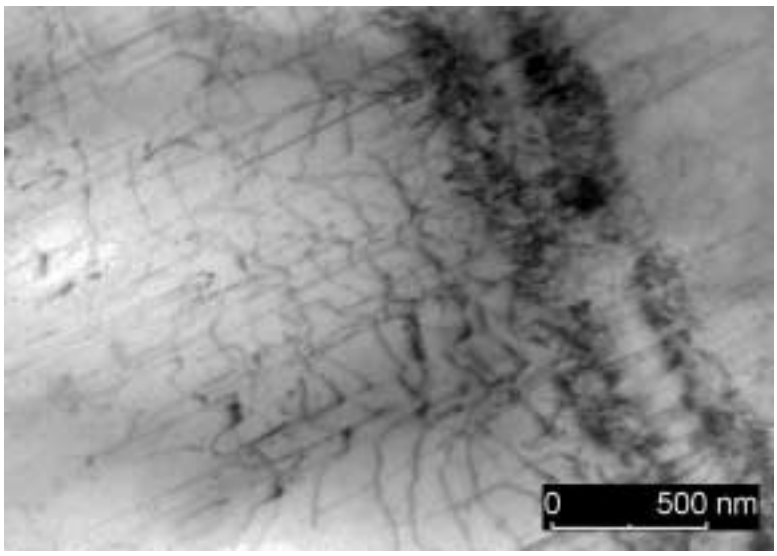

Fig. 8.18. Dislocations pile-up at the twin boundary of the AZ91 sample in the as-cast condition.

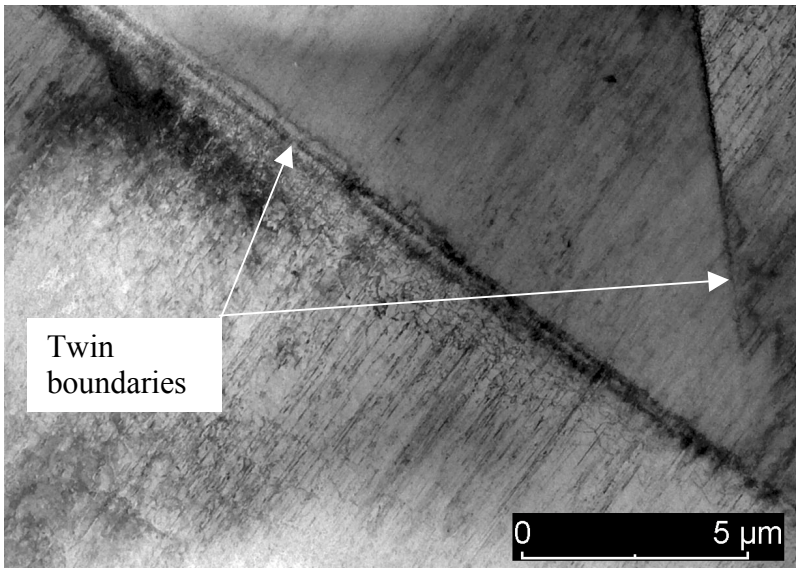

Fig. 8.19. Twin boundaries in the microstructure of the sand-cast AZ91 sample in the as-cast condition.

Figure 8.17 shows the presence of minute particles of presumably $Mg_{17}Al_{12}$-phase (1) which precipitated from the supersaturated α-Mg as a result of "aging" at ambient temperature. The presence of such particles in the as-cast condition was never described in the literature, however, this could be predicted. It may be concluded that certain age-hardening effects may take place in the thin-walled samples after a prolonged period of time. Indirectly, this effect was proven in the measurement of damping properties of the

as-cast samples when damping tests of the same sample were undertaken on different days.

Figure 8.18 presents an interesting picture of the dislocation pile-up at the twin boundaries. Twin boundary thickness is approximately 500 nm. In Fig. 8.19, two twin boundaries may be seen. The angle between the twin boundaries is about 40°. The twin formation occurred due to the thermal stresses in casting. The very high dislocation density, shown in Fig. 8.18 and 8.20 may also be caused by high thermal stresses during the cooling of the castings (the castings used in this study are very "rigid", which means that they underlay high thermal stresses during cooling). Furthermore, in comparing the results of the tensile tests of the non-heat treated samples (Table 8.3), we may come to the conclusion that this high dislocation density is the possible reason for the low values of elongation at fracture and relatively high values of microhardness, as shown later on in Table 8.8. Moreover, high dislocation density may be responsible for the relatively low efficiency of grain refinement, i.e. high strength values were already obtained in the as-cast condition, and grain refinement only insignificantly improved mechanical properties.

The fracture behaviour is, to a largest extent, determined by the microstructure. The fracturegraphs of the 16 mm and 50 mm samples are presented in Fig. 8.20 and 8.21.

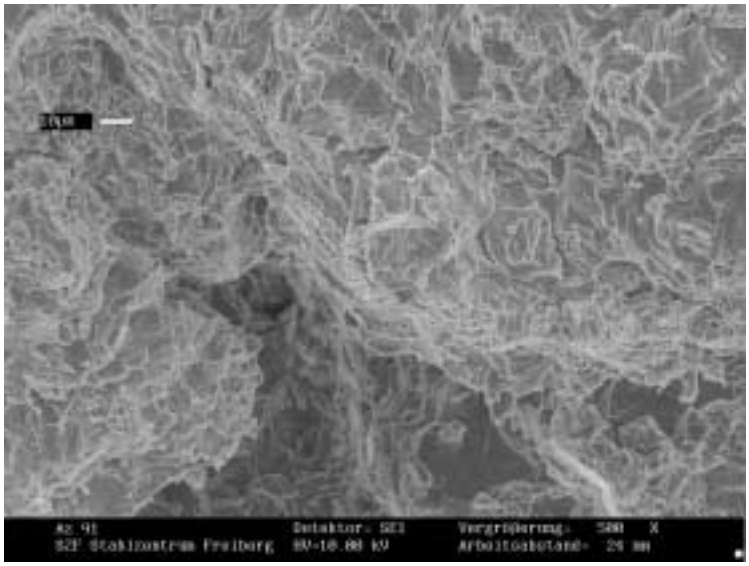

Fig. 8.20. Fracturegraph of the 16 mm diameter AZ91 sand-cast sample in the as-cast condition.

Fig. 8.21 shows a much coarser fracture surface of the 50 mm diameter sample in comparison to the 16 mm diameter sample. However, there is no principal difference between the fracture modes of the two samples – the brittle fracture dominates in both cases. Since the 50 mm diameter sample has larger grains of α-Mg, surrounded with β-$Mg_{17}Al_{12}$ phase, the fracture surface appears much coarser and resembles glass splinters.

The fracture studies of the as-cast AZ91 samples are very interesting. Magnesium itself is the hexagonal close-packed (HCP) metal and usually shows brittle fracture because of the limited number of slip planes. In pure HCP metals, cracks propagate along cleavage planes under the stress normal to the cleavage planes. Most brittle fractures in polycrystalline metals are transgranular; i.e., the crack propagates across the matrix of the grains. However, brittle fracture can occur in an intergranular manner if the grain boundaries contain a brittle film or if the grain-boundary region has been embrittled by the segregation of the detrimental elements [34].

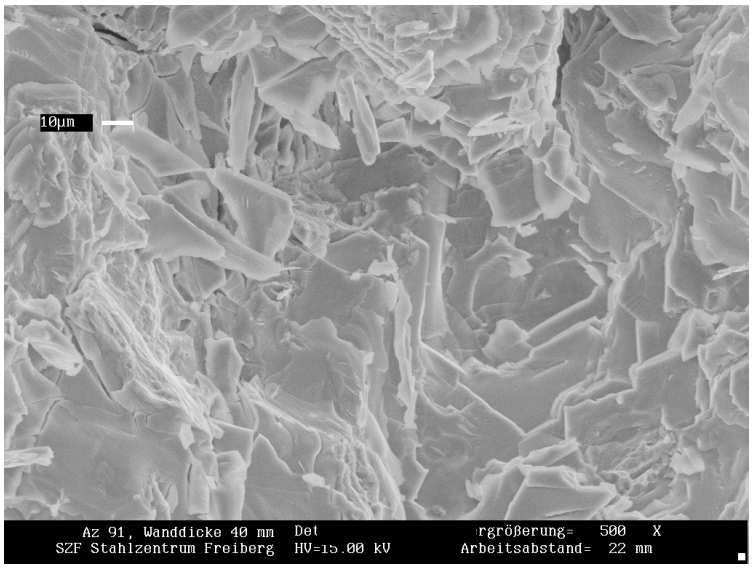

Fig. 8.21. Fracturegraph of the 50 mm diameter AZ91 sand-cast sample in the as-cast condition.

This brittle fracture mode in both samples let us conclude that the crack propagated across the brittle β-$Mg_{17}Al_{12}$-phase and cleavage planes of the as-cast microstructure. Thus, both of these factors play an important role in the fracture manner of the as-cast

AZ91. And the question arises: "What will happen if the brittle β-$Mg_{17}Al_{12}$ phase is dissolved in the α-Mg-matrix?"

The solution heat treatment causes the dissolution of the second phase precipitates and, generally, leads to the improvement of the ductility of the alloy. Solution heat treatment tests and later on the aging tests were undertaken with both grain refined and non-grain refined samples. The solutionizing procedure with the non-grain refined samples included the heating up to 420°C and solutionizing for 16, 32 and 48h without any pause, followed by quenching in water at 20°C. The modified heat treatment included heating up to 420°C, solutionizing at 420°C for 4 hours, lowering the heat treatment temperature to 350°C and maintaining this temperature for 1 hour. Then, the temperature was increased to 420°C and samples were solutionized for another 12 hours at this temperature. Quenching was made in water at 20°C. Lowering the heat treatment temperature for 1 hour during the solutionizing should avoid or, at least, reduce possible grain growth.

Results of the solution heat treatment tests conducted with the non-grain refined samples are presented in Table 8.5 and in Figures 8.22 and 8.23.

Table 8.5. Results of the solution heat treatment tests (T4)[4]

Heat Treatment Time, hours	Sample diameter, mm	Tensile Strength, MPa	Yield Strength, MPa	Elongation at fracture, %
0 h	50 mm	97	83	0,7
	16 mm	171	98	3,4
16 h	50 mm	112	66	1,4
	16 mm	236	87	9
32 h	50 mm	118	68	1,7
	16 mm	228	87	8
48 h	50 mm	120	65	1,8
	16 mm	232	87	8,3

[4] Average value from at least four samples

The results of these tests show that both tensile strength and the elongation at fracture values increase in 16 mm as well as in 50 mm diameter samples already after 16 hours of solutionizing at 420°C. Increasing the duration of the solutionizing to 32 hours and 48 hours also leads to an increase in the tensile strength and an elongation for the 50 mm diameter samples, but not to the same extent as after 16 hours of heat treatment. The tensile strength increased by 38%, and the elongation at fracture increased by 165% after 16 hours at 420°C for the 16 mm diameter sand cast samples. Yield strength decreased by approximately 13%. Interestingly, after 32 hours and 48 hours, both tensile strength and elongation slightly decreased in the 16 mm diameter samples. The peak in the tensile strength values for the 50 mm diameter samples was reached after 48 hours, and the percentual increase was 24% in comparison to the as-cast condition. Elongation at fracture values also reached a maximum of 1,8% after 48 hours of solutionizing, up 157% compared to the as-cast condition.

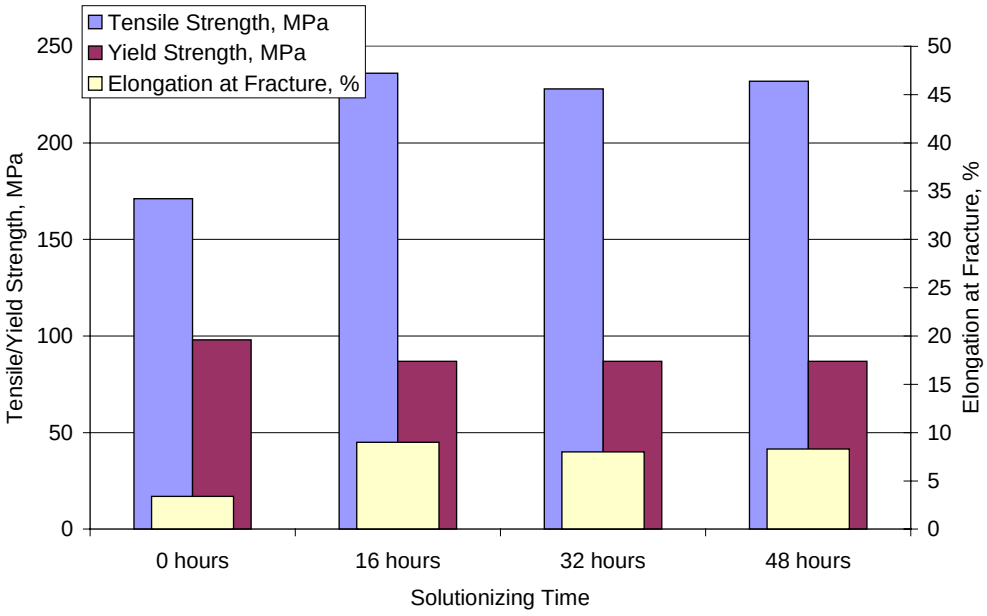

Fig. 8.22. Influence of the duration of the solution heat treatment at 420°C on the mechanical properties of the non-grain refined AZ91 sand-cast samples (Sample diameter 16 mm).

These results led us to the conclusion that 16 hours of solutionizing heat treatment may be sufficient for the relatively thin-walled castings, and that for the thick-walled casting longer solutionizing times are necessary. Metallographic studies of heat-treated samples rendered answers to this phenomenon.

The amount of the β-phase in the microstructure of the 16 mm and 50 mm diameter samples is schematically presented in Fig. 8.24.

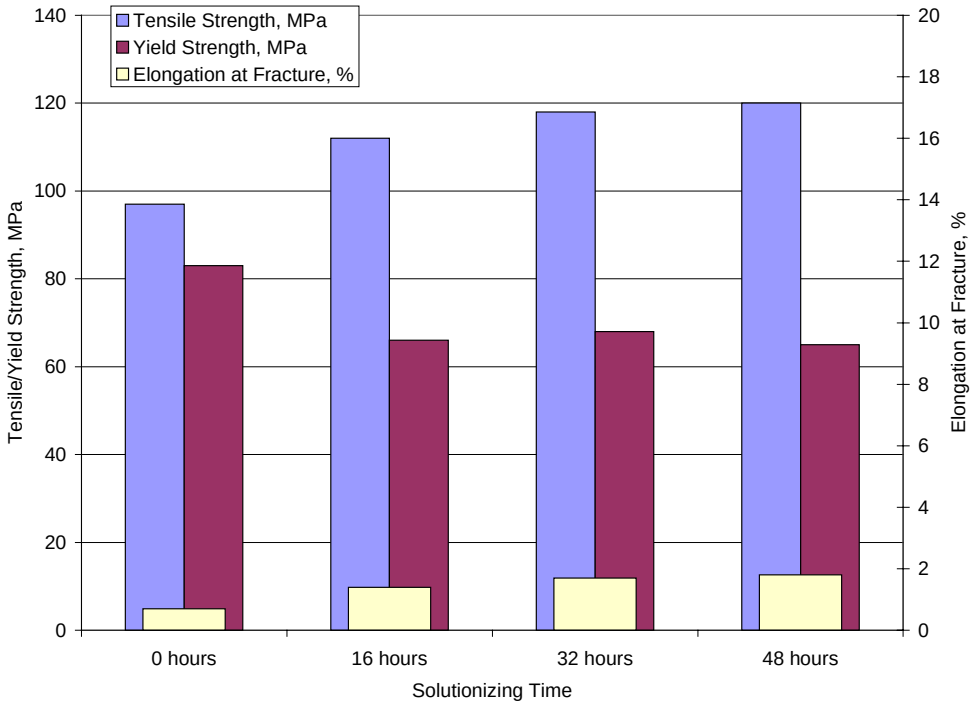

Fig. 8.23. Influence of the duration of the solution heat treatment at 420°C on the mechanical properties of the non-grain refined AZ91 sand-cast samples (Sample diameter 50 mm).

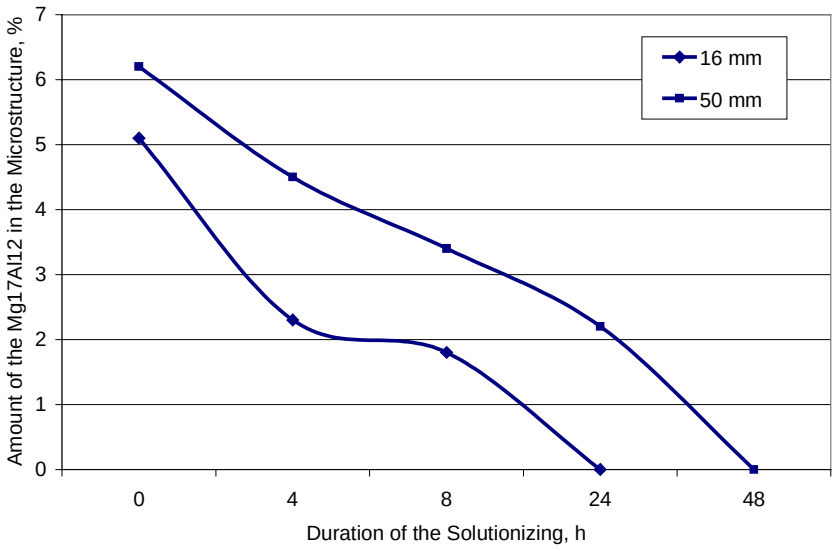

Fig. 8.24. Amount of the β-$Mg_{17}Al_{12}$ in the microstructure of the 16 mm and 50 mm diameter samples vs. duration of the solutionizing.

Since the as-cast microstructure of the 50 mm diameter samples is much coarser than that of the 16 mm diameter samples, it takes longer to bring all of the β-$Mg_{17}Al_{12}$ particles into a solid solution. The changes in the microstructure of the 16 mm diameter samples after 16, 32 and 48 hours are shown in Fig. 8.25-8.28. The comparison with the as-cast microstructure of samples, shown in Fig. 7.15 reveals that the lamellar eutectoid $Mg_{17}Al_{12}$ disappears first, and is no longer present in the microstructure after 16 hours of solution heat treatment. The microstructure becomes very homogenous, with small isles of hard β-$Mg_{17}Al_{12}$. After 32 hours of solution heat treatment, almost no β-$Mg_{17}Al_{12}$ particles are present in the microstructure, and after 48 hours, the microstructure is completely homogenized, as shown in Fig. 8.28. The microhardness of the α-magnesium solid solution gradually increases from 64 HV in the as-cast condition, reaching 70 HV in the completely homogenized state.

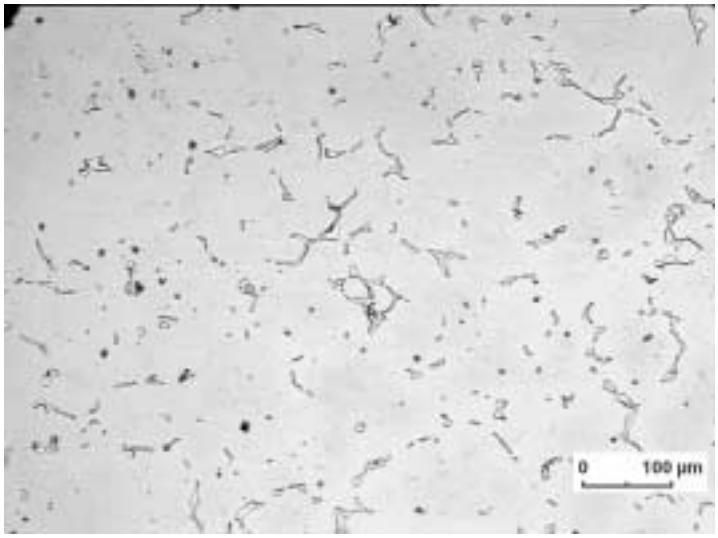

Fig. 8.25. The microstructure of a 16 mm diameter AZ91 sand-cast sample after 16 hours of heat treatment at 420°C.

The hard β-$Mg_{17}Al_{12}$ goes into the solution and the aluminium atoms, which have different size than the magnesium atoms, produce elastic strain fields, which interact with the strain fields of the moving dislocations. However, this effect is very small and does not cause an increase in the yield strength, as would be expected. Yield strength actually decreases, since the hard particles of β-$Mg_{17}Al_{12}$, which act as reinforcements in the matrix of an alloy, gradually disappear during solutionizing.

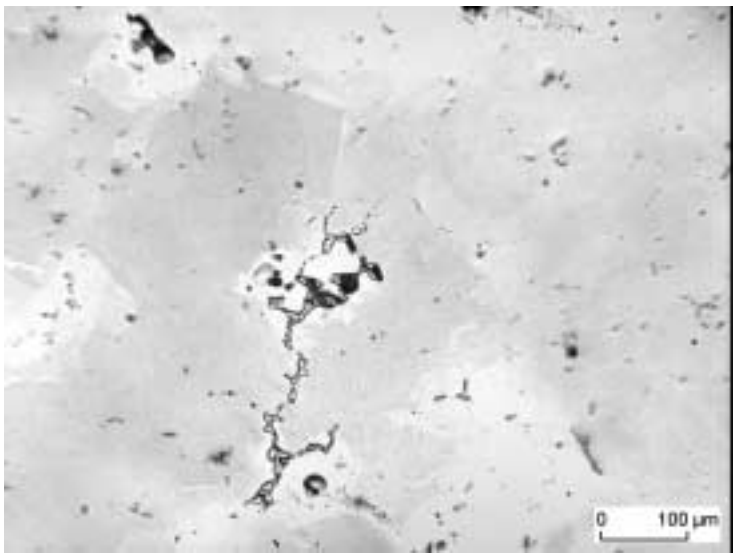

Fig. 8.26. The microstructure of a 16 mm diameter AZ91 sand-cast sample after 32 hours of heat treatment at 420°C.

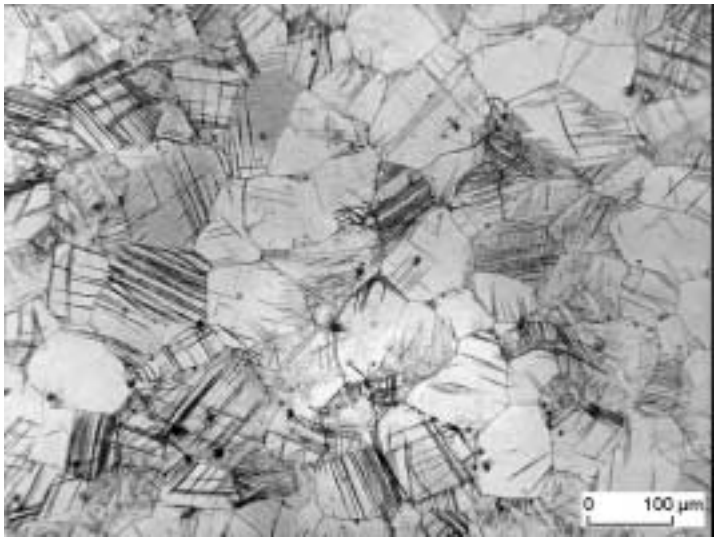

Fig. 8.27. The fine-grain microstructure of a 16 mm diameter AZ91 sand-cast sample after 48 hours of heat treatment at 420°C (T4).

Figures 8.27 and 8.28 are very interesting since they show the microstructures of two samples from the same casting. While the microstructure presented in Fig. 8.27 is relatively fine-grained, the microstucture in the Fig. 8.28 shows large differences in the grain sizes. Therefore, the statement that germination may be a problem when heat treating aluminium-containing magnesium alloys, was proven here. Germination is perhaps also the cause of the strong fluctuations in the mechanical properties of the sand-cast samples after 48 hours of the solutionizing heat treatment. So, the tensile

strength ranged from 206 MPa to 278 MPa, and the elongation at fracture ranged from 6,3% to 14,2%. After 16 hours of the heat treatment, the scatter of properties is much smaller, which is caused by the lower amount of germination that took place in the samples. Tensile strength values ranged from 231 MPa to 240 MPa, and the elongation at fracture fluctuated from 8,9% to 9%.

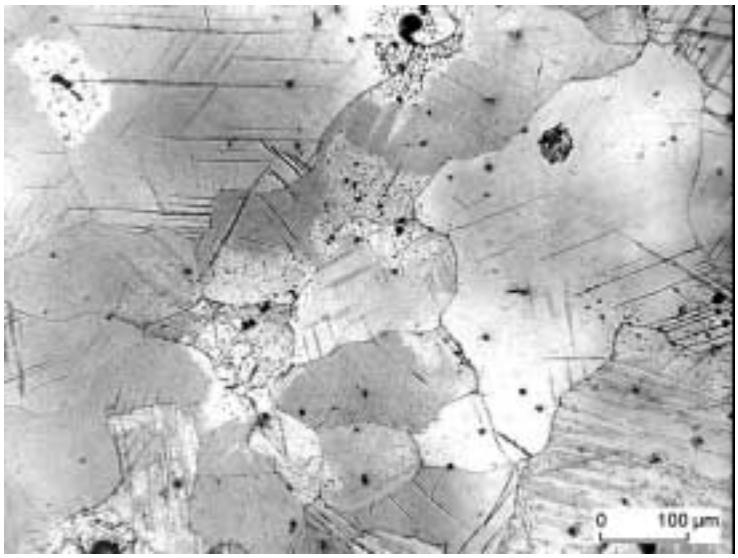

Fig. 8.28. The coarse-grain microstructure of a 16 mm diameter AZ91 sand-cast sample after 48 hours of heat treatment at 420°C (T4).

The microstructures presented in Fig. 8.27 and 8.28 stem from the non-deformed samples. Very astonishing is the high density of twins in these samples. Twinning may be caused by thermal stresses during the cooling of the samples. A closer look at these figures led us to the conclusions that the intermetallic phase precipitated at twin boundaries. The presence of the precipitates may be explained by aging at an ambient temperature, since the metallographical studies of these samples were conducted approximately one month after the heat treatment.

Grain size measurements were then conducted and frequency distributions of the grain size diameters for the samples heat-treated for 16 hours and 48 hours, correspondingly, are presented in Fig. 8.29 and 8.30.

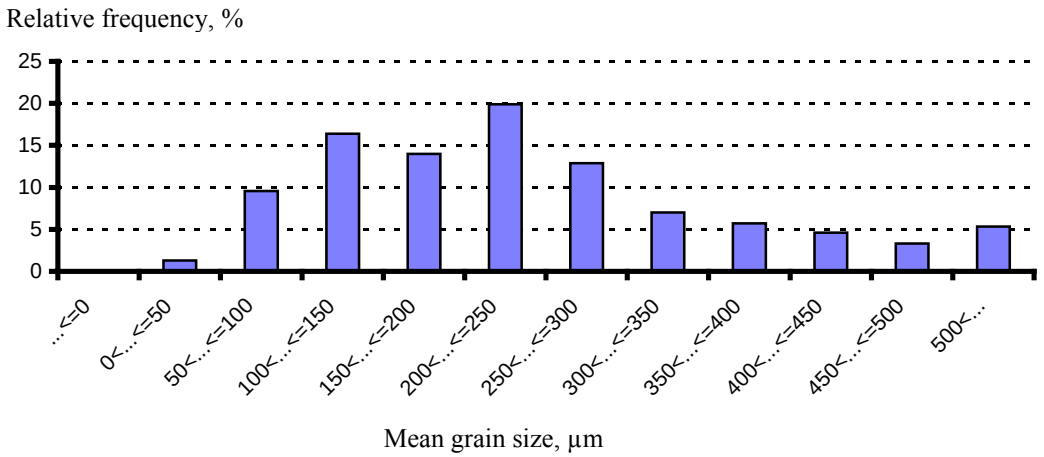

Fig. 8.29. Frequency distribution of grain size diameters of the non-grain refined 16 mm diameter AZ91 sand cast samples after solutionizing for 16 h at 420°C.

The results of the grain size measurement of the non-grain refined samples in the as-cast condition are presented in Fig. 8.14 a. The comparison between Fig. 8.14 a, 8.29 and 8.30 shows a marked increase in the large-sized grains (>500µm) as a result of the solutionizing. The mean grain size increased from 153µm in the as-cast condition to 242 µm after 16 hours and almost doubled to 287 µm after 48 hours. The standard deviation also rose from 103 in the as-cast condition to 199 after 48 hours. Schematically the increase in the grain size is shown in Fig. 8.31.

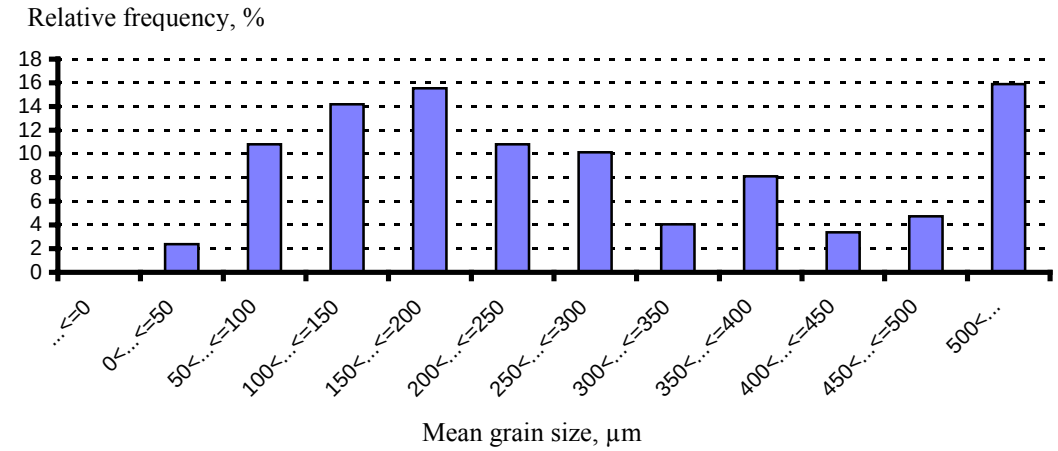

Fig. 8.30. Frequency distribution of grain size diameters of the non-grain refined 16 mm diameter AZ91 sand cast samples after solutionizing for 48 h at 420°C.

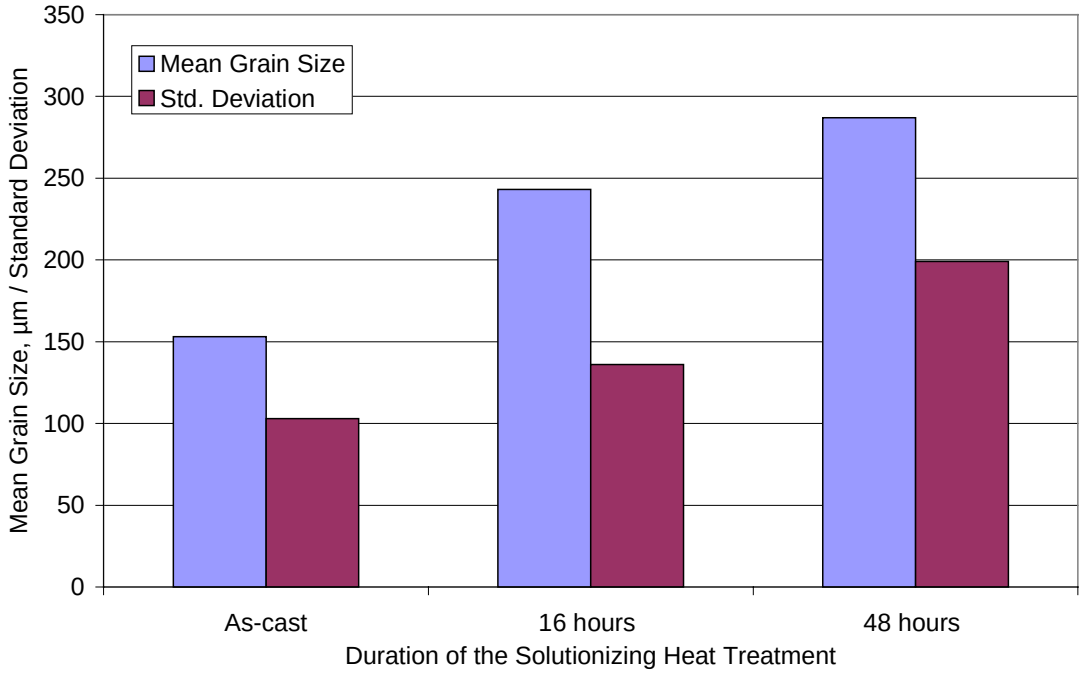

Fig. 8.31. Mean grain size of the 16 mm diameter non-grain refined sand cast samples versus duration of solutionizing treatment.

The grain growth phenomenon observed here is a typical case of the secondary recrystallisation. Usually all grain boundaries migrate at roughly equal rates, with the result that at any stage the grains are roughly uniform in size, but sometimes migration is restricted to only a minority of boundaries, so that a few grains grow very large at the expense of the others [34]. As this process is exaggerated in samples with largely varying grain size in as-cast condition (Fig. 8.14 a), it is not astonishing to observe such a large scatter of various grains as in Fig. 8.30.

The grain growth may be stopped by the presence of impurities and disperse phases [34]. However, large amounts of aluminium and zinc do not inhibit the grain growth process. Much more important is the presence of the disperse phase. Only a grain larger than its neighbour, (by at least 30%), can consume the latter with a decrease in the total boundary energy. The smaller the grains are, the more energetically favourable is their shrinkage. There are distinct critical energies (for a given volume fraction) that allow the growth of large grains and the disappearance of small grains. The critical particle size for inhibiting growth of large grains is proportional to the mean grain size. It can be seen that grain growth will not commence until particles have reached the critical size

Therefore, it may be concluded that small amounts of the β-$Mg_{17}Al_{12}$-phase in the microstructure may effectively hinder grain growth without being deleterious to strength and ductility.

Since the melt treatment with 0,6 weight-% of hexachlorethane sufficiently decreased grain size in the as-cast 16 mm diameter samples, a heat treatment test was also conducted with such samples. The heat treatment chosen was the modified heat treatment described above. For purposes of comparison, non-grain refined samples were also heat treated by this procedure. The resulting mechanical properties were measured and are presented in Table 8.6 and in Fig. 8.32, 8.33.

The obtained results are astonishing. First of all, modified solutionizing heat treatment resulted in a significant improvement of properties only in the 16 mm diameter grain refined samples. Tensile strength increased by 42% in comparison to the as-cast, grain-refined condition, while the elongation at fracture rose 247%. Furthermore, if we compare the mechanical properties of the grain-refined samples after the modified solutionizing heat treatment with the properties of the non-grain refined samples in the as-cast condition, we can see the 60% rise in the tensile strength and the 290% increase in the elongation at fracture.

Table 8.6. Results of the modified heat treatment tests (T4)[5].

Grain refined/non-grain refined	Sample diameter, mm	Tensile Strength, MPa	Yield Strength, MPa	Elongation at fracture, %
0% C_2Cl_6	50 mm	109	64	1,5
	16 mm	199	70	6
0,6% C_2Cl_6	50 mm	125	65	2
	16 mm	272	87	13

[5] Average value from at least 4 samples

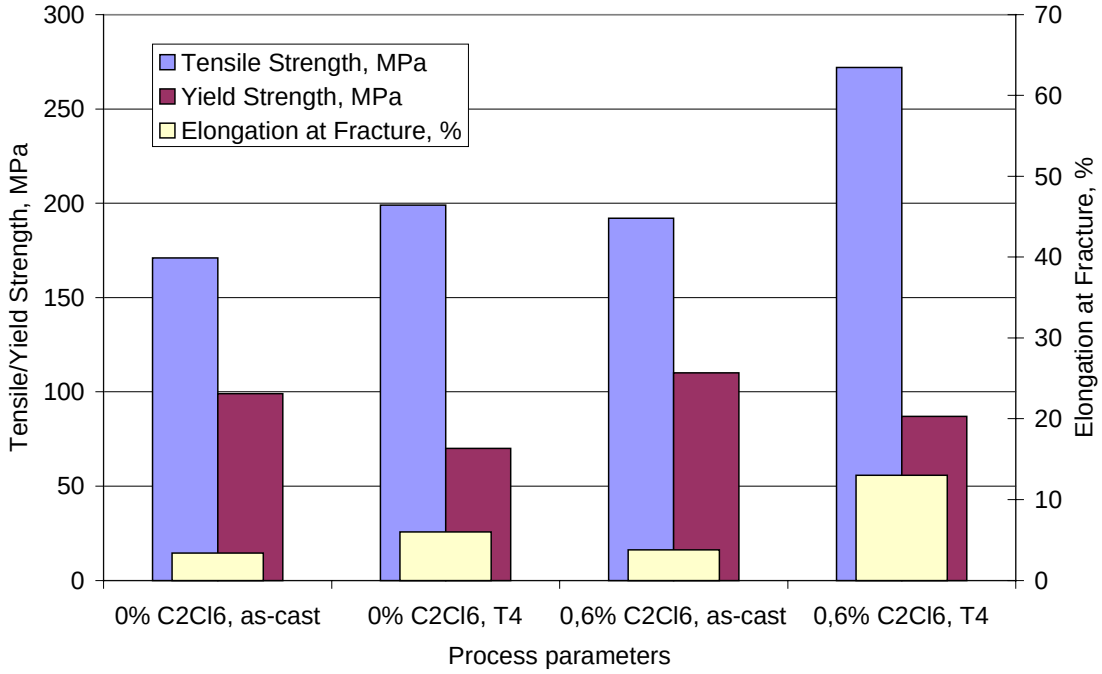

Fig. 8.32. Comparison of the mechanical properties of the 16 mm diameter grain-refined and non-grain refined samples in both as-cast and modified T4 condition.

Secondly, the modified heat treatment, when undertaken with non-grain refined samples, is ineffective in comparison to normal, non-stop solutionizing. So, 199 MPa tensile strength and 6% elongation achieved after modified solutionizing are much lower than 236 MPa and 9% after the non-stop solutionizing in the 16 mm diameter samples. A possible reason for this is the larger amount of brittle $Mg_{17}Al_{12}$ in the microstructure. In the case of the 50 mm diameter samples, modified solutionizing caused a slight improvement in all of the mechanical properties.

Grain size measurements were conducted on the 16 mm grain refined samples and the results are presented in Fig. 8.34. The mean grain size diameter was 85 μm, which is only marginally higher than the grain size of the samples in the as-cast condition (Compare with Fig. 8.14 c). These results lead us to the conclusion that grain refining is an effective tool in the suppressing of the grain growth during the solutionizing heat treatment, and, should the castings be used in the heat treated condition, grain refining melt treatment should be applied.

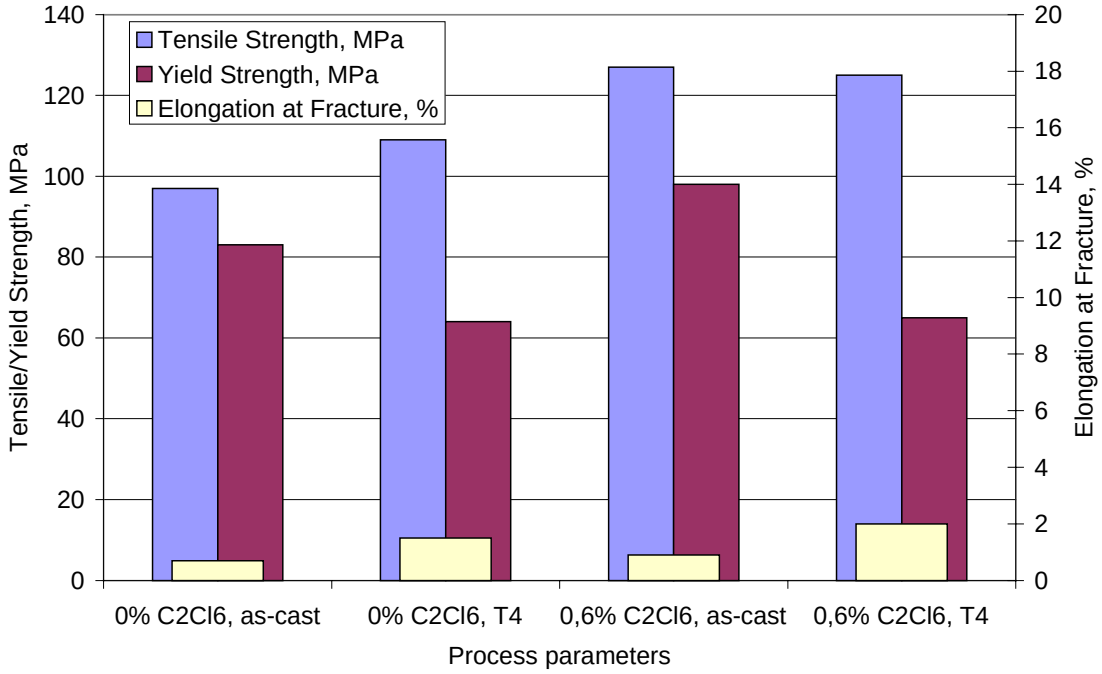

Fig. 8.33. Comparison of the mechanical properties of the 50 mm diameter grain-refined and non-grain refined samples in both as-cast and modified T4 condition.

In order to better understand the factors leading to the change in properties, fracturegraphs and TEM studies were undertaken. The TEM studies revealed that the microstructure of the solutionized samples is very homogenous, with well-developed dislocation substructure, as shown in Fig. 8.35. Dislocation looping on the Frank-Read dislocation sources and the bow-up from pinning points and clusters may be seen in this figure.

Fracturegraphs of the solutionized samples have revealed the different fracture pattern compared to the samples in the as-cast condition. The fracturegraphs of the 16 mm diameter samples are shown in Fig. 8.36-8.38. Different magnifications must be considered when observing the fracturegraphs. After 16 hours of solutionizing, the amount of plastic fracture in the samples has increased. The prolonged duration of the solutionizing causes a further increase in the transgranular fracture, and the fracture surface is marked by large amounts of twins, as shown in Fig. 8.37 and Fig. 8.38.

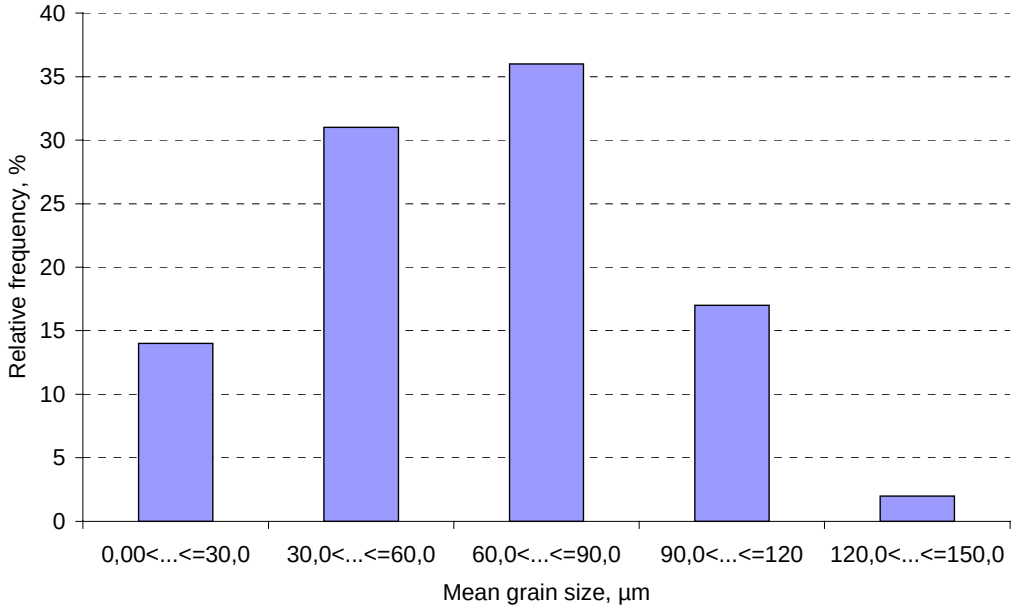

Fig. 8.34. Frequency distribution of grain size diameters of the grain refined 16 mm diameter AZ91 sand cast samples after modified solutionizing.

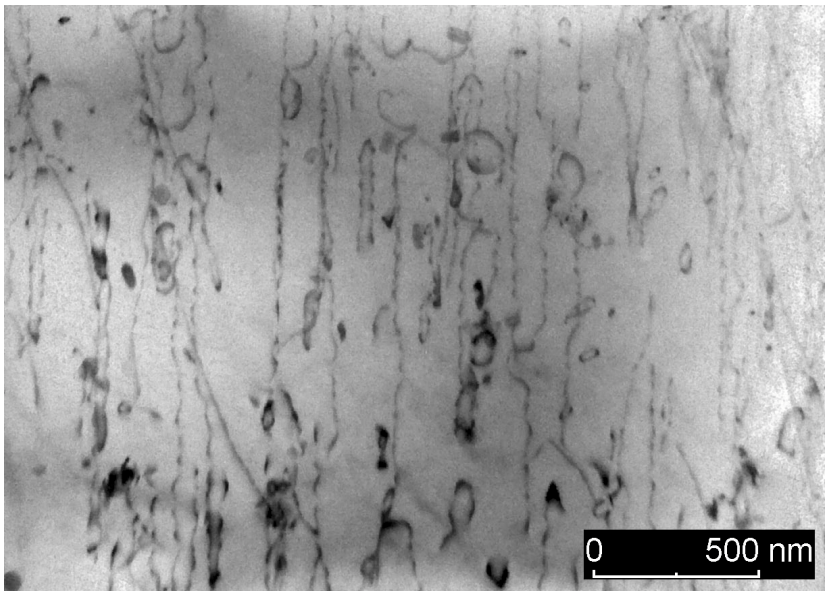

Fig. 8.35. TEM picture of the completely homogenized and quenched AZ91 sand-cast sample.

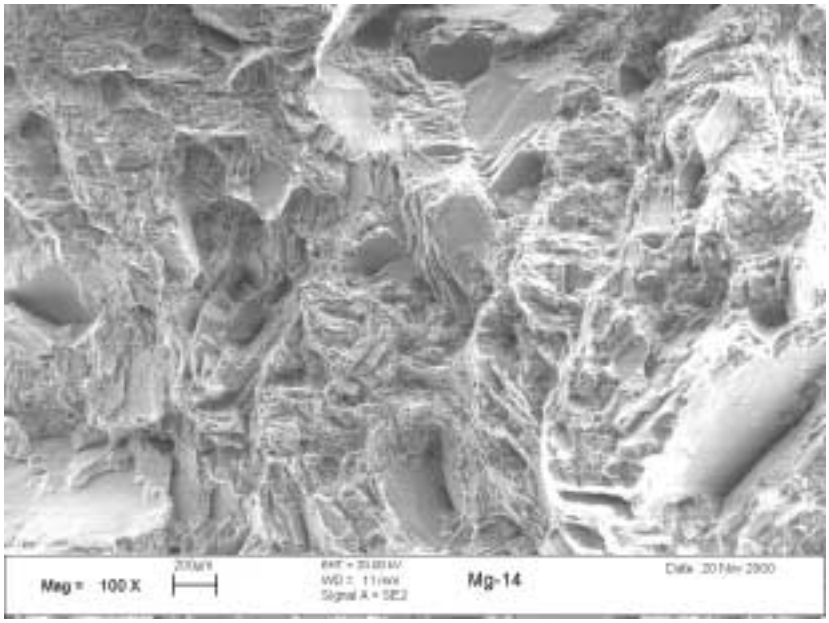

Fig. 8.36. Fracture surface of the 16 mm diameter non-grain refined sample after standard homogenizing for 16 hours.

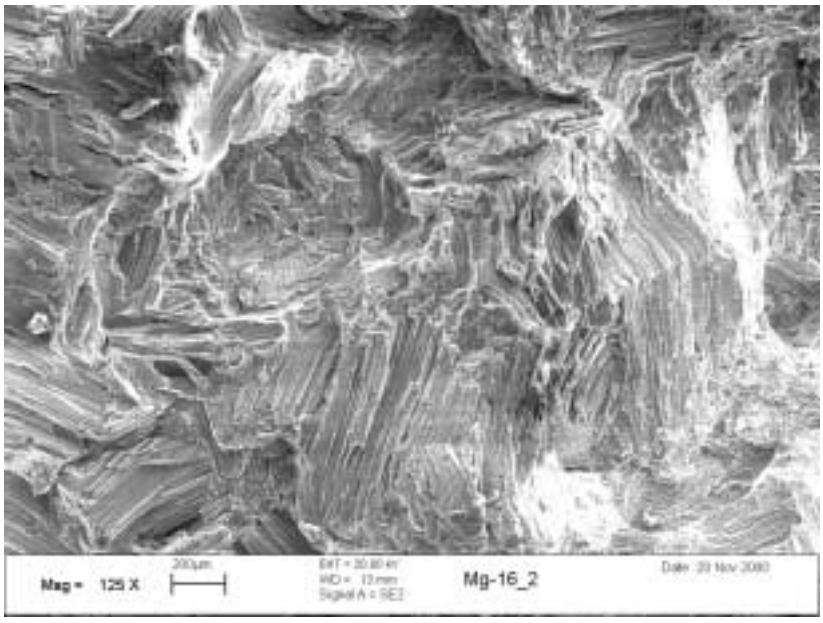

Fig. 8.37. Fracture surface of the 16 mm diameter non-grain refined sample after standard homogenizing for 32 hours.

If the homogenized and quenched samples are aged, tensile and yield strength are expected to rise, and the ductility is expected to decrease. The results of the aging of various samples are presented in the Table 8.7 and in Figures 8.39 and 8.40.

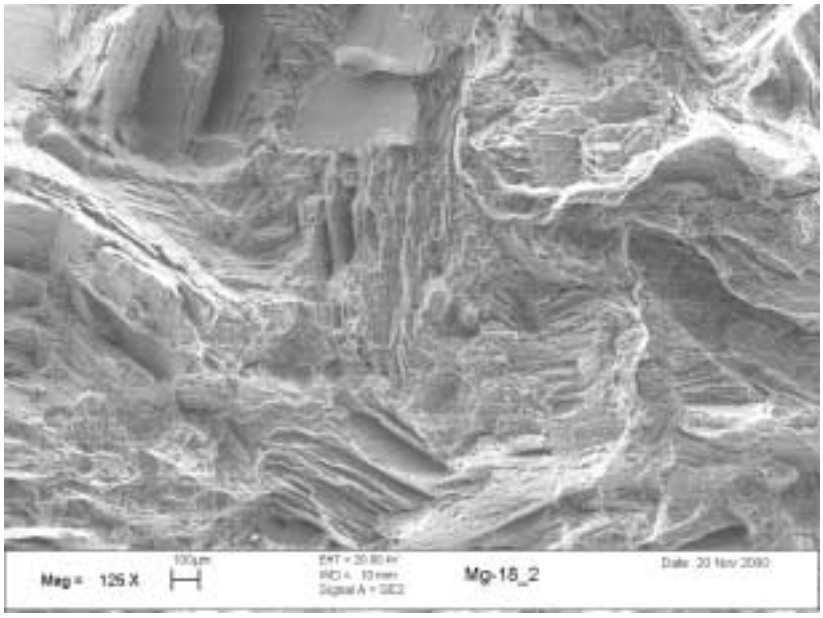

Fig. 8.38. Fracture surface of the 16 mm diameter non-grain refined sample after standard homogenizing for 48 hours.

Table 8.7. Solutionizing and annealing tests (T6)[6].

Nr.	Parameters of the heat treatment	Sample diameter, mm	Rm, MPa	$Rp_{0,2\%}$, MPa	A_5, %
1	0% C_2Cl_6, 16h@420°C, water quench, 4h @210C	50 mm	110	103	0,3
		16 mm	277	151	3,8
2	0% C_2Cl_6, 48h@420°C, water quench, 4h @210C	50 mm	133	109	0,6
		16 mm	261	146	3,7
3	0% C_2Cl_6, 48h@420°C, water quench, 8h @210C	50 mm	133	108	0,5
		16 mm	229	133	2,1
4	0% C_2Cl_6, 48h@420°C, water quench, 16h @210C	50 mm	145	117	0,5
		16 mm	215	137	1,4
5	0,6% C_2Cl_6, 16h@420°C, water quench, 4h @210C	50 mm	141	110	1,1
		16 mm	302	147	5,2

[6] Average value from at least 4 samples

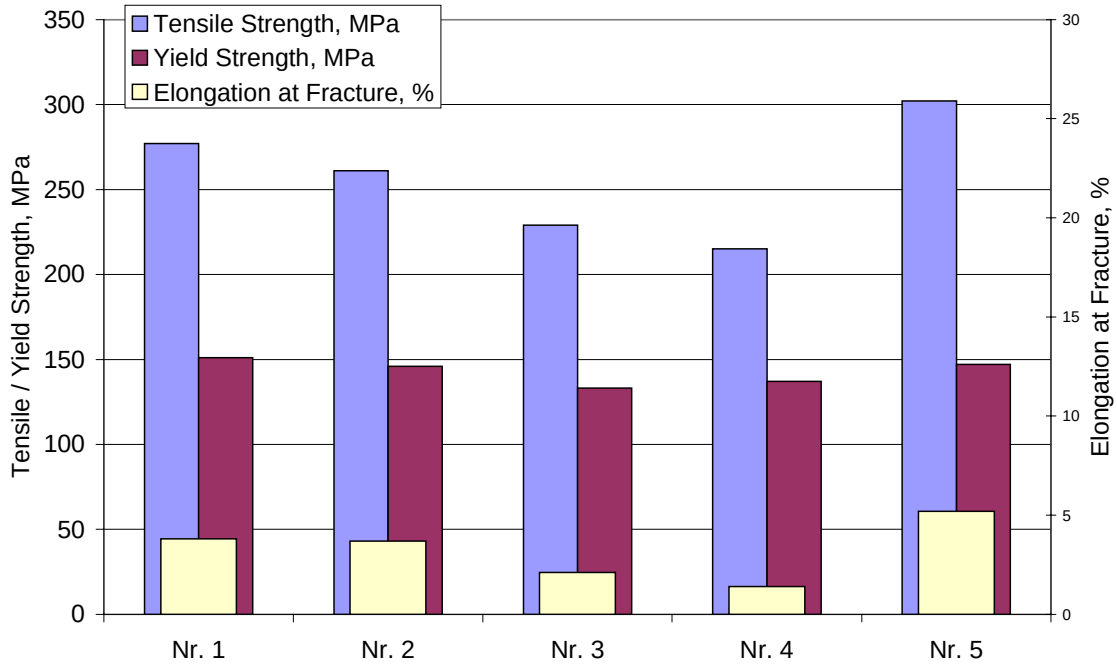

Fig. 8.39. Mechanical properties of the 16 mm diameter AZ91 sand-cast samples after T6 – heat treatment

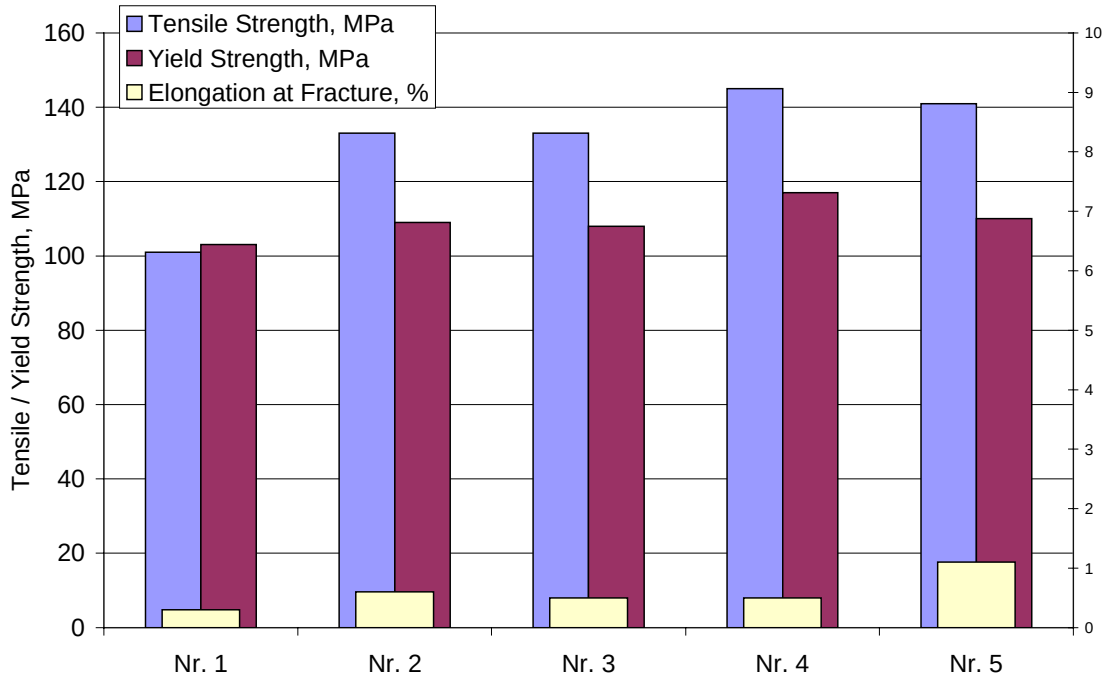

Fig. 8.40. Mechanical properties of the 50 mm diameter AZ91 sand-cast samples after T6 – heat treatment

It may be seen that the best combination of mechanical properties in 16 mm diameter samples may be achieved only in the grain-refined samples, which underwent modified heat treatment (i.e. the solutionizing was conducted with the 1 hour pause at 350°C). Tensile strength of 302 MPa, yield strength of 147 MPa and an elongation at fracture of 5,3%, achieved in the heat treated samples is much higher than 192 MPa tensile strength, 110 MPa yield strength and 3,8% elongation obtained in grain refined samples in the as-cast condition. Furthermore, it should be remembered that the non-grain refined samples in the as-cast condition had only 171 MPa tensile strength, 99 MPa yield strength and 3,4% elongation.

An important issue is a steady decrease in all mechanical properties with the exception of hardness by prolonged aging. All mechanical properties are lower in the non-grain refined samples after 16 hours of aging at 210°C than after 4 hours of aging at this temperature. One possible reason for this is the growth of precipitates in the microstructure. However, ductility and strength decrease together, which must have various reasons. This problem will be discussed later on, in the TEM investigations of the microstructure.

The 50 mm diameter samples have a different pattern in the development of the properties during aging. The observation of the behaviour of the non-grain refined samples shows that the best combination of properties will be achieved after prolonged annealing. One possible reason for this is that the strengthening of the microstructure by the precipitates compensates for the inherent microporosity. The grain-refined samples have a better combination of properties, especially a higher elongation at fracture, than the non-grain refined samples. Moreover, grain refining may allow for less aging time, thereby causing less energy consumption for the heat treatment procedure.

The hardness measurements of the microstructure can yield important information on the precipitation process in the alloy. Microhardness measures of the α-Mg solid solution were conducted in this study and their results are shown in Table 8.8.

Each reported value is the average of at least 5 measurements. We have chosen microhardness since this method is much more precise than the composite hardness of the microstructure, which can be influenced by the microporosity and by the

incompletely dissolved β-$Mg_{17}Al_{12}$ particles. The results of the microhardness measurements are presented schematically in Fig. 8.41. The largest increase in the microhardness already occurs during the first 4 hours of aging. After this time, the hardness increases only slightly. These results correspond well to those obtained by Clark [55]. Interestingly, microhardness increases insignificantly after complete homogenisation compared to the as-cast condition. One possible reason for this is the very high dislocation density present in the as-cast microstructure (Compare Figures 8.18 and 8.19)

Table 8.8. Development of Microhardness During Annealing at 210°C[7]

Conditions	As-cast	Completely homogenized	4 h at 210°C	8 h at 210°C	16 h at 210°C
Microhardness, HV	64	70	84	86	95

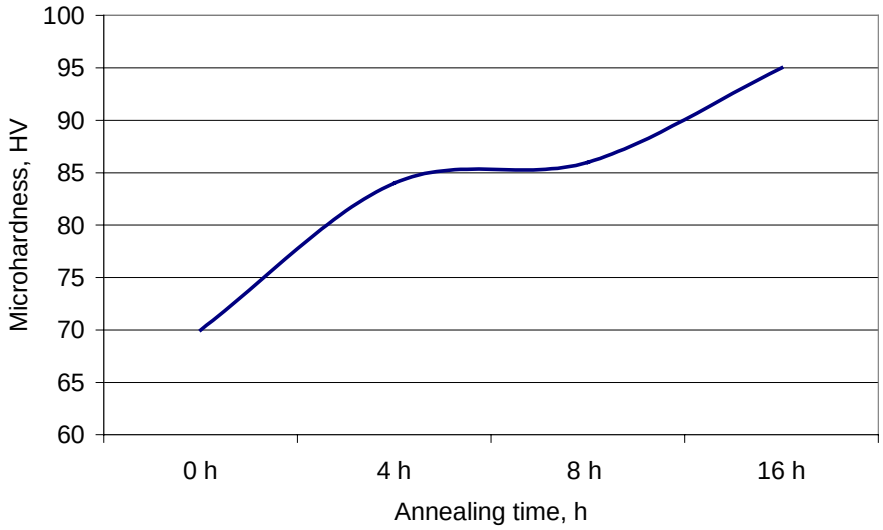

Fig. 8.41. Microhardness of α-Mg solid solution vs. annealing time at 210°C.

The microstructures of two 16 mm diameter completely homogenized (48 h at 420°C) and aged for 4 hours and 16 hours samples are shown in Fig. 8.42 - 8.45 (different magnifications should be considered).

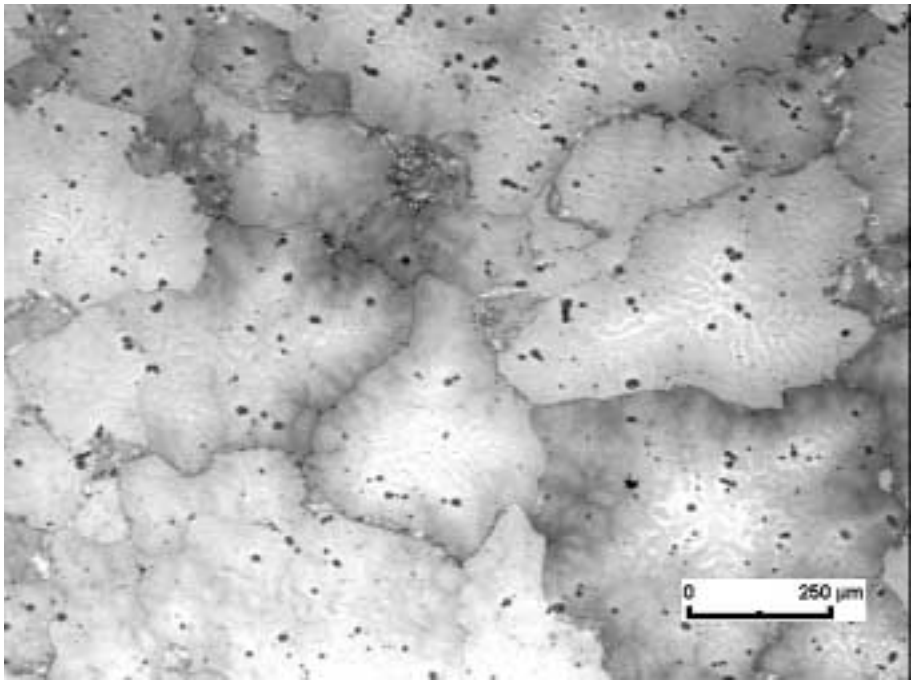

Fig. 8.42. Microstructure of 16 mm diameter samples after 4 hours of aging at 210°C.

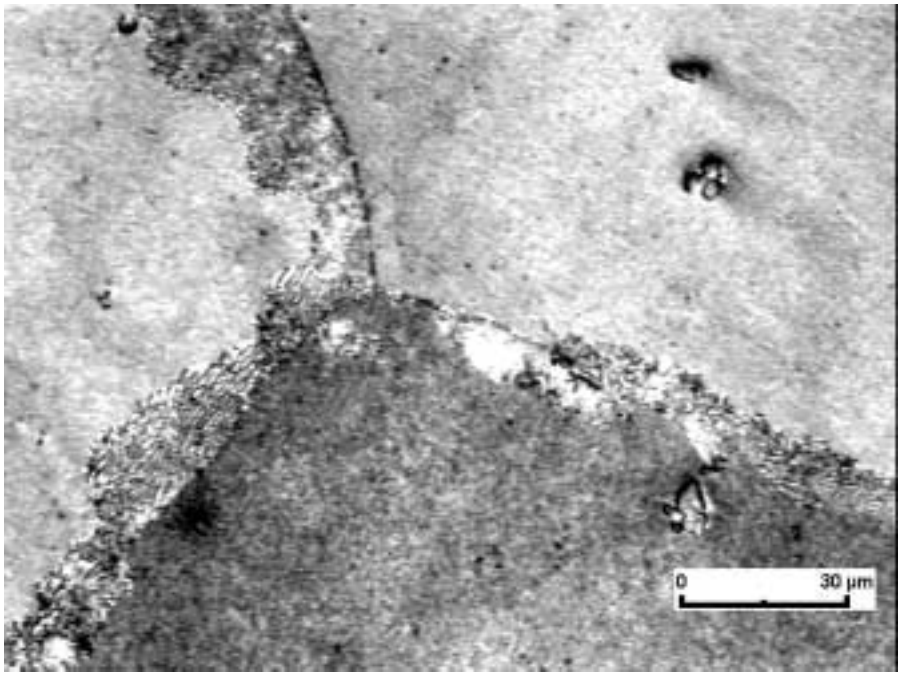

Fig. 8.43. Microstructure of 16 mm diameter samples after 4 hours of aging at 210°C (higher magnification).

[7] Mean value from at least 5 measurements

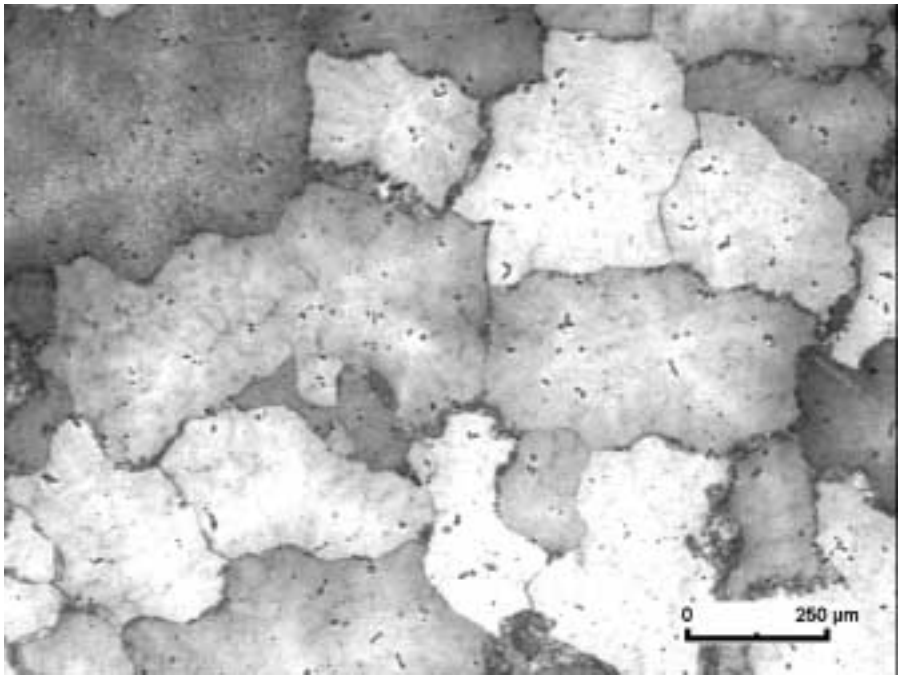

Fig. 8.44. Microstructure of 16 mm diameter samples after 16 hours of aging at 210°C.

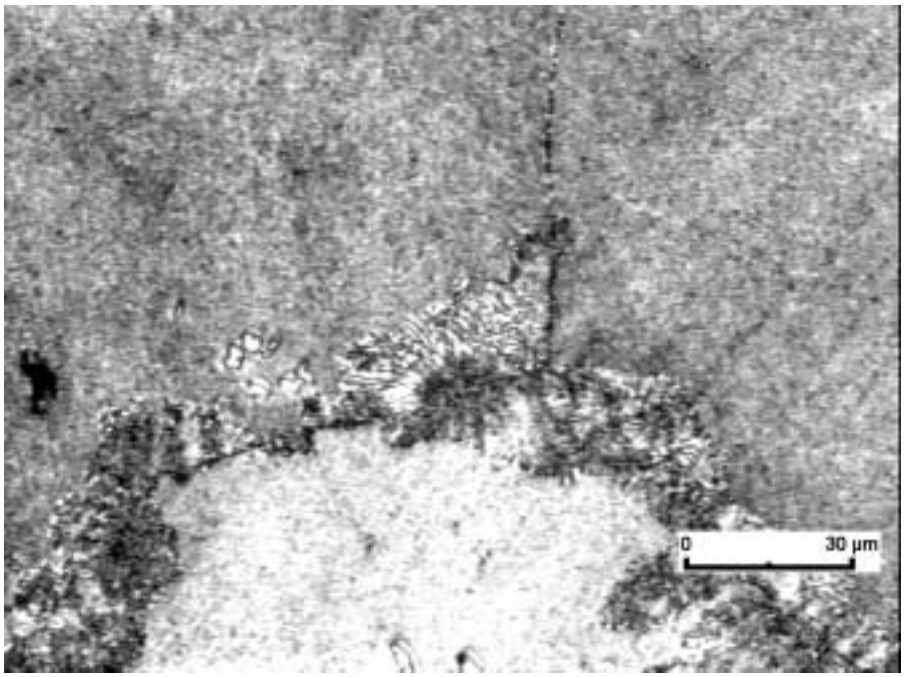

Fig. 8.45. Microstructure of 16 mm diameter samples after 16 hours of aging at 210°C (higher magnification).

The precipitation process starts at the grain boundaries, which are richer with aluminium than the core of the grain. However, light optical microscopy is not the best

suitable tool for the observation of the precipitation process, since the picture does not change significantly after longer aging times.

TEM studies have yielded a much more interesting picture of the precipitation in AZ91 magnesium alloy. Fig. 8.46-8.49 shows the TEM picture of the 16 mm diameter sample after 4, 8 and 16 hours of aging.

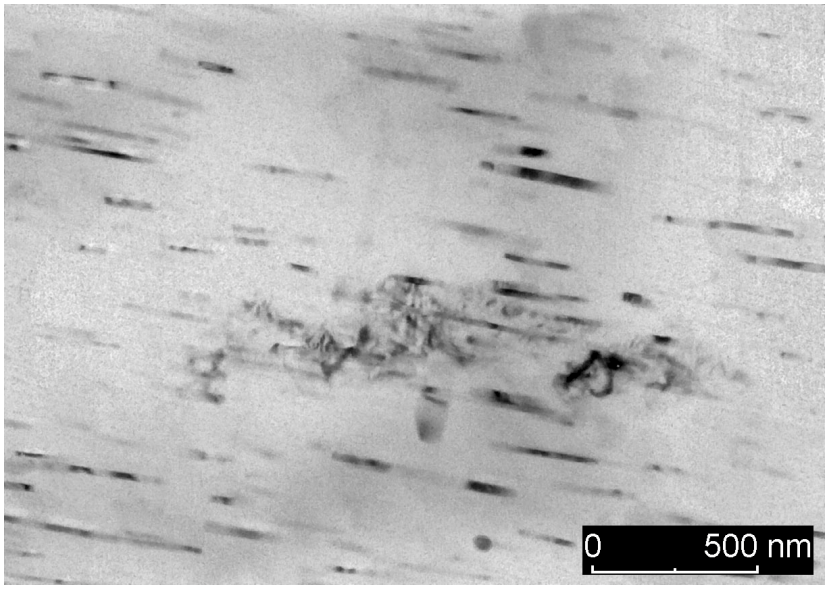

Fig. 8.46. TEM picture of 16 mm diameter samples after 4 hours of aging at 210°C

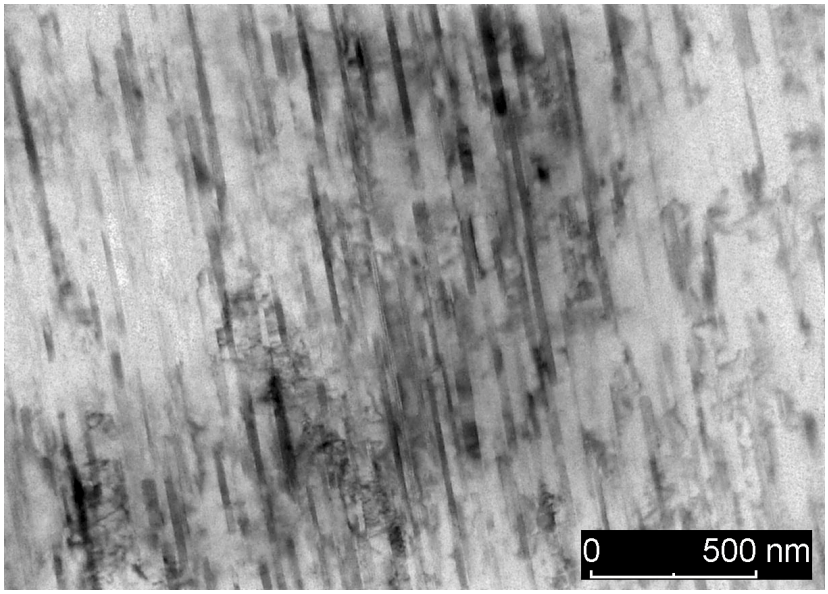

Fig. 8.47. TEM picture of 16 mm diameter samples after 8 hours of aging at 210°C

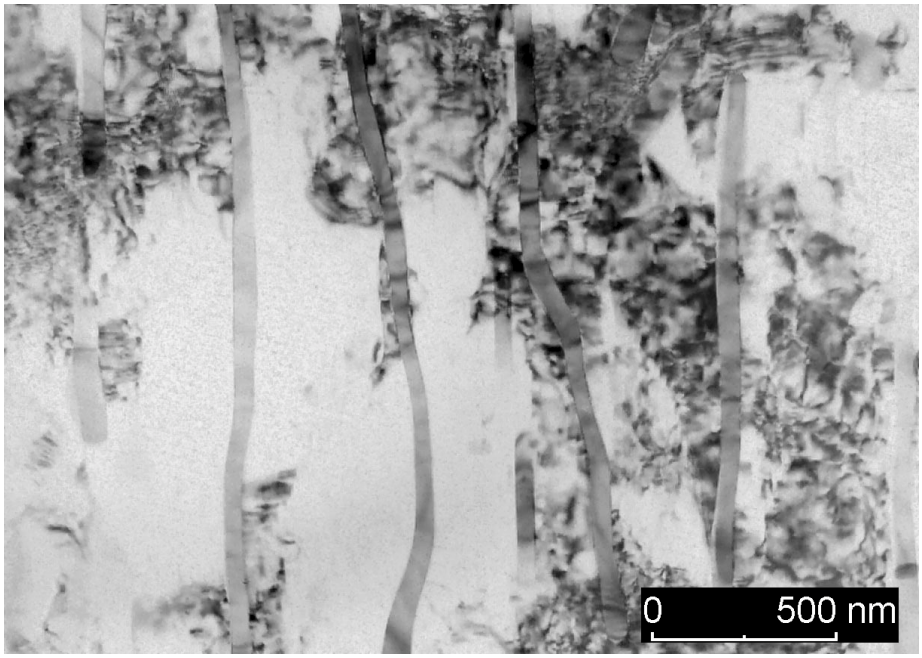

Fig. 8.48. TEM picture of 16 mm diameter samples after 8 hours of aging at 210°C

The precipitation picture changes gradually. After 4 hours of aging, only small plates of equilibrium $Mg_{17}Al_{12}$ are formed parallel to the basal plane and are elongated in the three close-packed directions of the matrix. These results correspond excellently with the results obtained by Clark [55]. The formation of these plates is responsible for the rise in the hardness of the matrix. The inter-plate spacing is about 200 nm. We have observed no dislocations around the $Mg_{17}Al_{12}$ precipitate. This is interesting, since the aging of AZ91 usually causes considerable expansion, and the dislocations should appear around the precipitates to relieve the strain.

The amount of the $Mg_{17}Al_{12}$ precipitate dramatically increased after 8 hours of aging, as seen in Fig. 8.47 and new, never before observed precipitates were found in the microstructure (Fig. 8.48, 8.49). These are several nm long, rod-form precipitates with the preferred orientation in the microstructure. The orientation relationship of these precipitates was not determined by the electron diffraction. After a prolonged aging time, these rods appear to be the main precipitate in the microstructure.

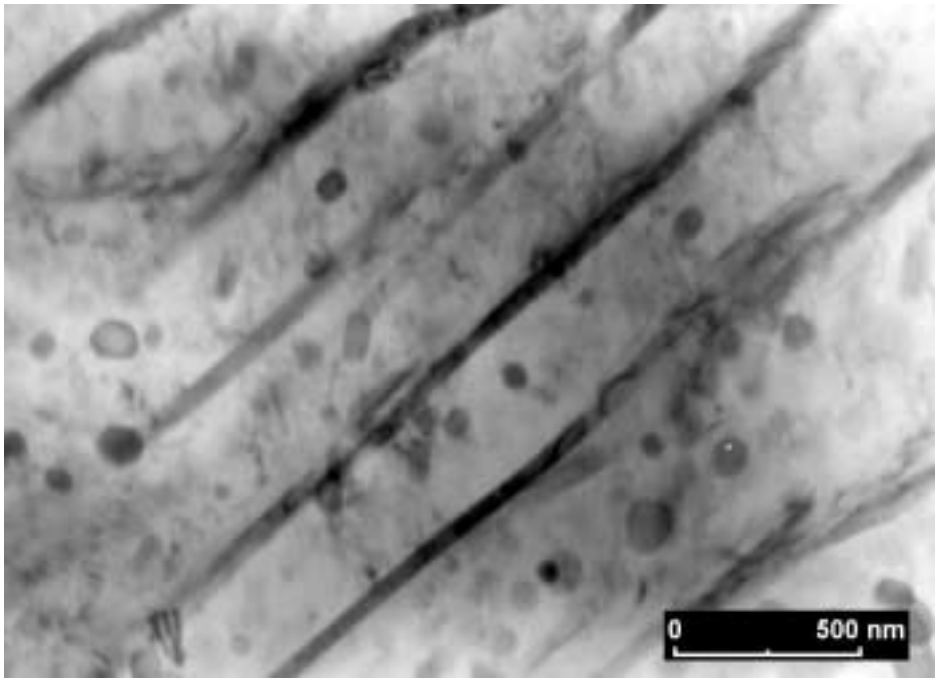

Fig. 8.49. REM picture of 16 mm diameter samples after 16 hours of aging at 210°C.

The largest increase in properties was caused by the relatively small amount of $Mg_{17}Al_{12}$ precipitate in the structure after 4 hours of aging. We suggest, however, that the real reason for the increase in strength is the availability of very small incoherent $Mg_{17}Al_{12}$ clusters. These particles are not sheared by dislocations along with the matrix.

We may suggest that the rod-like precipitates are formed from the minute $Mg_{17}Al_{12}$ precipitate, and developed by coarsening. Since these rod-like precipitates are very coarse and the spacing between them is large, they are easily sheared along with the matrix. We agree with Clark in that the role of the $Mg_{17}Al_{12}$ precipitate is to break up basal glide, cause cross slip and thus, in effect, strain harden the matrix.

The availability of coarse rod-like precipitates in the matrix changes the fracture type of the samples, as shown in Fig. 8.50-8.51.

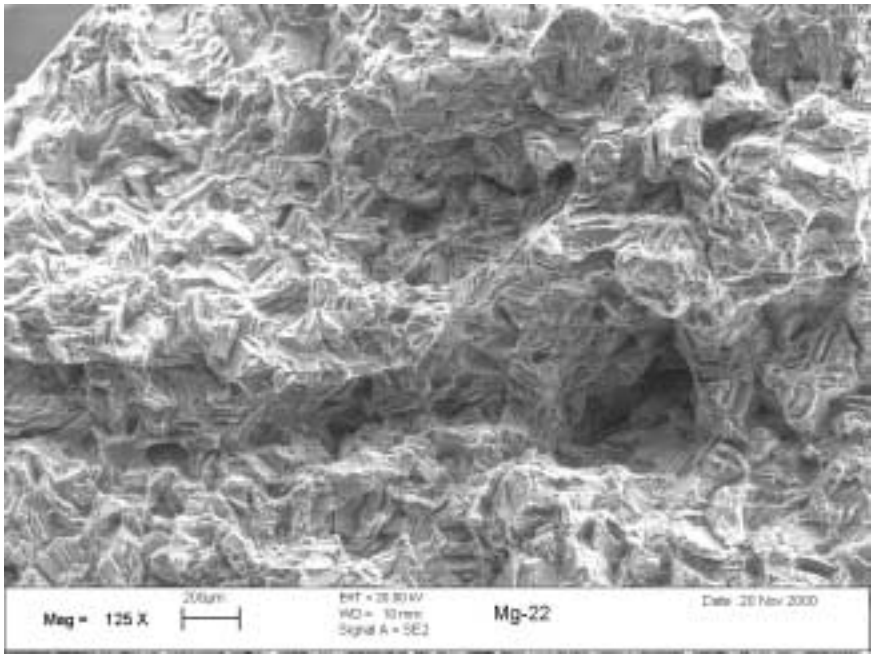

Fig. 8.50. Fracturegraph of the 16 mm diameter sample after 4 h of aging at 210°C

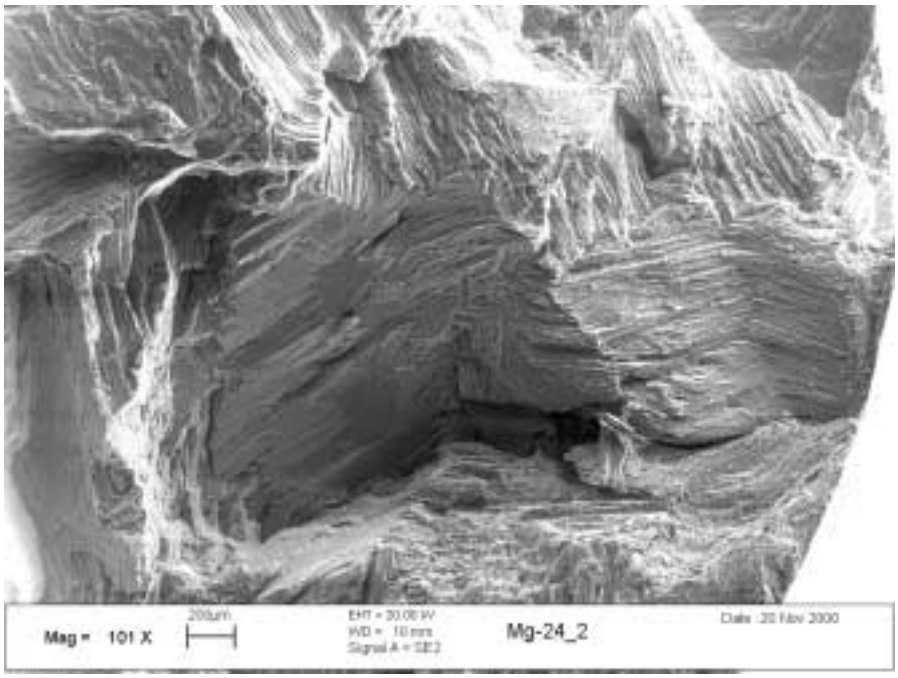

Fig. 8.51. Fracturegraph of the 16 mm diameter sample after 8 h of aging at 210°C

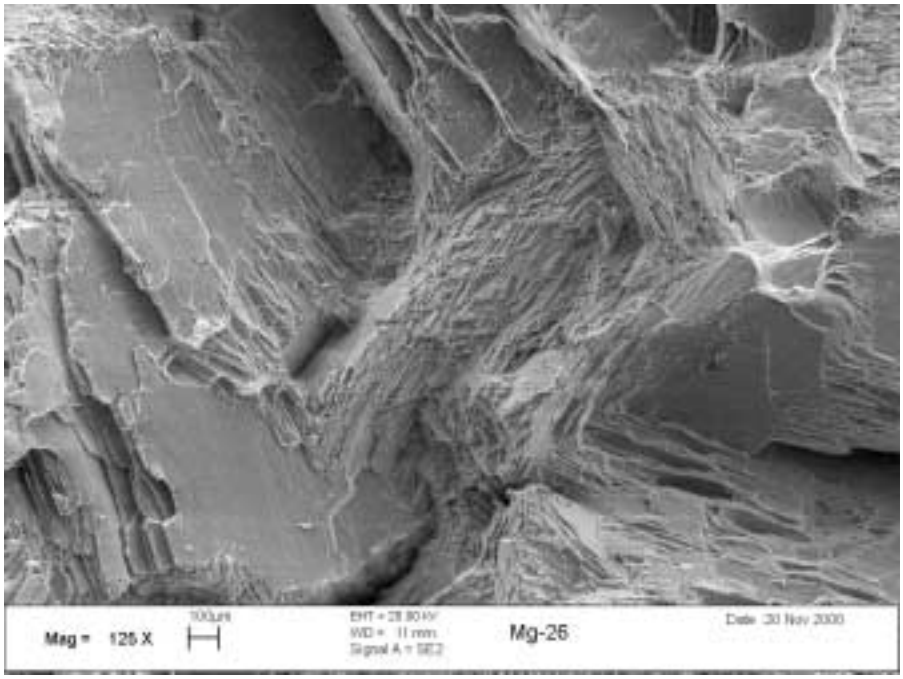

Fig. 8.52. Fracturegraph of the 16 mm diameter sample after 16 h of aging at 210°C

The fracture type in Fig. 8.50 is of the relatively uniform brittle transgranular type, with the well-developed twin structure. Longer aging times result in the transformation to the very coarse fracture of the intergranular type (Fig. 8.51, 8.52). The brittle fracture of the intergranular type may occur if the grain boundaries were embrittled by hard precipitations. As already mentioned above, the aging process in the AZ91 sand cast alloy starts in the grain boundary regions, as they are richer in aluminium than the bulk matrix. After the short aging time, precipitates at the grain boundaries did not grow and coarse to the extent that they could significantly diminish ductility. The crack propagates on the path with the lowest fracture energy. The grain boundaries still strengthen the matrix by acting as barriers to the movement of dislocations. With prolonged aging, precipitates coarse and create very brittle regions in the microstructure. The dislocations avoid the particles by climbing or cross-slipping around it.

In sum, heat treatment is a useful tool for the sand caster of magnesium alloys. “Tailored” heat treatment procedures may be used to improve the properties of AZ91 sand cast parts. A lot of magnesium alloy applications today need a relatively high ductility. The solution to this problem is the homogenization heat treatment followed by quenching in water. The best mechanical properties may be obtained in the grain-

refined parts, which have undergone germination-prohibiting heat treatment. The elongation at fracture values as high as 13% combined with tensile strength of 272 MPa were obtained in this study. These values are well comparable to the results obtained in the high-pressure die-castings.

The homogenization and quenching heat treatment, however, usually decreases yield strength. To solve this problem, the T6 heat treatment is usually applied. During the aging, $Mg_{17}Al_{12}$ precipitates from the super-saturated solid solution, resulting in significant hardening. The duration of aging should be chosen according to the wall thickness of the parts to be heat-treated. Thicker parts require longer aging times, while in the relatively thin castings excellent mechanical properties are achieved already after 4 hours of aging. Again, grain refining may significantly boost the properties.

In this study, new rod-like precipitates were found. We suppose that these precipitates originate from small plates of equilibrium $Mg_{17}Al_{12}$ and coarsen during the aging.

8.4. Results of the Instrumented Impact Tests

In this study, instrumented impact testing of samples machined from the 20 mm and 40 mm thick plates of sand cast AZ91 were conducted. Results of the instrumented impact tests are presented in Table 8.9 and in the Fig. 8.53. Representative impact curves are shown in Fig. 8.54-8.56.

Table 8.9. Results of the impact tests[8]

Nr.	Parameters of the samples	Wall Thickness, mm	W, J	Max F, N
1	0% C_2Cl_6, F	40	1,12	2166
		20	1,06	2306
2	0,6% C_2Cl_6, F	40	1,4	2296
		20	1,03	2301
3	0% C_2Cl_6, Homogenized and quenched	40	3,1	3300
		20	3,08	2766
4	0,6% C_2Cl_6, Homogenized and quenched	40	3,5	3100
		20	3,44	2937
5	0% C_2Cl_6, Quenched and aged	40	1,03	2007
		20	1,06	2498
6	0,6% C_2Cl_6, Quenched and aged	40	1,6	2329
		20	1,1	2123

Wall thickness does not influence the impact properties to the same extent that it does in tensile tests. Moreover, impact energy is almost the same for the samples in the as-cast condition as for the samples in quenched and aged condition. Only the homogenization heat treatment causes a significant increase in the impact energy, tripling impact energy values. Therefore, for energy-absorbing parts, the castings in T4-heat treatment condition should be applied.

A closer look at the results of the impact tests reveals that the samples machined from the thick-walled castings have slightly higher values of impact energy. We may suggest that the “thick-walled” samples in the as-cast condition are stronger under impact

conditions, as the crack probably propagates along the grain boundaries, where the $Mg_{17}Al_{12}$ phase is present in higher amounts than in the "thin-walled" samples because of the lower solidification rate. However, we cannot give any explanation for this effect in the quenched and aged samples.

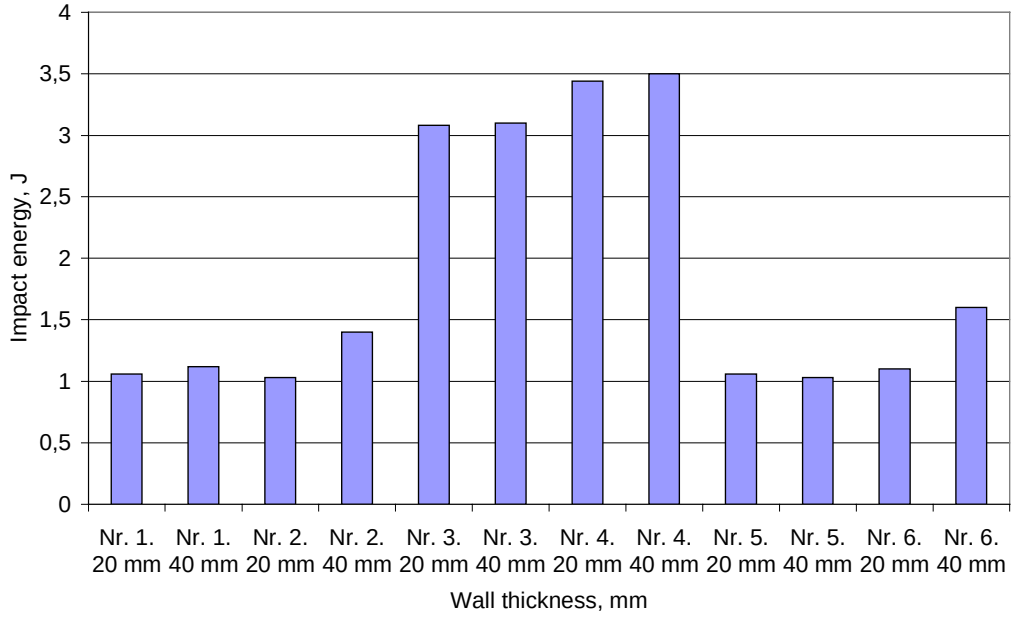

Fig. 8.53. Impact energy vs. process parameters

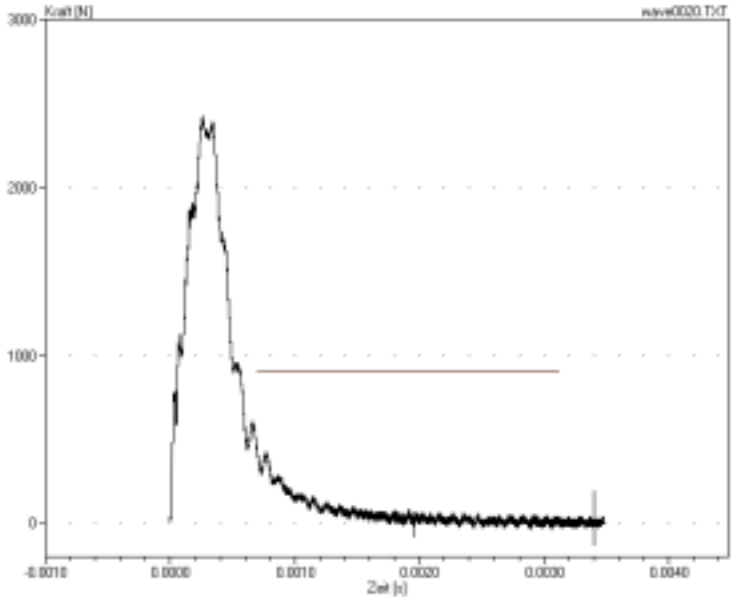

Fig. 8.54. Instrumented impact curve of the sample machined from the 20 mm thick plate, grain-refined, as-cast condition.

[8] Average value from at least four measurements

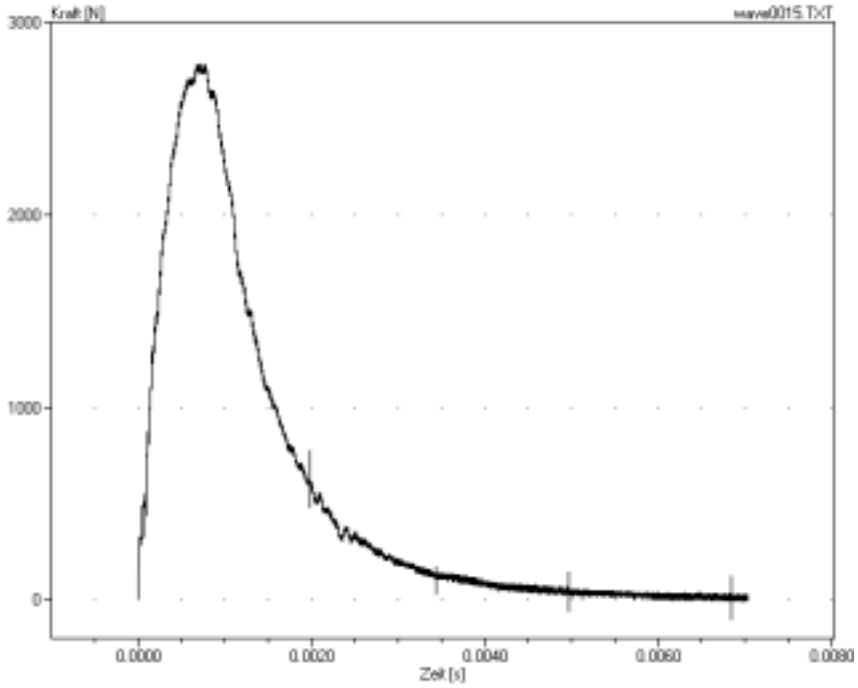

Fig. 8.55. Instrumented impact curve of the sample machined from the 20 mm thick plate, grain-refined, homogenized and quenched (T4) condition.

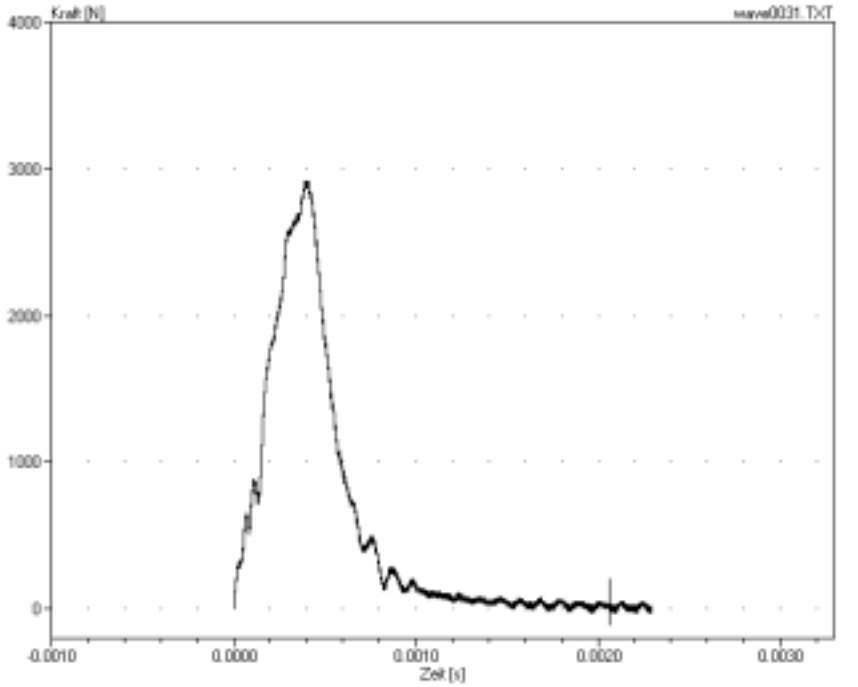

Fig. 8.56. Instrumented impact curve of the sample machined from the 20 mm thick plate, grain-refined, quenched and aged (T6) condition.

The fracturegraphs of the samples machined from the 20 mm thick plates are presented in Fig. 8.57-8.59.

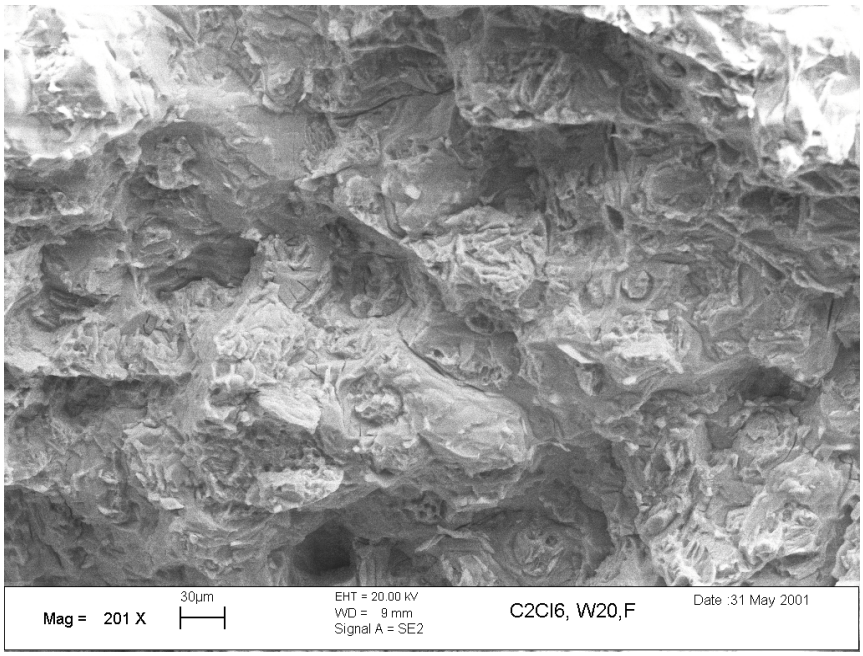

Fig. 8.57. Fracturegraph of the grain-refined sample machined from the 20 mm thick plate, as-cast condition.

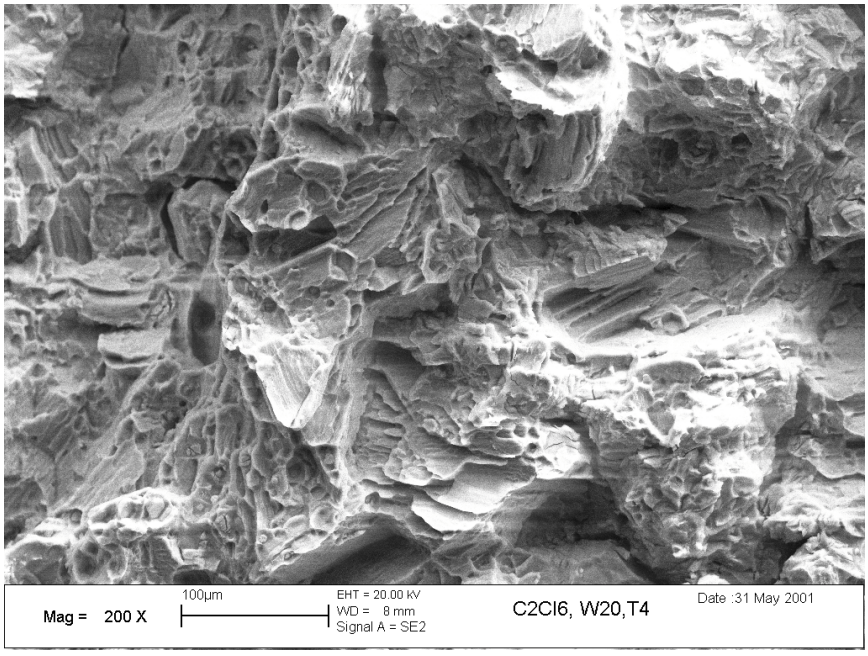

Fig. 8.58. Fracturegraph of the grain-refined sample machined from the 20 mm thick plate, T4 condition.

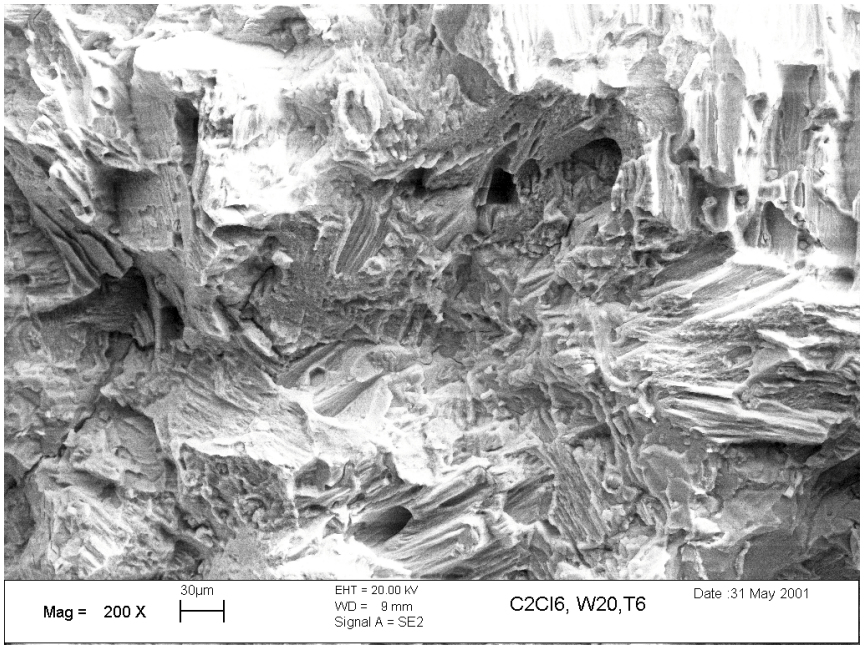

Fig. 8.59. Fracturegraph of the grain-refined sample machined from the 20 mm thick plate, T6 condition.

The comparison of these fracturegraphs with those obtained after standard tensile test (Fig. 8.20, 8.36 and 8.50) shows the drastic change of the fracture type. The fractures of all impact test samples are much coarser than those of the tensile test samples. This is caused by high impact velocity, which prohibits significant plastic deformation. The amount of ductile fracture decreased in all impact samples.

The general feature of all impact fracture samples is the very coarse intergranular fracture. However, the heat treatment also changed the fracture morphology. So, the amount of ductile fracture is somewhat higher in the homogenized and quenched sample in comparison to the as-cast sample. The fracturegraph of the T6 - heat treated sample demonstrates strong orientation morphology which may be caused by twinning.

In sum, sand-cast magnesium alloy AZ91 has poor impact properties. The results of this study may suggest that parts cast from AZ91 should not be used as crash structures in automobiles. If, however, designers demand AZ91 parts, homogenization treatment should be applied.

8.5. Results of the Neutron Diffraction Experiments

The recalculated pole figures of the non-deformed non-grain-refined and grain-refined samples in the as-cast condition are presented in Fig. 8.60 a and 8.60 b.

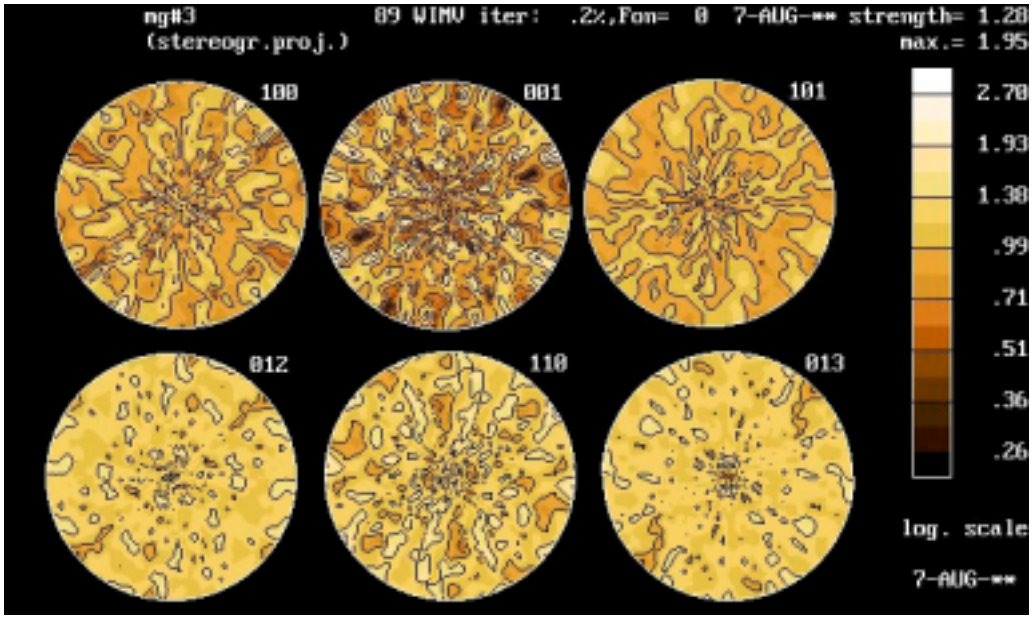

Fig. 8.60 a. Recalculated pole figures of the non-deformed, non-grain-refined AZ91 sample in the as-cast condition.

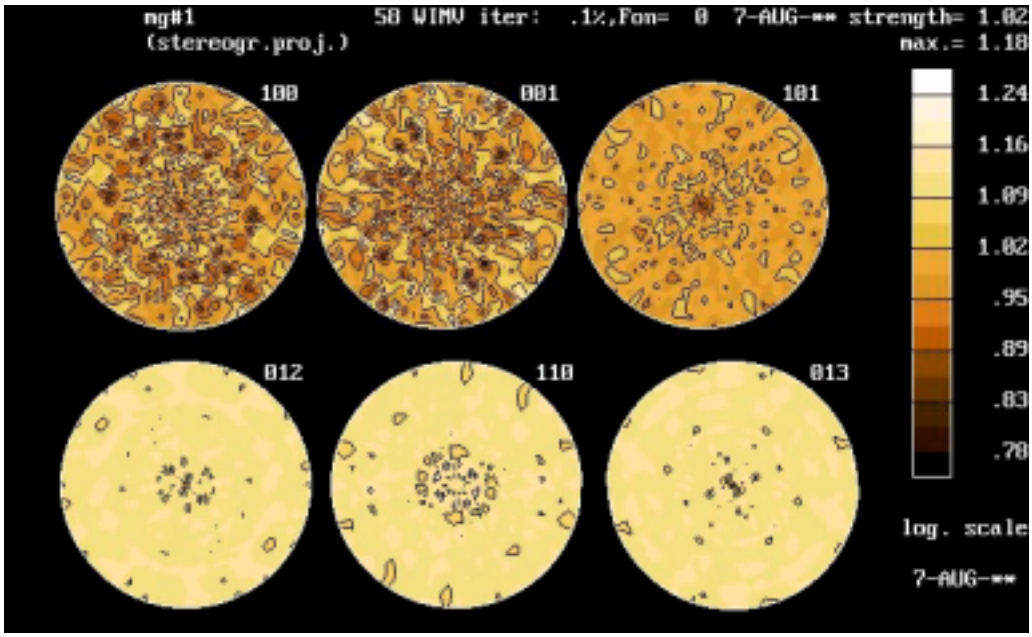

Fig. 8.60 b. Recalculated pole figures of the non-deformed, grain-refined AZ91 sample in the as-cast condition.

In Figures 8.60a and 8.60b, a very slightly developed rotational symmetric solidification fiber texture (100) may be seen, which is more intense in the grain refined sample because of the smaller grain size, and thus, greater amounts of crystallites with similar orientation. Solid solution heat treatment causes a more pronounced development of the (100) fiber texture in the grain refined sample (Fig. 8.61). A possible explanation for this phenomenon is the grain growth, combined with the relaxation of thermal stresses occuring during the solution heat treatment.

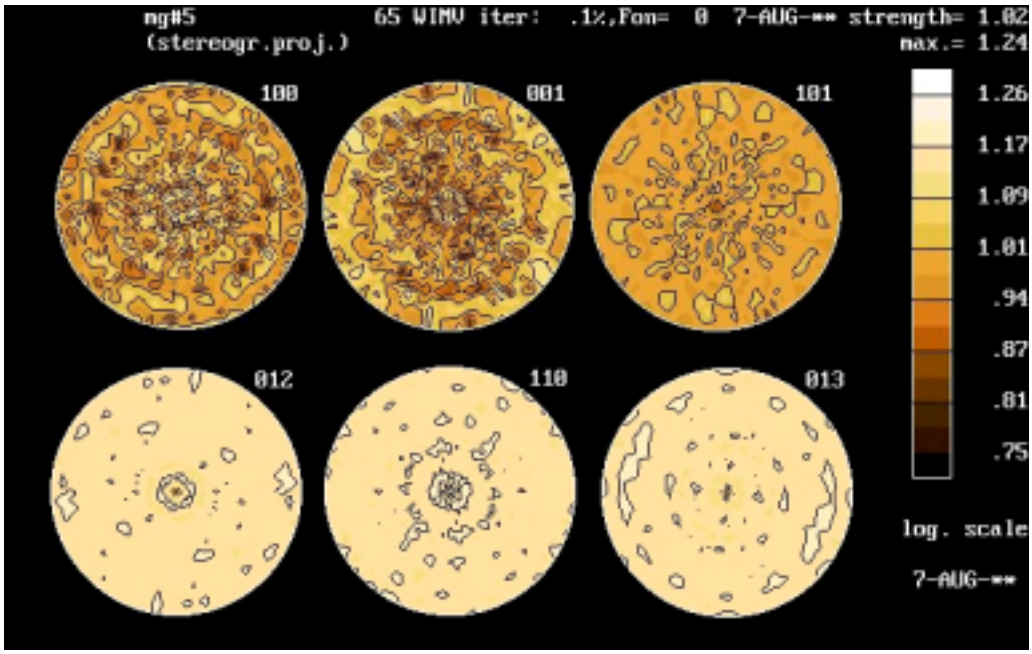

Fig. 8.61. Recalculated pole figures of the non-deformed, grain-refined AZ91 sample in the T4-condition.

Textures of the non-deformed samples in the T6 condition, both grain-refined and non-grain refined, only differ slightly from those of the samples in the T4 condition.

On the contrary, all deformed (both grain-refined and non-grain-refined) samples had a clear (100) fiber texture component. The highest intensity of the (100) fiber texture component was found in the grain-refined, T4-heat treated sample (Fig. 8.62 a). The non-grain-refined, T4-heat treated sample also has a high intensity of the (100) fiber texture component, but larger grain size causes less grains to be similarly oriented after the deformation (Fig. 8.62 b).

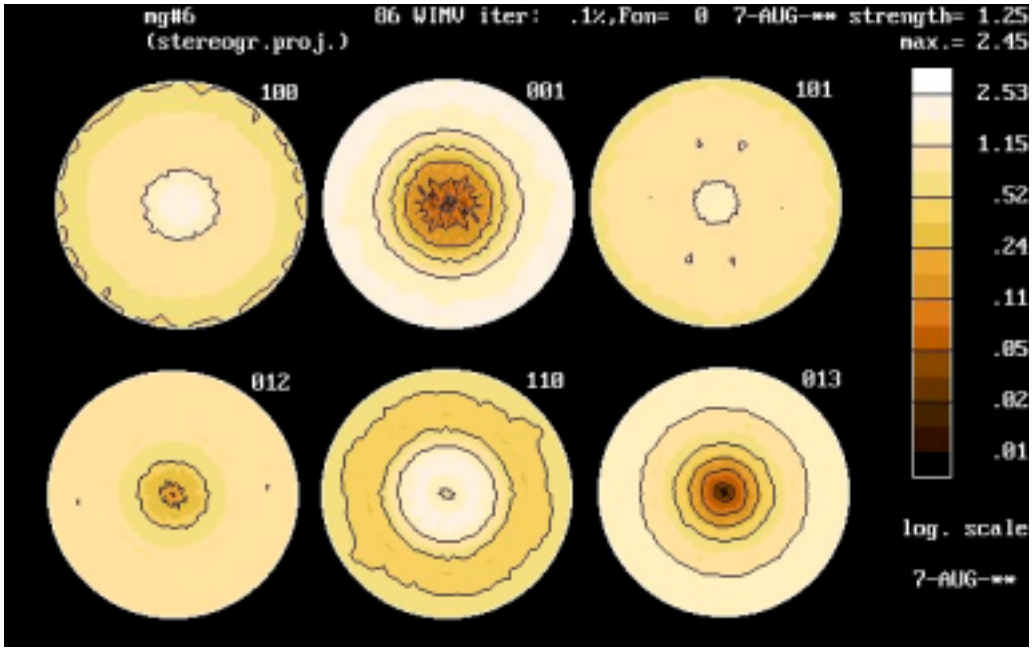

Fig. 8.62 a. Recalculated pole figures of the deformed, grain-refined AZ91 sample in the T4-condition.

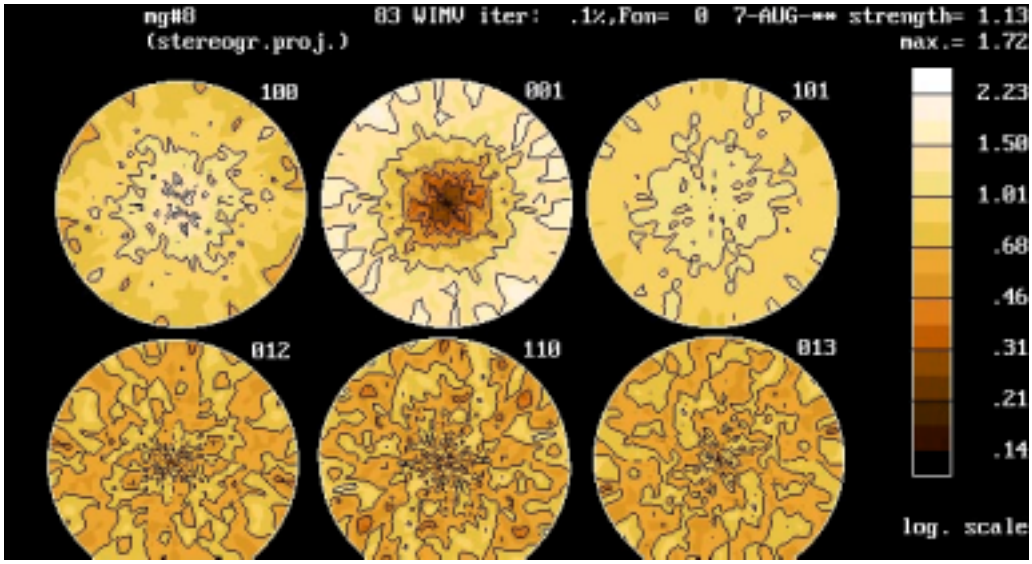

Fig. 8.62 b. Recalculated pole figures of the deformed, non-grain-refined AZ91 sample in the T4-condition.

The deformed grain-refined T6-heat treated samples also have a preferred (100) texture, which was found (similar to samples in the as-cast condition) to be very unsharp in the deformed, non-grain-refined, T6-treated samples. (Compare Figures 8.63 a and 8.63 b).

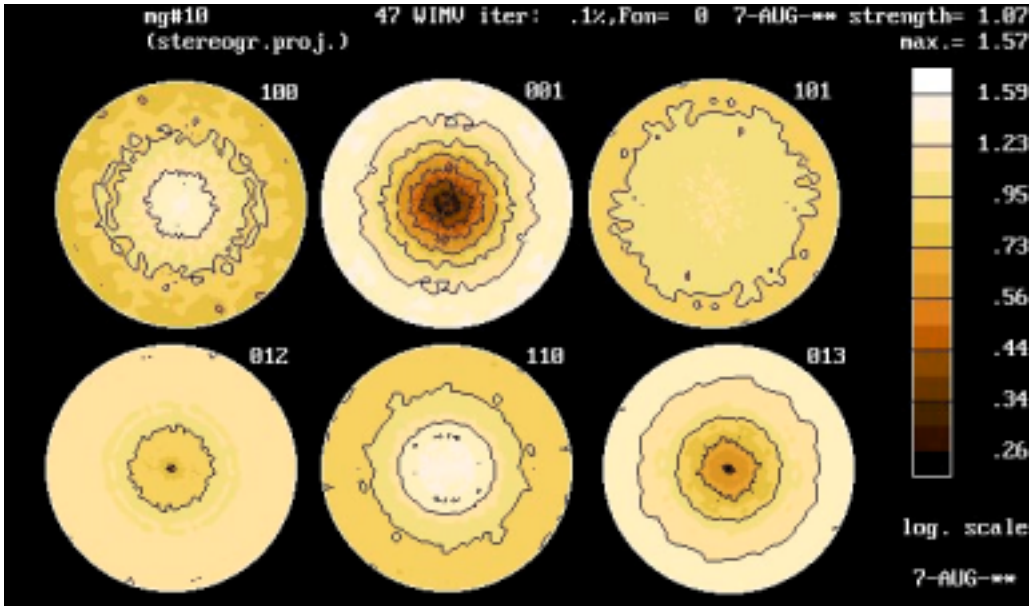

Fig. 8.63 a. Recalculated pole figures of the deformed, grain-refined AZ91 sample in the T6-condition.

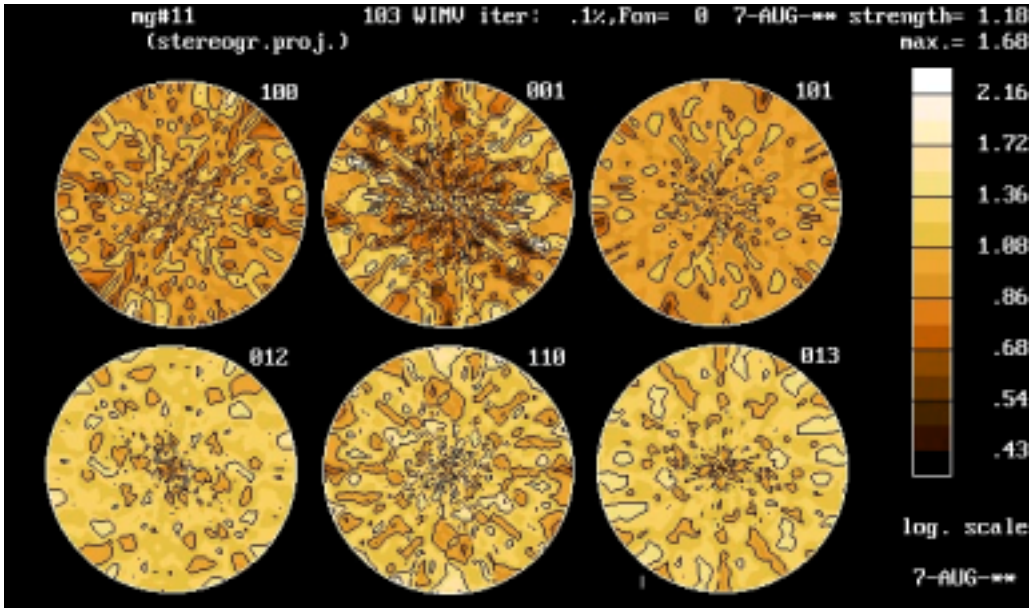

Fig. 8.63 b. Recalculated pole figures of the deformed, non-grain-refined AZ91 sample in the T6-condition.

As the deformation increases from the as-cast condition through the T6 to the T4 condition, more and more crystals change their spatial orientation and sharper textures develop (Compare Figures 8.64 a and 8.64 b).

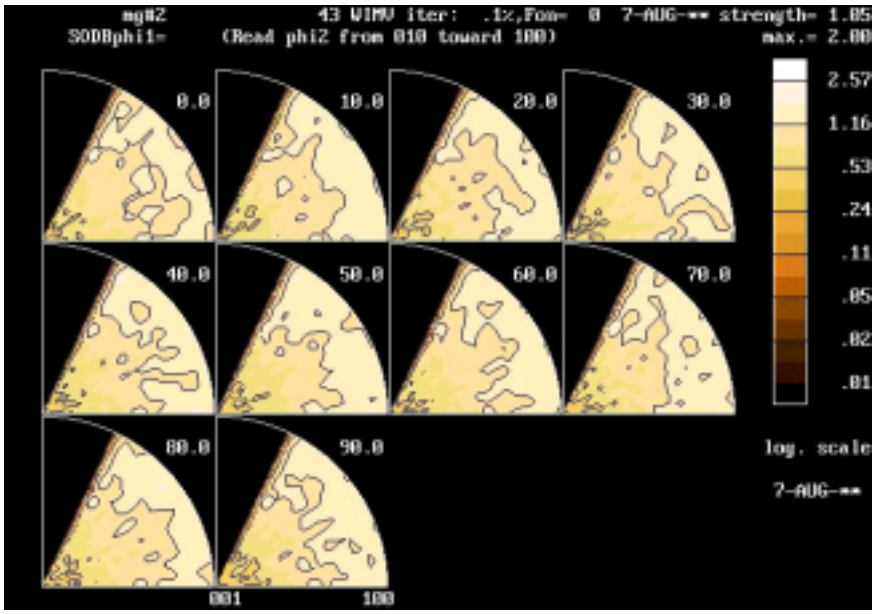

Fig. 8.64a. ODF of the deformed, grain-refined AZ91 sample in the as-cast condition.

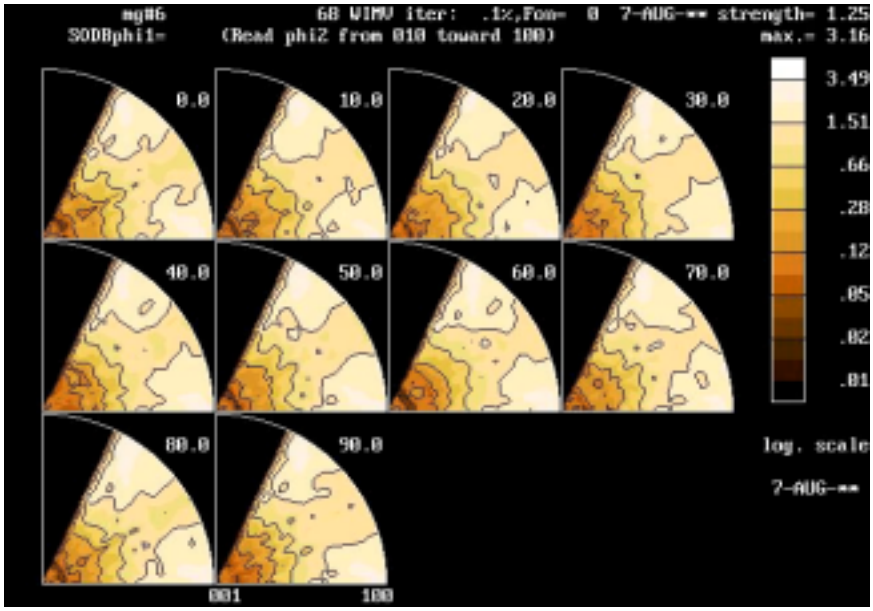

Fig. 8.64b. ODF of the deformed, grain-refined AZ91 sample in the T4 condition.

In sum, it can be stated that as-cast textures do not influence the mechanical properties of AZ91. Knowledge of the texture development in various conditions may provide designers with a useful tool for the prediction of the mechanical behaviour of magnesium alloy parts under different stress conditions.

8.6. Results of the Stress Relaxation and Damping Tests

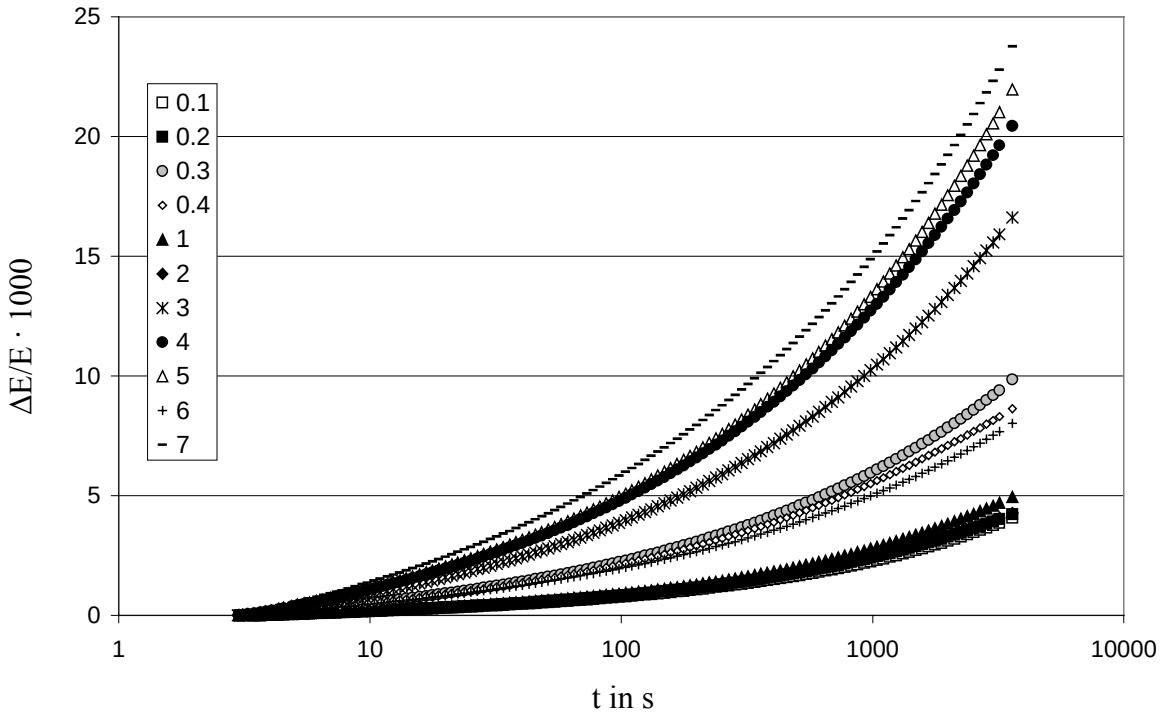

Fig. 8.65. Change of relative modulus ΔE/E versus time for various samples.

Stress relaxation curves for all samples tested are presented in Fig. 8.65. Three zones can be distinguished. All T6 - heat treated samples have the highest modulus defect at 3030s in comparison to the other samples. The grain refined and T6 - heat-treated sample #7 has the most pronounced modulus defect of them all. The second group of samples has a lower modulus defect. These are the grain-refined, as-cast sample #0.3, the gravity die-cast sample #0.4 and the grain-refined, T4-heat treated sample #6. The third group of samples possess the lowest modulus defect and include samples #0.1, #0.2, #1 and #2. Interestingly, these are the non-grain-refined samples, either in the as-cast condition, or in the T4-heat treated condition.

It may be concluded that the non-grain refined samples, both in the as-cast or in the T4-heat treated condition have the best long time stability, which is of interest not only for precision mechanical instruments but also for mass-production parts, where low stress relaxation is desirable, if the magnesium part is to be joined to other structural components by means of bolting.

Low stress relaxation in as-cast and T4- solution heat-treated samples may be caused by the microstructural features. The non-grain refined samples have a larger grain size in comparison to the grain-refined samples. However, further investigations are needed to explain this phenomenon. The as-cast microstructure of the magnesium alloy AZ91 also has large inclusions of very hard intermetallic phase β-$Mg_{17}Al_{12}$, which are very stable at room temperature. The solution heat treatment T4 greatly increases the ductility and hardness of α-magnesium matrix by solving almost all β-$Mg_{17}Al_{12}$.

It may be suggested that after the solution and aging heat treatment T6, stress relaxation increases because of precipitation of intermetallic β-$Mg_{17}Al_{12}$ from the supersaturated solid solution of α-magnesium. This has also been reported from other investigations [70, 76]. However, further research is needed to explain this phenomenon.

The lowest stress relaxation was reached in samples with relatively low mechanical properties.

Fig. 8.66 shows the variation of δ with the maximum strain amplitude ε for samples manufactured with AZ91. From the first glance, the difference in the damping behaviour of the as cast and the heat-treated samples are evident. For small strains, the logarithmic decrement is virtually equal for as-cast (both 16 mm, 50 mm and die-cast sample), T4-heat treated samples and T6-treated sample #3. The T6-heat treated samples #4 and 5 have somewhat higher values of logarithmic decrement at small strains. However, at larger strains, the logarithmic decrement of almost all samples increases, with a rapid onset in the as-cast specimen. Only two grain-refined and heat treated samples #6 and #7 do not show any significant increase in damping.

This increase in damping with strain amplitude may be explained by the model of Granato and Lücke. As the as-cast microstructure has fewer weak pinning points for the dislocations than the homogenized and annealed sample, which is saturated with aluminium atoms and incoherent $Mg_{17}Al_{12}$-precipitates, the dislocations break away easier from weakly pinned sites in the as-cast samples than they do in the heat-treated samples, thus causing a drastic increase in damping. The earlier onset of a damping increase in the 16 mm specimen in comparison to the 50 mm specimen may be caused by differences in the microstructure of the samples, with more lamellar eutectoid ß-

phase precipitates in the 50 mm specimen. The gravity die-cast sample #0.4 and the grain-refined sample #0.3 both have a finer grain size than the non-refined samples #0.1 and #0.2. Grain boundaries may serve as strong pinners and thus prohibit the break away of dislocations.

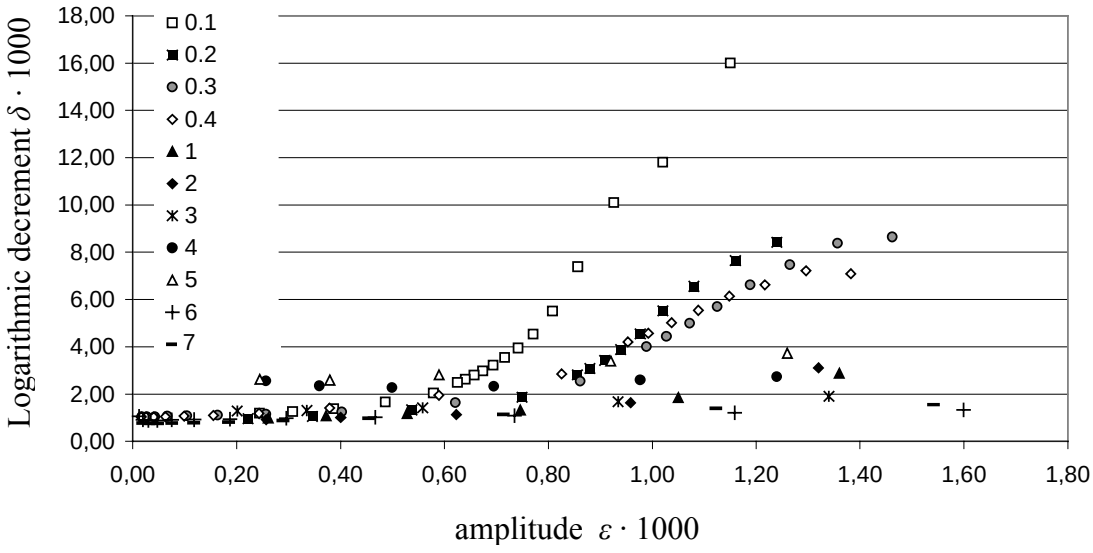

Fig. 8.66. The logarithmic decrement δ vs. maximum strain amplitude ε

A closer look at the different damping behaviour of heat-treated samples is given in Fig. 8.67. The completely homogenized and annealed samples # 4 and #5 have a higher damping compared to the partially homogenized sample #3 and homogenized and annealed samples #1 and #2 already at very low strains ε. At higher strains, the completely homogenized and annealed for 16 h sample #5 has a higher damping than the completely homogenized and annealed for 4 h sample #4. Longer annealing times allow for higher amounts of incoherent ß-$Mg_{17}Al_{12}$ precipitates in the microstructure, which in turn causes higher logarithmic decrement values. The microhardness of the magnesium solid solution shows a direct correlation between hardness values and logarithmic decrements (Table 8.8).

In the case of homogenized and quenched samples, a steeper increase of the logarithmic decrement of partially homogenized sample #1 compared to the completely homogenized sample #2 may be explained by the onset of grain growth or germination at prolonged homogenization times as the damping at low temperatures is decreased by smaller grain size due to the stronger interaction of different dislocations.

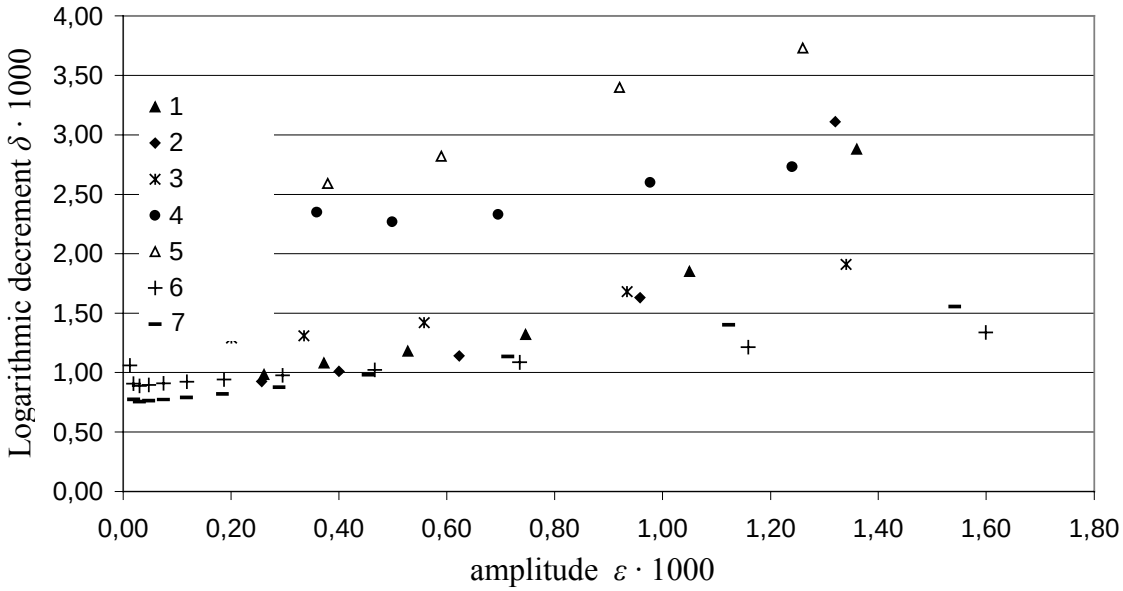

Fig. 8.67. The logarithmic decrement δ vs. maximum strain amplitude ε for heat-treated samples.

Due to the grain refining and special heat-treatment allowing for less grain growth, in samples #6 and #7, more strong pinners are available in the microstructure, thus prohibiting the dislocation-induced damping effects especially at higher strain amplitudes.

9. Conclusions

The goal of this study was to investigate the influence of various process parameters on the mechanical properties of the sand cast magnesium alloy AZ91.

It has been found out that the mechanical properties, such as strength and elongation, may be improved through the application of in-mold filters, grain refinement and heat treatment. Ceramic foam filters were found to be the most effective. Mechanical properties gradually rise with increased filter thickness and decreased pore size. Steel wool filters which are currently in use were shown to be relatively ineffective.

Among the various grain refiners studied, hexachlorethane was the most effective. The efficiency of the grain refinement depends on the wall thickness of the part – for smaller wall thicknesses less grain refiner is needed. It should be noted, however, that though the melt treatment with hexachlorethane decreases the average grain size, mechanical properties increase marginally. A significant disadvantage of the hexachlorethane as a grain refiner is its negative environmental impact caused by the fume development during the melt treatment.

Heat treatment has the largest effect on the mechanical properties of the sand cast magnesium alloy AZ91. Either very high ductility and impact strength or high yield strength may be obtained, depending on the heat treatment chosen. Generally, annealing and quenching (T4 - treatment) renders very high tensile strength and ductility, but decreases yield strength. Annealing and quenching, followed by ageing (T6 - treatment), greatly increase yield strength and also increase tensile strength, but not to the same extent as the yield strength. Elongation at fraction decreases after the ageing. Heat treatment parameters should be carefully chosen, since a prolonged annealing causes grain growth and the scatter of obtained mechanical properties widens. The combination of grain refinement, heat treatment and filtration results in the best values of mechanical properties.

Damping of mechanical vibrations and stress relaxation are the mechanical properties which may be tailored to various engineering applications through the grain refinement and heat treatment as well. The lowest stress relaxation and highest damping was found

in non-grain- refined samples in the as-cast condition. Both stress relaxation and damping increase in the grain-refined, heat-treated parts.
Neutron diffraction experiments were conducted in this study and texture development in various samples was investigated. It has been shown that a clear rotational symmetric fiber texture (100) develops after the deformation. The obtained results open the way to further studies of deformation mechanisms in cast magnesium alloys.

In-depth studies of microstructures, conducted on all samples described here, were done in this work. These studies have revealed a clear interdependence between the mechanical properties and microstructural features of sand cast AZ91. Interestingly, internal friction properties (damping capacity of stress relaxation) may serve as a reliable means to determine microstructural features and, consequently, mechanical properties. In a cast shop, for instance, stress relaxation may be a useful tool to determine the efficiency of the grain refinement. In ae heat-treatment shop, it may also be used for rapid control of microstructure.

The obtained results have clearly shown that through the application of a combination of various metallurgical methods, it is possible to achieve the mechanical properties of the die-cast parts in sand castings. The designer may install and test the sand-cast prototypes in different devices, and be sure of the reliability and transferability of the test results. Futhermore, it is possible to tailor mechanical properties of the sand cast prototypes through the variations of the process parameters. So, for instance, it is possible to manufacture cross-beams (parts which may underlay crash conditions), and through the heat treatment, improve the ductility of these parts to the level obtainable in high pressure die castings. These sand cast prototypes may be crash-tested and the results of the crash tests may be transferred with a high reliability. Or, it is possible to suit the damping capacity of the sand-cast prototypes, such as engine blocks or gear boxes, so that they can generate the noise level typical of the die cast parts.

The results obtained in this study open the way to further investigations. The following problems should be studied:

- Influence of various alloying elements on mechanical properties
- Creep and fatigue strength of sand cast parts of AZ91

- Influence of different sand casting methods on mechanical and physical properties
- Statistical investigation of mechanical properties of serial sand cast parts.

The influence of small variations of basic alloying elements Al and Zn must be studied and statistical information must be provided. Furthermore, what impact do different Al- or Zn- contents have on stress relaxation and damping properties?

Through the addition of certain alloying elements such as Ca or Si it may be possible to improve the creep strength, as it has already been shown in the example of the high pressure die cast AZ91. However, will these alloy elements also be effective in the case of sand cast alloy? Moreover, which impact will the addition of alloying elements have on the mechanical behaviour in different heat-treated conditions? And how will the addition of alloy elements influence the recycling capability of the alloy?

The knowledge of fatigue strength is very important for the development and design of dynamically loaded magnesium parts. To a certain extent, fatigue strength has been studied for high pressure die cast parts. However, no information is available for the sand castings. Thus, since static mechanical properties differ significantly in variously treated parts, how will fatigue properties respond to various melt and heat treatments?

And, finally, extensive statistical investigations on properties, obtained in serial parts must be conducted, as well. Castings with the same wall thickness but different gating and feeding systems may have largely differing mechanical properties, and a statistical approach for various designs is needed.

9. References

[1] D. Magers, J. Willekens, Proc. Intl. Conf. “Magnesium Alloys and their Applications”, April 28-30, Wolfsburg, Germany, p. 105.

[2] N. Zeumer, Proc. Intl. Conf. “Magnesium Alloys and their Applications”, April 28-30, Wolfsburg, Germany, p. 125.

[3] R.L. Edgar, Proc. Intl. Conf. “Magnesium Alloys and their Applications”, September 26-28, Munich, Germany, p. 3.

[4] P. S. Frederick, Die Casting Engineer, 1990, p.10.

[5] H. Naber, F. Breitinger, Giesserei-Erfahrungsaustausch, 2/97, p. 59.

[6] S. Schumann, F. Friedrich, Proc. Intl. Conf. “Magnesium Alloys and their Applications”, April 28-30, Wolfsburg, Germany, p. 3.

[7] D. L. Albright, T. Ruden, “Magnesium Utilization in the North American Automotive Industry”, Light Metal Age, (5), 1994.

[8] G. V. Raynor, “The Physical Metallurgy of Magnesium and its Alloys”, Pergamon press, London, NY, Paris, LA, 1959.

[9] Magnesium Taschenbuch, Editor C. Kammer, Aluminium-Verlag, Düsseldorf, 2000.

[10] W. D. Callister, Jr. „Materials Science and Engineering, An Introduction“, 4th Edition, John Wiley & Sons, Inc. NY, Chichester, Brisbane, Toronto, Singapore, Weinheim, 1997.

[11] P.G. Partridge, Met. Rev. Review, 1967, p. 118.

[12] F. Habashi (editor), “Alloys: Preparation, Properties, Applications”, Wiley-VCH, Weinheim, NY, Chichester, Brisbane, Singapore, Toronto, 1998.

[13] M. Ö. Pekgüleryüz, M. M. Avedesian, DGM Conference "Magnesium Alloys and Their Applications", 1992, Garmisch-Patenkirchen, Germany, p. 213.

[14] M. B. Altmann, M. E. Dritz, M. A. Timonova, M. W. Chukhrov, „Magnesiumlegierungen, Vol. 1, 2“, Moscow, "Metallurgija", 1978.

[15] J. Murray, “Binary Alloys Phase Diagrams, ASM Int., Metals park, OH, U.S.A., 1986, **1**, p. 129 p. 201.

[16] Polmear, I. J., „Light Alloys - Metallurgy of the Light Metals“, Honeycombe, P. W. K., Hancock, P. (eds.); Edward Arnold, London, 1995.

[17] A. Luo, Proc. 3rd Intl. Magnesium Conf., 10-12 April 1996, Manchester, UK, p. 449.

[18] W. Kurz, D. J. Fisher, „Fundamentals of Solidification“, Trans Tech Publications 1989, Switzerland, Germany, UK, USA.

[19] S. Erchov, Diploma Thesis, Technical University of Freiberg, Germany 1999.

[20] E. Aghion, B. Bronfin, Proc. 3rd Intl. Magnesium Conf., 10-12 April 1996, Manchester, UK, p. 313.

[21] O. Holta, H. Westengen, J. Røen, Proc. 3rd Intl. Magnesium Conf., 10-12 April 1996, Manchester, UK, p. 75.

[22] E. Aghion, B. Bronfin, S. Shmelkin, Proc. of the 1st Israeli Intl. Conf. of Magnesium Science and Technology, Dead Sea, Israel, 1997, p. 279.

[23] M. Fukuchi, F. Watanabe, Journal of the Japan Institute of Metals, 39, (5), 1975, p. 493

[24] M. Fukuchi, F. Watanabe, Journal of the Japan Institute of Light Metals, 30, (5), 1980, p. 253.

[25] M. S. Dargush, G. L. Dunlop, K. Pettersen, Intl. Conf. "Magnesium Alloys and their Applications", 1998, April 28-30, Wolfsburg, Germany, p. 277.

[26] Dunlop, G. L., Sequeira, W. P., Dargusch, M. S., Proc. of the 1st Israeli Intl. Conf. of Magnesium Science and Technology, Dead Sea, Israel, 1997, p. 108

[27] M. Regev, M. Bamberger, A. Risen, E. Aghion, Intl. Conf. "Magnesium Alloys and their Applications", 1998, April 28-30, Wolfsburg, Germany, p. 283

[28] S. R. Agnew, S. Viswanathan, E. A. Payzant, Q. Han et al, Intl. Conf. "Magnesium Alloys and their Applications", 2000, September 28-28, Munich, Germany, p.687

[29] Gutman, E.M., Unigovski, Ya., Levkovitsch, M., Koren, Z., Proc. of the 1st Israeli Intl. Conf. of Magnesium Science and Technology, Dead Sea, Israel, 1997, p.169

[30] Mordike, B. L., Lukac, P., Proc. 3rd Intl. Magnesium Conf., 10-12 April 1996, Manchester, UK, p. 419.

[31] M. Polanyi, Z. für Physik, 1934, 89, p.660.

[32] E. Orowan, Z. für Physik, 1934, 89, p. 605, p. 634

[33] G. I. Taylor, Proc. Royal Soc. (London), A145, 1934, p. 362.

[34] R.W. Cahn, P. Haasen, (eds), "Physical metallurgy", 3rd revised and enlarged edition, Part 2, North Holland Physics Publishing, Amsterdam, Oxford, NY, Tokyo, 1983.

[35] J. Friedel, “Dislocations”, Pergamon Press, Oxford, 1964

[36] C. Barrett, T.B. Massalski, “Structure of Metals”, Pergamon Press, Oxford, 1980

[37] W. Schatt, H. Worch (Eds), „Werkstoffwissenshaft“, Dt. Verlag für Grundstoffindustrie, Stuttgart, 1996.

[38] H. Böhm, „Einführung in die Metallkunde“, B.I. Wissenschaftsverlag, Mannheim/Leipzig/Wien, Zürich, 1992.

[39] W. Dahl, R. Kopp, O. Pawelski (Eds.), „Umformtechnik, Plastomechanic unf Werkstoffkunde“Verlag Stahleisen, Düsseldorf, 1993.

[40] Guy, A.G., Petzow, G, „Metallkunde für Ingenieure“Techn.-Phys. Sammlung, Bd. 7., Frankfurt, 1970.

[41] J. G. Sevillano in „Materials Science and Technology“, R.W. Cahn, P. Haasen, E.J. Kramer (Eds.), VCH- Publishing, Weinheim, NY, Basel, Cambridge, 1993.

[42] A. Beck, “Magnesium und seine Legierungen“, Julius Springer Verlag, 1939.

[43] H.-F. Honsel, P. Zimmermann, Giesserei 25, (1963), p. 765.

[44] G. F. Balandin, “Kristallisation aus Schmelzen”, Moscow, Mashinostrojenie, 1973.

[45] H. Busch, Giesserei, 23 (1936), p. 290

[46] Y. Lee, A. Dahle, D. StJohn, Magnesium Technology 2000, TMS 200, S. 211

[47] Heat Treater’s Guide. Practices and procedures for nonferrous alloys, ASM Intl.

[48] M.W. Chukhrov, S.I. Borovikova, A.I. Sokolova, “Light metals research”, AN USSR Publication, 1963.

[49] O.B. Abramov, “Crystallisation of metals in the ultrasonic field”, Moscow, Metallurgija, 1972.

[50] R.E. Smallman, R.J. Bishop, “Metals and Materials”, Butterworth Heinemann, Oxford, London, 1995.

[51] R.S. Busk, “Magnesium Products Design”, Marcel Dekker, New York, 1987.

[52] Magnesium Electron Ltd, Report MR10/773, December 1981.

[53] Heat Treatment of Magnesium Alloy Castings, ASM Publication (?)

[54] D. Regener, E. Ambos, H.Heyse, Giessereiforschung 49 (1997), Nr. 4, p. 163

[55] J. B. Clark, Acta Metallurgica, 1968, 16, p. 141.

[56] A. F. Crawley, K.S. Milliken, Acta Metallurgica, 1974, 22, p. 557.

[57] C. J. Bettles, P. Humble, J.F.Nie, Proc. 3rd Intl. Magnesium Conf., 10-12 April 1996, Manchester, UK, p. 403

[58] B. Lagowski, AFS Transactions, 71-41, p. 115

[59] K. E. Mann, Gießerei, 52, 1965, p. 664.

[60] E. Arnoudt, P. V. Houttle, T. Leffers in “Materials Science and Technology” Vol. 6, R.W. Cahn, P. H. Haasen, E. J. Cramer (Eds.), VCH-Publishing, Weinheim, New York, Basel, Cambridge, 1993.

[61] “Structural Neutronography” Vol. 1, Ju. Z. Nowik, R. P. Ozerow, K. Hennig, Moscow, Atomizdat, 1979.

[62] P. Klimanek in "Werkstoffanalytische Verfahren", H.-J- Hunger (Ed.), Dt. Verlag für Grundstoffindustrie, Leipzig, Stuttgart, 1995

[63] R. B. v. Dreele in "Materials Science and Technology", Vol. 2b, R.W. Cahn, P. H. Haasen, E. J. Cramer (Eds.), VCH-Publishing, Weinheim, New York, Basel, Cambridge, 1993.

[64] R. Batist in „Materials Science and Technology", Vol. 2b, Eds. R. W. Cahn, P. Haasen, E. J. Kramer, VCH-Publishing, Weinheim, New York, Basel, Cambridge, Tokyo, 1994.

[65] W. Riehemann, "Metallische Werkstoffe mit extremer innerer Reibung und deren Messung", Papierflieger, Clausthal-Zellerfeld, 1994.

[66] W. Riehemann, „Internal Friction in Magnesium Materials", Intl. Conf. „Magnesium Alloys and their Applications", April 28-30, 1998, Wolfsburg, Germany, p. 61.

[67] K. Sugimoto, J. Iron and Steel Inst. Japan, 1974, (14), p. 2203.

[68] M. Shimizu, H. Takeuchi, Int. J. Cast Metals Res., 1997, (10), p. 159.

[69] Z. Trojanová, W. Riehemann, F. von Buch et al., phys. stat. sol. (a) 175, 1999, p. 555.

[70] P. Buchhagen, W. Riehemann, B.L. Mordike, Intl. Conf. „Magnesium Alloys and their Applications", April 8-10, 1992, Garmisch-Patenkirchen, Germany, p. 229.

[71] P. Buchhagen, W. Riehemann, B. L. Mordike, Intl. Conf. „Magnesium Alloys and their Applications", April 8-10, 1992, Garmisch-Patenkirchen, Germany, p. 455.

[72] F. Abed el-al, J. Göken, W. Riehemann, B. L. Mordike, Intl. Conf. „Magnesium Alloys and their Applications“, April 28-30, 1998, Wolfsburg, Germany, p. 351.

[73] Z. Trojanová, P. Lukáč, W. Riehemann, B. L. Mordike, Proc. Second Israeli Intl. Conf. Magnesium Sci. and Tech., February 22-24, 2000, Dead Sea, Israel, p.190.

[74] Z. Trojanová, P. Lukáč, W. Riehemann, B. L. Mordike, Proc Second Intl. Symposium on Advanced Materials and Technologies, December 5-7, 1995, Prague, CR.

[75] Z. Trojanová, P. Lukáč, W. Riehemann, B. L. Mordike, Intl. Conf. „Magnesium Alloys and their Applications“, April 28-30, 1998, Wolfsburg, Germany, p. 357.

[76] J. Göken, W. Riehemann, Mat. Sci. Eng (A) (2001)- accepted for publication.

[77] B. Watzinger, P. Weidinger, F. Breutlinger et al., „Intl. Conf. „Magnesium Alloys and their Applications“, April 28-30, 1998, Wolfsburg, Germany, p. 259.

[78] K. Sugitomo, K. Matsui, T. Okatomo, K. Kishitake, Trans. JIM 16 (1975), p.647.

[79] A. Granato, K. Lücke, J. Appl. Phys. (27) 1956, p. 583

[80] W. Riehemann, P. Fleischer, V. Martens, Journal of Alloys and Compounds, 211/212 (1994), p. 596.

[81] Nikulin, L. W., Liptschin, T. N., Saslawski, M. L., „Die Casting of Magnesium Alloys“, "Maschinostrojenije", Moscow, 1978

[82] Gjestland, H., Westengen, H., Plahte, S., , Proc. 3rd Intl. Magnesium Conf. 1996, Manchester, UK., The Institute of Materials, p. 33.

[83] Rauch, E., Giesserei 82 (1995) Nr. 10, p. 347.

[84] Gjestland, H., Magers, D., 6. Magnesiumguss Abnehmerseminar and Automotive Seminar; 30.9-1.10 1998; Aalen, Germany.

[85] Metals Handbook, 8th edition, ASM Publication, 1970.

[86] Smith, F. B., Die Casting Engineer, 9/10 (1997), pp. 135-139

[87] Kolobnev, I. F. (Ed.), „Casting of Light Metal Alloys“, Moscow, Metallurgija, 1966.

[88] P. Spitaler, Giesserei 26, (1957), p. 757.

[89] P. Spitaler, Giesserei 23, (1936), p. 177.

[91] D. Oymo et al., Light metals 1994, p. 1017

[92] C. J. Simensen, B. Oberländer, Z. Praktische Metallographie, 17 (3), 1980, p. 125.

[93] S. E. Housh, V. Petrovich, SAE Technical Paper 920071

[94] A. D. Patel, N. El-Kaddah, Light Metals 1997, p. 1013

[95] T. A. Engh, “Principles of Metal Refining”, Oxford University Press, Oxford, UK, 1992

[96] P. Bakke et al., Light Metals 1992, p. 923

[97] P. Bakke et al., Materials and Manufacturing processes, 9(1), 1994, p. 111

[98] S. Sirrel, J. Campbell, AFS Transactions 1997, S. 645-654.

[99] Ch. Dickenson, “Filters and Filtration Handbook”, 3rd edition, Elsevier Advanced Technology, Oxford, 1991.

[100] D. B. Purchas, “Industrial Filtration of Liquids”, Leonard Hill, London, 1967.

[101] L. C. B. Martins, L. S. Aubrey, B. Cummings, “Effect of Preheating and Priming Time on the Proper Start-up of Ceramic Foam Filters”, Commercial Information of ACF Company, USA.

[102] G. Siebel, Z. Metallkunde, 39 (1948), p. 97.